**Thèse de doctorat**


## Université de Limoges

**École Doctorale Sciences et Ingénierie pour l'Information, Mathématiques (ED 521)**

**XLIM CNRS UMR-7252 Axe Photonique**


Thèse pour obtenir le grade de

Docteur de l'Université de Limoges

Mention : Électronique des Hautes Fréquences, Photonique et Systèmes


Présentée et soutenue par

**Mathieu Jossent**


Le 4 mai 2017

# Développement de fibres optiques à dispersion contrôlée pour l'élaboration de lasers ultrarapides à 2 µm.

Development of dispersion tailored optical fibers for ultrafast 2 µm lasers

Thèse dirigée par Sébastien Février

JURY :

Président du jury

| | |
|---|---|
| M. Philippe DI BIN | Professeur<br>XLIM, Université de Limoges |

Rapporteurs

| | |
|---|---|
| M. Jayanta SAHU | Professeur<br>ORC, Université de Southampton |
| M. Ammar HIDEUR | Maître de conférences HDR<br>CORIA, Université de Rouen |

Examinateur

| | |
|---|---|
| M. Laurent BIGOT | Chargé de recherche 1 CNRS – HDR<br>PhLAM, Université de Lille 1 |

Invités

| | |
|---|---|
| M. Arnaud GRISARD | Ingénieur<br>TRT, Thales, Palaiseau |
| M. Sébastien FEVRIER | Maître de conférences HDR<br>XLIM, Université de Limoges |

To my family


BY-NC-ND

## Copyright

Cette création est mise à disposition selon le Contrat :

« **Attribution-Pas d'Utilisation Commerciale-Pas de modification 3.0 France** »

disponible en ligne : *http://creativecommons.org/licenses/by-nc-nd/3.0/fr/*

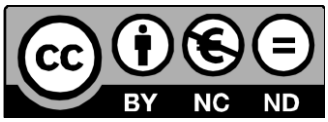




BY-NC-ND

## Table of contents





BY-NC-ND

BY-NC-ND

## Chapter I. Context

The ANR-funded project UBRIS2 aims at developing innovative ways towards the realization of high-power ultrafast laser systems at the wavelength of 2 µm. One approach to build high-energy lasers at 2 µm relies on parabolic amplification, a concept that has never been explored at 2 µm so far. The 2-µm parabolic amplifier would rely on Thulium-doped fibers with tailored high normal dispersion (high –D), providing temporal broadening along the amplifier leading to an increase of the storable energy compared to conventional systems. This concept has been successfully used at 1 µm where silica exhibits normal dispersion but remains unexploited at 2 µm due to the lack of properly designed fibers. **The goal of my PhD was to design and develop parabolic amplifiers based on specialty active fibers producing high normal dispersion at 2 µm.**

Parabolic amplification or direct amplification in normal dispersion regime, yields a particular class of pulses, the similariton, characterized by parabolic temporal and spectral shapes that homothetically grow along the active fiber. Similaritons result from the interplay between gain and nonlinear Kerr effect in normally dispersive materials.

In this context, this chapter gives an overview of the physical mechanisms at stake in the formation of similaritons in optical fibers with a particular emphasis on (i) energy scaling and (ii) transposition of this concept towards the mid-infrared. The effects of optical nonlinearities in optical fibers are briefly reviewed. This review is followed by a description of the generalized nonlinear Schrödinger equation with gain. Finally, state-of-the-art ultrafast high power amplifiers based on active fibers emitting at 1 µm and 2 µm are presented with an emphasis on the fiber design.

### I.1. Nonlinearities in optical fibers

The main constituent of optical fiber is silica ($SiO_2$). Silica is a dielectric, meaning that the charge carriers in this material are strongly bound to one another. Hence, they are unable to move, in a macroscopic scale, under the influence of an electrical field. However, in a microscopic scale, the links between the charge carriers have a certain elasticity allowing them a transitory displacement under the influence of an electrical field. Those charge movements imply the creation of several induced dipoles within the material. The interactions between those charge carriers and the applied electrical field generates a polarization of the media.

In the case of a weak electromagnetic field, the polarization $P_{ol}$ of the material is proportional to the applied electrical field $E_F$ by the dielectric constant $\varepsilon_0$ and the material electrical susceptibility $\chi^{(1)}$:


BY-NC-ND

$$P_{ol} = \varepsilon_0 \chi^{(1)} E_F \quad \text{(I.1)}$$

The linear susceptibility $\chi^{(1)}$ is a complex number and can therefore be expressed by its real and imaginary parts $\chi^{(1)} = \chi'^{(1)} + i\chi''^{(1)}$. This parameter depends on the wavelength of the excitation electromagnetic wave. It gives access to two parameters: the refractive index $n_0$ of the media and its absorption $\alpha$:

$$n_0(\lambda) = 1 + \frac{1}{2}\chi'^{(1)}(\lambda) \quad \text{(I.2)}$$

$$\alpha(\lambda) = \frac{2\pi}{n_0(\lambda)\lambda}\chi''^{(1)}(\lambda) \quad \text{(I.3)}$$

However, with an increased intensity of the electromagnetic field, nonlinear response of the material could be observed. The relation (I.1) will therefore be incomplete since the material will produce a nonlinear response to the excitation field. The polarization is therefore expressed by:

$$P_{ol} = \varepsilon_0 \left( \chi^{(1)} E_F + \chi^{(2)} {E_F}^2 + \chi^{(3)} {E_F}^3 + \ldots \right) \quad \text{(I.4)}$$

In this expression, the linear susceptibility $\chi^{(1)}$ can be identified. The other components $\chi^{(j)}$ represent the nonlinear susceptibilities of the $j^{th}$ order and are responsible for nonlinear effects within the material. In general, those effects are categorized by the order *j* of the considered susceptibility.

In dielectrics composed by centro-symmetrical molecules, such as silica, $\chi^{(2)}$ is evanescent and therefore will not have any effect in optical fibers. However, this order of susceptibility is responsible of effects such as the second harmonic generation in crystals. In the following, the contribution of $\chi^{(2)}$ will be taken equal to zero. In that way, when considering silica based optical fibers, the nonlinear effects arise from the third order nonlinear susceptibility $\chi^{(3)}$. Some of those effects will be discussed in the following.

### I.1.1. Optical Kerr effect

When an electromagnetic field of high intensity passes through a dielectric material, the wave oscillating electrical field generates the induced electrical dipoles. The electrical dipoles presenting the highest dipolar moment might then orientate themselves in the electrical field direction creating local birefringence in the media. The refractive index profile is no more a constant at a given wavelength $\lambda$ but becomes dependent on the applied electrical field intensity. This nonlinear index has the following expression:


BY-NC-ND

$$n\left(\lambda,\left|E_F(z,t)\right|^2\right)=n_0(\lambda)+n_2(\lambda)\left|E_F(z,t)\right|^2 \quad \text{(I.5)}$$

with $n_0(\lambda)$ the linear refractive index as defined previously and $n_2(\lambda)=\frac{3\chi^{(3)}}{8n_0(\lambda)}$ the index change due to the third order nonlinearity. For pure silica, $n_2 = 2.24\cdot10^{-20}m^2.W^{-1}$ at 1.55 µm [1]. However, this experimental value of the nonlinear index also depends on impurities and/or dopants (Germanium, Phosphorus, Fluorine, Aluminum, rare earth ions…) within the glass matrix.

The dependency of the refractive index to the electrical field intensity is called “optical Kerr effect”. The wave passing through the material will locally change the refractive index of the material in which the wave propagates. This self-process leads to an addition of a phase term called to the wave itself. This effect is referred to as ‘self-phase modulation’ (SPM). The phase therefore writes:

$$\phi(z,t)=\left(n(\lambda)+n_2\left|E_F(z,t)\right|^2\right)\cdot k_0 L \quad \text{(I.6)}$$

where $k_0$ is the wave vector norm and is equal to $2\pi/\lambda$, *L* is the fiber length. The nonlinear phase is $\phi_{NL}=n_2k_0L\left|E_F\right|^2$.

The nonlinear coefficient $\gamma$ expresses the strength of the third order nonlinearities arising from Kerr effect in an optical fiber and is given by [1]:

$$\gamma=\frac{2\pi n_2(\lambda)}{\lambda A_{eff}(\lambda)} \quad \text{(I.7)}$$

where $A_{eff}$ is the effective mode area of the fiber fundamental mode. This area represents the zone over which the optical power is distributed and therefore depends on the transverse repartition of the modal field.

$$A_{eff}=\frac{\left(\iint\left|\vec{E}_F\right|^2 dS\right)^2}{\iint\left|\vec{E}_F\right|^4 dS} \quad \text{(I.8)}$$

with dS a surface element of the considered fiber section.

A characteristic length can also be defined and is called the nonlinear length $L_{NL}$. This parameter gives an idea of the fiber length from which nonlinear effects due to Kerr effect become important:


BY-NC-ND

$$L_{NL} = \frac{1}{\gamma P_0} \qquad \text{(I.9)}$$

This nonlinear length depends on the nonlinear coefficient $\gamma$ of the optical fiber and on the input power $P_0$ (the pulse peak power in the case of pulsed sources). For a pulse with 10 kW of peak power propagating in a singlemode fiber at the wavelength of 1.9 µm ($A_{eff}$ = 150 µm²) the calculated nonlinear length $L_{NL}$ is roughly equal to 0.2 m which is a tenth of the length of commonly used fiber amplifiers. Moreover, in an amplifier $P_0$ will increase thus the impact of nonlinearities will not be negligible.

When considering pulses, in the slowly varying envelope approximation, propagating in a nonlinear media, the electric field amplitude has a maximum at the envelope peak and decreases on its edges. Since the nonlinear refractive index is intensity dependent, it will decay continuously from the pulse peak to its wings. The nonlinear phase variation $\phi_{NL}$ (as in equation I.6) will lead to a shift of the electrical field oscillations extrema. At the pulse front, both the nonlinear refractive index and nonlinear phase increase leading to a delay on the peak positions. The wave frequency decreases. On the contrary, at the pulse trail, both the refractive index and nonlinear phase decrease leading to an increased wave frequency. Hence, the self-phase modulation mechanism leads to a spectral broadening of the pulse. This spectral broadening is a direct consequence of the time dependence of $\phi_{NL}(z,t)$. A temporally varying phase implies that the instantaneous optical frequency differs across the pulse from its central value. This can be seen as a frequency chirp that increases in magnitude with the propagated distance. Bluntly, new frequency components are continuously generated as the pulse propagates down the fiber through the SPM mechanism as can be seen in Figure I-1 (c).

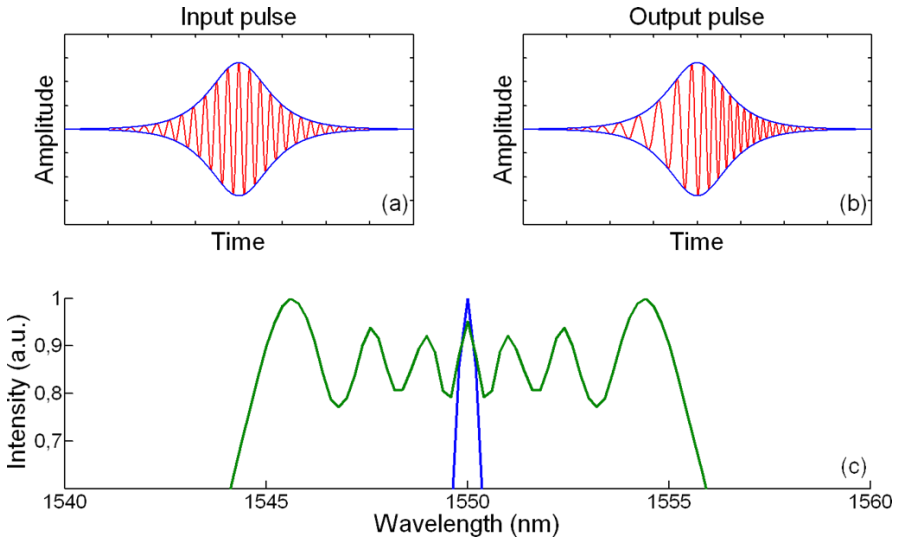


Figure I-1: Simulated electrical field oscillations of a laser pulse inside a fiber. The intensity variation is represented by the pulse envelope. (a) Input pulse. (b) Output pulse. (c)


BY-NC-ND

Spectra for the input pulse (blue) and the is output pulse (green), showing spectral broadening by the optical Kerr effect.

### I.1.2. Stimulated Raman scattering

Kerr effect (and its manifestation SPM) are instantaneous nonlinear effects. However, delayed phenomena do exist such as Stimulated Brillouin and Raman scatterings (SBS and SRS respectively). Both those effects are categorized as inelastic since they arise from an energy exchange between the media and the electrical field . They are both based on the excitation of vibrational or rotational modes of the nonlinear media. Stimulated Brillouin scattering vanishes when using pulsed sources delivering pulses shorter than 10 ns. SBS will not be further addressed since it will not be triggered in ultrafast regime. In the case of Raman scattering, a photon at a pump wavelength is absorbed by a media molecule as shown in Figure I-2. This molecule enters an excited state. When this molecule goes back to its ground state, a photon of lower energy is emitted. The difference in terms of energy between the two photons is the molecule vibrational or rotational state energy ($h\nu_{Molecule}$). The emitted photon wavelength is called the Stokes wavelength when $\lambda_{pump} < \lambda_{Stokes}$. On the contrary, it can be called the Anti-Stokes wavelength when $\lambda_{pump} > \lambda_{Stokes}$, meaning that the emitted photon has more energy than the pump photon, hence the molecule was already in is vibrational state before interacting with the pump photon.

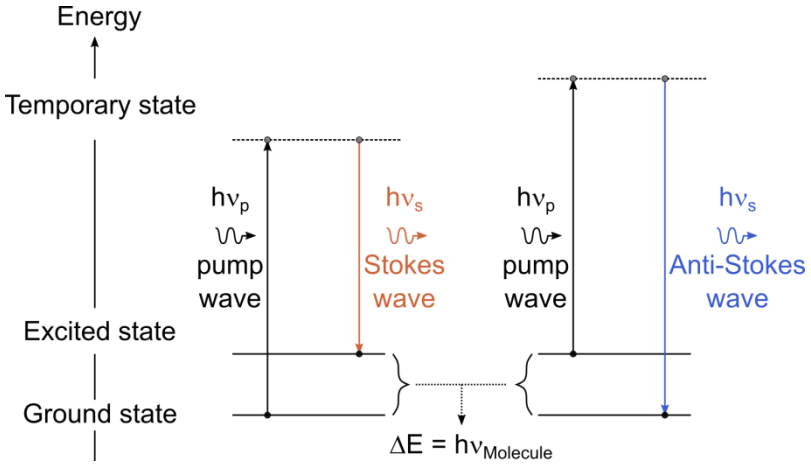


Figure I-2: Stimulated Raman Scattering - Energy diagram of the generation of Stokes and Anti-stokes waves.

When high peak power at the pump wavelength, enough to trigger SRS, is injected in an optical fiber, the output spectrum will not be monochromatic anymore. It will be composed of the pump frequency surrounded by sidebands: a red-shifted peak (Stokes) and a blue-shifted peak (Anti-Stokes). This difference in frequency is governed by the difference in energy due to the vibrational (or rotational) state. Therefore the strength of Raman scattering is inherent to the considered material. For pure silica, the most efficient frequency shift imposed by Raman scattering is $\Delta\nu$ = 13.2 THz as shown in Figure I-3. Figure I-3 shows the


BY-NC-ND

imaginary part of the Raman susceptibility of silica against frequency. Raman gain ($g_R$) is directly linked to this imaginary part.

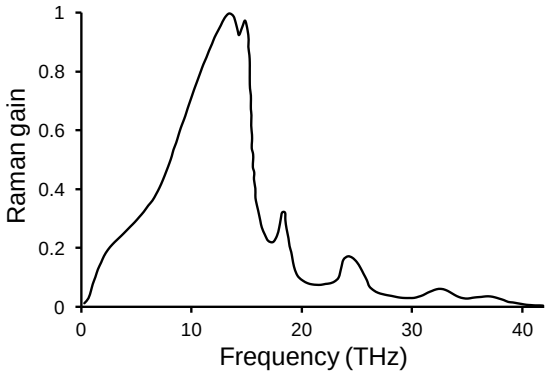


Figure I-3: Imaginary part of the Raman susceptiblity (=Raman gain in arbitrary units) in a $SiO_2$ core fiber.

However, the Raman peak intensity is different when considering either the Stokes or Anti-Stokes peak. This difference is due to the fact that fewer molecules are to be in an excited state while considering any media. Therefore, the peak intensity of the red shifted (Stokes) frequency is higher. Moreover, if the Stokes peak has enough energy to also trigger SRS, cascaded SRS can be achieved [2].

In the case of short pulses, they can have a spectrum wide enough that the Raman gain can amplify the low-frequency components by transferring energy from the high-frequency components of the pulse (non null slope at 0 frequency). As a result, the pulse spectrum shifts toward the red side as the pulse propagates inside the fiber, this phenomenon is referred to as self-frequency shift (SFS) and originates from the delayed nonlinear response of the propagating media. The SFS of pulses in optical fiber has been used to produce new wavelengths allowing new windows of operation and vast possibilities [3]. SFS has also been reported to have a key role in beam cleaning process for pulses operated in multimode fibers [2].

### I.1.3. Nonlinear Schrödinger equation

Modeling the propagation of the pulse envelope along a fiber, in the slowly varying envelope approximation, can be realized by solving the nonlinear Schrödinger equation given by:

$$\frac{\partial A(z,t)}{\partial z} + \beta_1 \frac{\partial A(z,t)}{\partial t} + \frac{i}{2}\beta_2 \frac{\partial^2 A(z,t)}{\partial t^2} + \frac{\alpha(\omega)}{2} A(z,t) = i\gamma |A(z,t)|^2 A(z,t) \quad \text{(I.10)}$$

with A the electrical field temporal envelope, $\alpha$ the propagation losses, $\gamma$ the nonlinear coefficient (Eq. I.7), $\beta_1$ and $\beta_2$ the first and second derivative of the propagation constant $\beta$ according to the pulsation $\omega$ given by:


BY-NC-ND

$$\beta_1(\omega) = \frac{d\beta}{d\omega} = \frac{d[(2\pi/\lambda)n(\omega)]}{d\omega} = \frac{1}{c}\left(n(\omega) + \omega\frac{dn(\omega)}{d\omega}\right) \quad \text{(I.11)}$$

$$\beta_2(\omega) = \frac{\lambda^3}{2\pi c^2}\frac{d^2n(\omega)}{d\omega^2} \quad \text{(I.12)}$$

Equations I.12 and I.13 allow the definition of two key parameters in optical fibers: the group velocity ($v_g = 1/\beta_1 = c/n_g$ with $n_g$ the refractive index seen by the pulse called the group index) which represents the pulse envelope velocity, and the group velocity dispersion (chromatic dispersion: $D_C(\lambda) = -\beta_2\left(2\pi c/\lambda^2\right)$) which is responsible for temporal broadening during the propagation. In our case, optical fibers are electromagnetic waveguides. The guided electromagnetic field has a peculiar distribution over the plan orthogonal to the propagation axis depending on the boundary conditions at the core-cladding interface and due to its cylindrical symmetry. This distribution is caracterized by a group of electromagnetic modes called Lineary Polarized modes ($LP_{nm}$) which are composed by linear combination of pure electromagnetic modes. Those modes 'see' the waveguide with a different refractive index and therefore propagates at different speeds. At a given wavelength, a mode propagates at speed *v* allowing the definition of its effective index ($n_{eff}$) given by:

$$n_{eff} \approx c/v \approx n_M + \Delta n_W \quad \text{(I.13)}$$

with *c* the celerity, $n_M$ the material refractive index (taken to be the cladding refractive index) and $\Delta n_W$ the refractive index contrast in the waveguide. Depending on the considered guided mode, the effective index can present different slope variations hence different dispersion (*D*). When considering a mode of an optical fiber, Equation I.13 can be written as:

$$D = \frac{-2\pi}{\lambda}\frac{\partial^2\beta}{\partial\omega^2} = \frac{-2\pi}{\lambda c}\left(2\frac{\partial n_{eff}}{\partial\omega} + \omega\frac{\partial^2 n_{eff}}{\partial\omega^2}\right) \quad \text{(I.14)}$$

$$D = \frac{-2\pi c}{\lambda^2}\frac{\partial^2(k_0\Delta n_W)}{\partial\omega^2} + \frac{-2\pi c}{\lambda^2}\frac{\partial^2(k_0 n_M)}{\partial\omega^2} = D_W + D_M \quad \text{(I.15)}$$

The dispersion of a mode propagating in a fiber can hence be written as the sum of two contributions: the waveguide dispersion ($D_W$) and the material dispersion ($D_M$). $D_M$ is fixed by the glass matrix, here silica (Figure I-4). $D_W$ can be adjusted by optimizing the refractive index profile (RIP) of a fiber.


BY-NC-ND

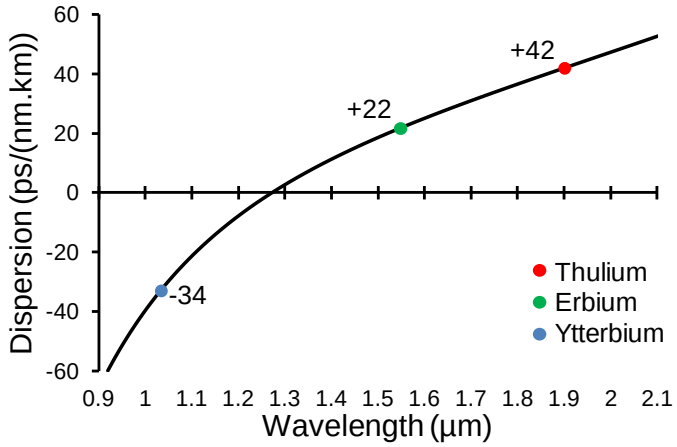


Figure I-4: Silica dispersion curve calculated by Sellmeier series from [4]. Dispersion values at commonly used lasing wavelengths: Ytterbium 1.03 µm (blue), Erbium 1.55 µm (green) and Thulium 1.9 µm (red).

The waveguide contribution to dispersion is strongly dependent to the radial field distribution according to wavelength and can be expressed as follows:

$$D_W \propto \lambda \int_0^{\infty} \left( \frac{dE(r)}{dr} \right)^2 rdr + \lambda^2 \frac{d}{d\lambda} \left( \int_0^{\infty} \left( \frac{dE(r)}{dr} \right)^2 rdr \right) \qquad \text{(I.16)}$$

The waveguide dispersion dependence of the fundamental mode is weak as its radial field distribution varies slowly from 1 to 2 µm. Therefore, the dispersion of the fundamental mode is close to that of silica. The lower the waveguiding effect, the closer the chromatic dispersion is to the material dispersion. This is especially the case in large effective mode area fibers, where waveguiding effects on dispersion are negligible.

In pulsed regime, it is useful to define another characteristic length called the dispersion length:

$$L_D = \frac{T_0^2}{|\beta_2|} \qquad \text{(I.17)}$$

with $T_0$ the duration at $1/e$ of the pulse envelope. For a Gaussian pulse, the full width at half maximum intensity (FWHMi) relates to $T_0$ by $\Delta T_{FWHMi} = \sqrt{2\ln(2)}T_0$. $L_D$ is the distance at which the duration of a Gaussian pulse is multiplied by $\sqrt{2}$. As an example, let us consider a 250 fs ($\Delta T_{FWHMi}$) Gaussian pulse centered at the wavelength of 1.9 µm propagating in a single mode fiber (SMF). At 1.9 µm, the chromatic dispersion of a SMF is of 42 ps/(nm.km) ($\beta_2 \approx -8.10^{-26}$ s²/m). The calculated value of the dispersion length $L_D$ is roughly 0.6 m which is at least three times lower than the length of commonly used fiber amplifiers. Therefore, the impact of chromatic dispersion will not be negligible.


BY-NC-ND

## I.2. Generalized nonlinear Schrödinger equation

Equation (I.10) describes the propagation of an optical pulse in single-mode passive fibers. It includes the effects of fiber loss through $\alpha$, group delay through $\beta_1$, chromatic dispersion through $\beta_2$ and fiber nonlinearities through $\gamma$. The group velocity dispersion can either be positive or negative depending on whether the wavelength is shorter or longer than the zero-dispersion wavelength $\lambda_D$ of the considered mode In the anomalous-dispersion regime ($\lambda > \lambda_D \Rightarrow \beta_2 < 0 \Leftrightarrow D > 0$) the fiber can support optical soliton which will be introduced later. Although this propagation equation allowed explaining a large number of nonlinear effects, it needs modification in order to include other experimental conditions. Here, neither Raman-induced self-frequency shift nor the gain impact are included. The inclusion of these effects leads to the generalized propagation equation:

$$\frac{\partial A(z,T)}{\partial z} - i\sum_{k\geq 2}\frac{i^k\beta^k}{k!}\frac{\partial^k A(z,T)}{\partial t^k} + \frac{G(z,\omega)}{2}A(z,T) = i\gamma\left(1+\frac{i}{\omega_0}\frac{\partial}{\partial T}\right)\left(A(z,T)\int_{-\infty}^{T}R(t')\left|A(z,T-t')\right|^2 dt'\right) \tag{I.18}$$

where the chromatic dispersion in expressed as a Taylor expansion of the propagation constant about the pump wavelength, *G* stands for the fiber gain and loss depending on wavelength and fiber length, $\gamma$ includes the optical Kerr effect, $(i/\omega_0)\cdot(\partial/\partial T)$ refers to the inclusion of self-steepening which reduces the velocity at which the peak of the ultra-short pulse propagates leading to an increasing slope of the trailing part of the pulse, the integral is the delayed Raman response accounting for SFS. This equation includes the impact of $\beta_1$ by using a co-moving time frame moving at the group velocity ($T = t - \beta_1 z$).

When considering pulses propagating near the zero-dispersion wavelength $\lambda_D$ ($\beta_2 \approx 0$) or for pulses having temporal width below 1 ps [1], the third order dispersion parameter has an impact. This phase term induces a temporal dissymmetry onto the pulse limiting its subsequent compressibility.

### I.2.1. Modeling the propagation of short pulses in optical fibers

A convenient way to solve the GNLSE (Eq. I.18) is a pseudo-spectral model referred to as the symmetric split-step Fourier method. It assumes dispersion and nonlinear effects act independently over a short piece of fiber. It is practical to use equation (I.19) as:

$$\frac{\partial A}{\partial z} = \left(\breve{D} + \breve{N}\right)A \tag{I.19}$$


BY-NC-ND

where $\check{D}$ is the differential operator representing the dispersion and gain/absorption in a linear medium and $\check{N}$ is the nonlinear operator ruling all the nonlinear effects on pulse propagation. These operators are given by:

$$\check{D} = i\sum_{k\geq 2}\frac{i^k\beta^k}{k!}\frac{\partial^k}{\partial t^k}(\ ) - \frac{G(z,\omega)}{2} \tag{I.20}$$

$$\check{N} = i\gamma\left(1+\frac{i}{\omega_0}\frac{\partial}{\partial T}\right)\left(\int_{-\infty}^{T} R(t')\left|A(z,T-t')\right|^2 dt'\right) \tag{I.21}$$

The symmetrized split-step Fourier method obtains an approximate solution by assuming that propagation over a small distance *h* is carried out in three steps. First, the pulse propagates over half the distance with dispersive effects only. Then, in the middle of the section, nonlinearity is included after which the pulse propagates again half the distance with dispersive effects only (Figure I-5).

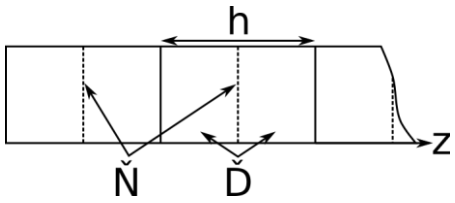


Figure I-5: Diagram of the symmetrized split-step Fourier method. Dispersive operator is applied over [z;z+h/2[ and ]z+h/2;z+h[. Nonlinear operator is applied at z+h/2.

Mathematically,

$$A(z+h,t) \approx \exp\left(\frac{h}{2}\check{D}\right)\exp\left(\int_{z}^{z+h}\check{N}(z')dz'\,e\right)\exp\left(\frac{h}{2}\check{D}\right)A(z,t) \tag{I.22}$$

The exponential operators can be evaluated in the Fourier domain. For the dispersive operator exp(h$\check{D}$/2), this yields:

$$\exp\left(\frac{h}{2}\check{D}\right)A(z,t) = F_T^{-1}\left(\exp\left(\frac{h}{2}\check{D}(i\omega)\right)F_T\left(A(z,t)\right)\right) \tag{I.23}$$

where $F_T$ denotes the Fourier transform operation, $\check{D}(i\omega)$ is obtained by replacing the differential operator $\partial/\partial T$ by $i\omega$. $\check{D}(i\omega)$ is just a number in the Fourier space so the evaluation of Equation (I.23) is straightforward.

Successive iterations of this procedure will give access to the evolution of the electrical field envelope along the fiber. The optical fiber length will therefore be divided by a


BY-NC-ND

fair amount of intervals. In order to lower errors and gain in accuracy, the step *h* must be at least two orders of magnitude lower than the shortest characteristic length. Depending on the dispersion regime, several types of pulses can be found while numerically solving the GNLSE. In the following, I will introduce two kinds of pulses namely *soliton* and *similariton* which can exist in anomalous and normal dispersion regimes respectively. Those explanations are adapted from Liu's thesis [5].

### I.2.2. Pulse in the anomalous dispersion regime: Solitons

#### I.2.2.1. Soliton theory

Soliton pulses are formed thanks to a balance between the nonlinear phase induced by the Kerr effect and the anomalous dispersion. It maintains its shape and energy along the propagation once it is formed. It has many solutions for each integer value of the soliton number N defined as

$$N = \gamma P_0 (T_0)^2 / |\beta_2| \tag{I.24}$$

High order solitons correspond to *N*>1. Fundamental *N* = 1 soliton is a solution of the equation (I.25) of the form (I.26):

$$\frac{\partial A}{\partial z} = -i\frac{\beta_2}{2}\frac{\partial^2 A}{\partial t^2} + i\gamma\left(|A|^2\right)A \tag{I.25}$$

$$A(z,t) = A_0 \operatorname{sech}(t/T_0)\exp(iz/2) \tag{I.26}$$

If this solution is injected into the GNLSE, we obtain a simple relation between the pulse parameters and the system parameters called the *soliton area theorem*:

$$E_T = |\beta_2|/(\gamma T_0) \tag{I.27}$$

According to Equation (I.27), the soliton energy is clamped by balancing nonlinearity and dispersion. When considering a fundamental soliton centered at 1.9 µm wavelength with 250 fs pulse duration propagating in standard fibers with parameters close to those of SMF-28 (8.2 µm core diameter, *D* = 42 ps/(nm.km)), the obtained energy is around 0.7 nJ. In this configuration, $L_{NL}$ and $L_D$ are equal showing the required balance between nonlinearities and dispersion to maintain a fundamental soliton. A first approach used to increase the energy of solitons relies on the use of large mode area gain fiber with reduced nonlinear coefficient $\gamma$. For example, Horton and co-workers [6] used 360 fs pulses containing 500 nJ of energy centered at 1.55 µm at a repetition rate of 1 MHz to seed a rod-type fiber presenting 2300 µm² of $A_{eff}$. Taking advantage of the soliton Raman self-frequency shift, the output pulses presented duration of 65 fs centered at 1.675 µm containing 67 nJ of energy.


BY-NC-ND

#### I.2.2.2. Soliton laser

The fundamental soliton has the property of maintaining its shape along the fiber once it is formed and can withstand strong perturbations, such as gain and loss. Solitons were observed in laser oscillator [7]. Temporal breathing in the laser cavity was also shown to be effective in increasing the pulse energy [8], [9].

In 2013, a high-energy dissipative soliton oscillator based on a single mode Erbium doped fiber was reported [9]. Wang and coworkers achieved the net normal dispersion by introducing a dispersion compensating fiber producing high normal dispersion and a highly Erbium doped normally dispersive active fiber while all other components and fibers were exhibiting anomalous dispersion. As in [8], the active core was smaller compared to the other fiber pieces to produce SPM and achieve normal dispersion. The mode locking was realized by resonant saturable absorber mirror which induces spectral filtering narrower than the erbium gain bandwidth. The oscillator output pulses carried 7 nJ of energy in 10 ps at a repetition rate of 35 MHz. Those pulses could be compressed down to 640 fs assuming a Gaussian pulse shape.

Unfortunately, single mode Thulium doped fibers present high anomalous dispersion and reaching the dissipative soliton regime in an anomalous dispersion gain media is quiet challenging. Tang and coworkers have tried to transpose this regime around the wavelength of 2 µm [10] by adding ultra high numerical aperture (UHNA) fibers in the cavity. UHNA fibers come with small cores to keep a single mode behavior and therefore produce normal dispersion in the anomalous dispersion region of silica. In their setup, the mode locking was assured by NPE. After fine tuning the lengths of the UHNA fiber, they manage to obtain output pulses carrying 8.3 nJ of energy in ~3 ps at a repetition rate close to 20 MHz. Those pulses could be compressed down to 150 fs by a 65% efficiency compressor producing 36 kW peak power. The chirp of the pulses was less than the cavity group delay dispersion which is a feature of self-similar evolution and not dissipative solitons [11].

### I.2.3. Pulse in the normal dispersion regime: Similaritons

#### I.2.3.1. Similariton theory

Similariton is an asymptotic wave-breaking free solution of the GNLSE in normal dispersion regime with gain (Equation I.28) identified by Fermann and coworkers [12]. Such pulses present a parabolic intensity profile and a quadratic phase (Equation I.29-30). This pulse propagates self similarly maintaining its parabolic shape. It is subject to exponential scaling of its amplitude, temporal and spectral widths (Figure I-6). To generate those pulses nonlinear effects are to be predominant over dispersion. The generated second order phase has to come mostly from SPM in order to get a spectral bandwidth of some tens of


BY-NC-ND

nanometers. Therefore $L_{NL}$ will be much shorter than $L_D$. The envelope, phase and duration as functions of the position along the fiber are given by Equation (I.28) to (I.30).

$$A(z,t) = A_0(z)\sqrt{1-(t/T_0(z))^2}\,\exp(i\varphi(z,t)) \text{ for } |t| \le T_0(z) \qquad \text{(I.28)}$$

$$\varphi(z,t) = \varphi_0 + 3\gamma/(2g(z))A_0^2(z) - g(z)/(6\beta_2)t^2 \qquad \text{(I.29)}$$

$$T_0(z) = 3g(z)^{-2/3}(\gamma\beta_2/2)^{1/3}E_{IN}^{1/3}\exp(g(z)z/3) \qquad \text{(I.30)}$$

g(z) is the distributed gain coefficient, $E_{IN}$ the initial pulse energy and $\varphi_0$ is an arbitrary constant. For an amplifier with constant gain, any kind of pulse is to converge to this solution if the initial condition (mainly energy) is close enough.

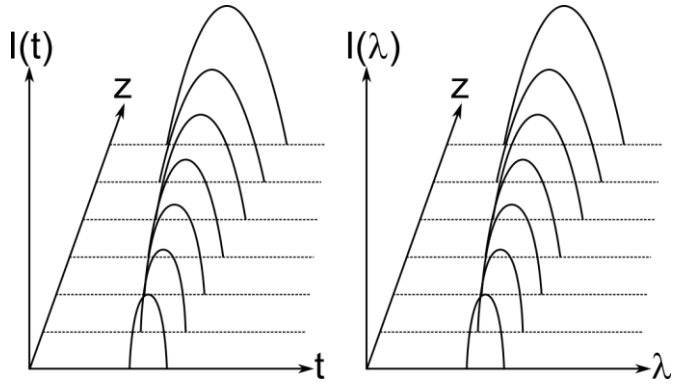


Figure I-6: Illustration of self similar evolution of the temporal (left) and spectral (right) shapes of a similariton along its amplification.

The maximal energy Ê that an amplified similariton can contain is equal to:

$$\hat{E} = \frac{c}{8gn_2}\frac{D^2(\Delta\lambda)^3 A_{eff}}{\lambda} \qquad \text{(I.31)}$$

with $\Delta\lambda$ the full spectral bandwidth and *g* the distributed gain in Np/m. To increase the energy, one can increase $A_{eff}$ or operate the amplifier at high normal dispersion. If the energy within the pulse becomes greater than what is predicted by Equation I.31, the pulse will not be a similariton anymore nor will it be compressible to its Fourier limit. Figure I-7 shows the energy scalability enabled by similaritons according to the dispersion for four different effective areas spanning from 100 to 400 µm². These curves were calculated with a distributed gain g = 1.9 Np/m, a full spectral bandwidth of 105 nm centered at 1.9 µm.


BY-NC-ND

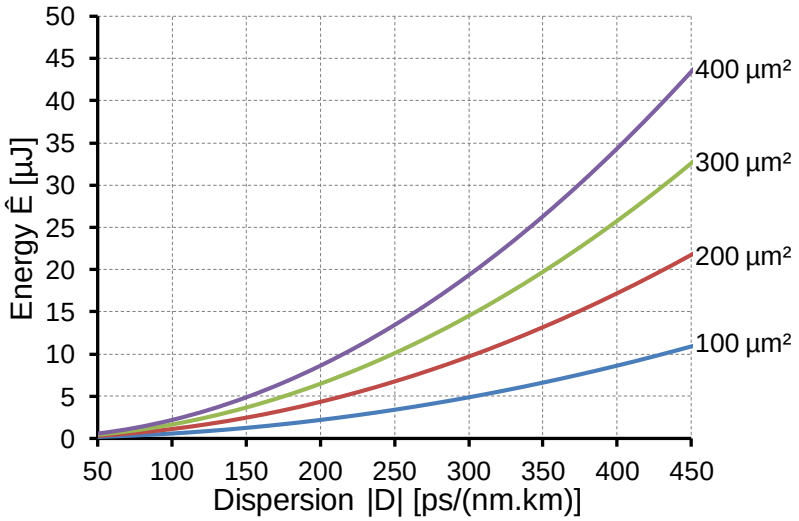


Figure I-7: Calculated maximal extractible energy, before wavebreaking, of an amplified similariton centered at 1.9 µm as a function of the absolute value of the dispersion coefficient for various modal effective areas.

It appears clearly that the maximum extractable energy before wavebreaking can be very high thanks to the temporal breathing in the amplifier. In the following, I will use a figure of merit (FOM) to easily compare the fiber. This FOM is directly linked to the energy a similariton propagating in the fiber and is given in Equation (I.32):

$$FOM = D \times A_{eff} \qquad \text{(I.32)}$$

Commercially available fibers providing normal dispersion around 2 µm such as the UHNA series from Nufern ($D$ = -55 ps/(nm.km) and $A_{eff}$ = 18 µm²) present a FOM of 1 femtosecond and will be a base for comparison.

### I.2.3.2. Similariton laser

Amplified similaritons have a pulse duration and a spectral bandwidth which are both broadening along the propagation. Hence, the output pulse can reach shorter durations compared to the input pulse and more energy can be stored within the pulse. A useful feature of these pulses is that the chirp of self-similar pulses is linear. The pulse can be easily compressed to the Fourier-transform limit by passing through a dispersion compensating line. The parabolic amplification intrinsically produces broadband spectrum without wave breaking. They are very sensitive to phase terms of order above two: gain bandwidth, third order dispersion of the amplifying fiber and of the output compressor and SPM. However, some studies shown that third order phase terms could be compensated by SPM when fine tuning the amplifier gain [13]. For rare-earth gain media emitting in the anomalous dispersion region of silica (>1.3 µm), it is difficult to achieve parabolic amplification. The commonly used way to produce normal dispersion in an Er- or Tm-doped fiber is to shrink down the core diameter. This comes with a reduced $A_{eff}$ and increased


BY-NC-ND

nonlinearity, hence less room for energy scaling. Nevertheless, oscillators delivering pulses presenting self-similar features have been reported [12]–[15]. Peng and coworkers demonstrated an all-fiber similariton oscillator using 1.3 m of a small core Erbium doped fiber producing -51 ps/(nm.km) at 1.55 µm. In order to meet a cavity resonance, which is contradictory with an endlessly broadening similariton, 2.7 m of anomalously dispersive single mode fiber were used to impose temporal breathing. The mode-locking was realized by means of NPE in the ring cavity. The output coupler was placed before the piece of singlemode fiber so as to extract uncompressed pulses. This oscillator delivers 700 fs pulses with a spectral bandwidth of 20 nm containing 0.13 nJ of energy at a repetition rate of 47.6 MHz.

## I.3. Ultrafast high power amplifiers

### I.3.1. High energy chirped pulse amplifier

The chirped pulse amplification has first been proposed by Strickland and Mourou [18] and relies on limiting the Kerr effect by using pulses with low peak power. The pulse is temporally stretched before amplification and recompressed afterwards. The peak power is therefore minimized along the amplification. In order to realize the stretching and compression steps, dispersive components generating second order spectral phase are required. On one hand, singlemode fibers and Bragg gratings (fiber or bulk) are commonly chosen to stretch the pulse to a few hundreds of picoseconds [18], [19], whereas for few nanoseconds pulses dispersive lines with diffraction gratings are used [1]–[3]. In those conditions, it is possible to decrease the peak power by a factor equal to the stretching factor, around $10^4$ in [20]. Furthermore, the sign and value of the chromatic dispersion in the amplifier does not matter anymore. On the other hand, the compression line must compensate the stretcher but also the dispersion and nonlinear phase produced by the amplifier. Let us consider a CPA scheme as depicted in Figure I-8 taken from [21]. The general setup, before the last stage of amplification, is composed by a femtosecond oscillator at a high repetition rate (MHz) delivering low average power (milliwatts [21] to Watt [20]) and one or two stages of preamplification to increase the average power. In order to reach high energy, hence high peak power after compression, it is compulsory to decrease the repetition rate of the input pulses of the last stage amplifier. To do so, a pulse picker, commonly realized with an acousto-optic modulator as in Figure I-8, is used.


BY-NC-ND

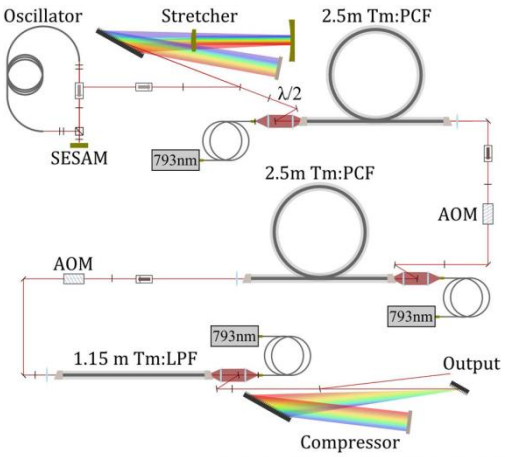


Figure I-8: Experimental setup of a CPA [21]. (AOM: Acousto-optic modulator, PCF: Photonic crystal fiber, LPF: Large pitch rod-type fiber).

To obtain highly energetic pulses with a high peak power, the repetition rate must be low (kHz range) [19]–[21]. The fiber core of the high power amplifier must be as large as possible to avoid any nonlinear effect.

Very recently, the record peak power of 1.74 GW has been set by Gaida and coworkers [21] in a Thulium-doped large-pitch fiber by transposing the technique from 1 µm to 2µm. The seed laser was a mode-lock thulium doped fiber laser emitting around 0.5 nJ pulses at a repetition rate of 33 MHz. The pulses were then temporally stretched to 0.6 nanoseconds. The repetition rate was decreased twice to reach 61 kHz. The two preamplifiers allowed reaching an energy pulse of 0.8 µJ to seed the amplifier. The main amplifier was composed of 1.15 m long Thulium-doped large-pitch rod-type fiber presenting an 81 µm core diameter. Backward propagating pump was guided by an airclad. The output pulse duration was 800 ps containing 570 µJ. Due to the transmission efficiency of the compression line, the energy contained in recompressed 270 fs pulses was 470 µJ. The average power was 28.7 W and the peak power was 1.74 GW. Limitations arose from the fact that a large bandwidth of the Thulium emission range overlaps with water absorption lines. To avoid those absorption lines, the authors shifted the central spectrum above 1.95 µm and operated in a climate chamber with reduced humidity. The thulium cross sections being higher in the water absorption bandwidth, differential losses have to be put on shorter wavelength to obtain proper amplification above 1.92 µm.

As said earlier chirped pulse amplification is a linear amplification. Experimentally those amplifiers allow reaching high peak power. This will have direct influence over the pulse phase and on the extracted pulse peak power. When considering power amplification, the non-uniformity of the gain over the considered bandwidth will lead to a pulse asymmetric spectral profile and phase which are difficult to compensate in the last step of compression.


BY-NC-ND

The amplified spectrum can be quite different compared to the input spectrum. This can be explained by different phenomena.

On one hand, as the spectral components of the pulse are temporally distributed, the pulse edge can strongly deplete the gain of the amplifier resulting in an unbalanced spectrum with a higher amplification of shorter wavelengths when the dispersion is anomalous and of longer wavelengths when the dispersion is normal. This phenomena has been observed by Gaida and coworkers [21] in the normal dispersion regime. A spectral deformation during the power amplification was observed (Figure I-9(a)). The gain saturation favored the amplification of shorter wavelengths.

Furthermore, the gain spectral profile also plays a key role. The emission cross-section variation over a broad spectrum at high level of amplification induces gain spectral shrinking which directly impacts the pulse duration and temporal shape [22].

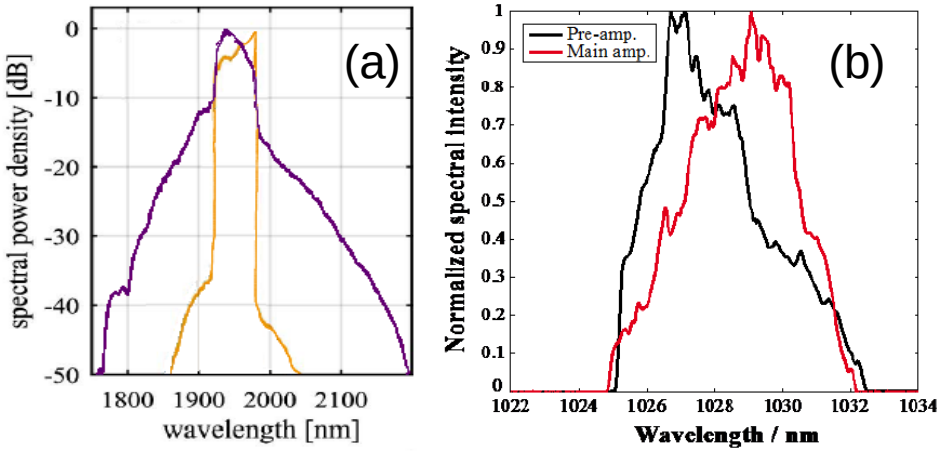


Figure I-9: Experimental spectrum measurements: (a) before two stages of amplification (yellow) and at the output of the main amplifier (purple) by Gaida and coworkers [21], (b) main amplifier input (black) and output (red) by Eidam and coworkers [19].

The pre-compensation of these effects can be realized by shaping the pulse seeding the amplifiers [21]. This yields a balanced temporal and spectral shape of the recompressed pulse.

The linear amplification based on chirped pulse amplification is one of the best candidates for energy scaling in ultrafast fiber optics. It relies on using large mode area single mode fibers which is also its main flaw. By endlessly widening the singlemode core diameter, the fiber becomes more of a bulk than a guiding medium thus forbidding coiling and all-fiber format integration. If an all-fiber format is desired, the energy scaling is drastically lowered to a few microjoules. Nonetheless, Gaponov and co-workers [23] and Tan and co-workers [24] demonstrated the possibility to reach the microjoule milestone in an all-fiber format. In [23], a MOPA scheme is used with an oscillator emitting at 1.94 µm. The highest peak power reached in their configuration was 2.4 MW (4 µJ of energy contained in


BY-NC-ND

1.6 ps). In [24], the pulses originated from an Er-doped fiber amplifier were Raman-shifted around 1.97 µJ before entering two stages of amplification. The use of high pump power (over 140 W at 793 nm) in the last stage allowed reaching 3 MW peak power for recompressed pulses (241 fs of pulse duration containing 700 nJ of energy). These results represent the benchmark for our aimed parabolic amplification

### I.3.2. High energy parabolic amplifier

In the parabolic amplifier, the goal is to take advantage of nonlinear effect by exploiting an auto-similar propagation regime. The generated second order phase has to mostly come from SPM. The goal is to get a spectral bandwidth of some tens of nanometers. Therefore, $L_{NL}$ is shorter than $L_D$. A transform-limited ultrashort pulse propagating in such an amplifier will have its temporal and spectral shapes tend towards parabolic profiles [12]. The pulse will therefore be a similariton as described in I.2.3.

The work realized by Zaouter and coworkers in 2008 emphasized the benefits and drawbacks of parabolic amplification in an Ytterbium doped large mode area photonic crystal rod-type fiber. The amplifying fiber was 85 cm long and presented an 80 µm core diameter. This single mode fiber presented an effective modal area of 3850 µm². The calculated nonlinear length was a hundred times lower than the dispersion length. The active fiber was backward pumped. It was directly seeded by an ultrafast oscillator delivering 330 fs pulses with a spectral bandwidth of 3.9 nm containing 170 nJ of energy at a repetition rate of 10 MHz. A specifically designed compressor and adjusted pulse energy allowed the generation of short pulses while keeping a high quality temporal shape. Third order phase management has been optimized through those parameters. The best performances, in terms of peak power (16 MW), were obtained for pulses of 70 fs with a limited energy of 1.25 µJ without lowering the repetition rate. The amount of power in the main peak was 89%. The pulse duration was limited by the spectral filtering imposed by the compressor.

At 1.55 µm Peng and coworkers [15] used an Erbium doped fiber with -51 ps/(nm.km) dispersion, seeded by the similariton oscillator described in [25]. The amplifier was forward- and backward core-pumped. At the output of this nonlinear amplifier, the output pulse was compressed using standard singlemode fiber to keep an all-fiber format. The 113 fs duration pulse contained 4.1 nJ (54 kW peak power). Since a similariton was amplified the pulse had a pedestal-free temporal shape and a smooth spectrum. According to the authors, the only limitation to power scaling was due to the available pump power of the amplifier.

Table I-1 summarizes the different references that have been focused on.


BY-NC-ND

Table I-1: References performances summary. In green are underlined the aimed performances. In red are represented the unwanted charateristics

| Reference | Gaida [21] | Gaponov [23] | Tan [24] | Zaouter [13] | Peng [15] |
|---|---|---|---|---|---|
| **Amplifier architecture** | Tm CPA | Tm CPA | Tm CPA | Yb **Similariton** | Er **Similariton** |
| **Year** | **2016** | **2016** | **2016** | **2008** | **2012** |
| **$E_{out}$ [µJ]** | 470 | 4 | 0.7 | **1.25** | 0.0041 |
| **$\Delta t_{out}$ [ps]** | 0.27 | 1.6 | **0.241** | **0.07** | 0.113 |
| **Peak power [MW]** | **1740** | 2.5 | 3 | **16** | 0.54 |
| **Repetition rate [kHz]** | 61 | 92 | 34800 | **10000** | 47600 |
| **Amplifier fiber type** | Rod | **All-fiber** | **All-fiber** | Rod | **All-fiber** |
| **Amplifier fiber core diameter [µm]** | 81 | **10** | **25** | 80 | ~3 |
| **FOM [fs]** | | | | **130** | 1.5 |

Up to now, to our best knowledge, there is no demonstration of similaritonic amplification at 2 µm. In this thesis, I've tried to pave the way to this demonstration by designing gain fibers with normal dispersion. This is the objective of the second chapter of this manuscript.

## I.4. Conclusion

Over the past years, energy scaling of ultrashort pulses in all-fiber format lasers has been mostly realized via mode area tailoring, culminating in the use of parabolic amplification (dissipative solitons) in all-normal dispersion (ANDi) lasers at 1 µm, where silica exhibits normal dispersion. This attractive amplification regime is prohibited at 2 µm due to large anomalous dispersion of silica. According to Eq. (I-31) the best all-fiber amplifier at 2 µm would need a special Tm-doped fiber with both increased $D$ and $A_{eff}$. It is impossible to design a single mode fiber with large mode area and high $-D$ at 2 µm since waveguiding effects are inhibited by nature in large mode area singlemode fibers. On the other hand, Poole *et al.*, from the Bell Labs [26], showed that high-order modes in optical fibers could be used for dispersion control. These modes might exhibit high $-D$ and large mode area near their respective cut-offs. They are therefore suited to energy scaling at 2 µm via parabolic amplification. To our best knowledge, no rare-earth doped version of this design has been produced to date.

The goal of this thesis is to pave the way towards the demonstration of parabolic amplification at 2 µm. To achieve this goal, the manuscript is organized in three chapters. First, a fiber gathering all attributes necessary to initiate parabolic amplification at 2 µm (gain, normal dispersion and large mode area) designed at XLIM and fabricated by MCVD at IRCICA/PhLAM is presented. The second chapter reports on the first, to our knowledge, spatial mode converter efficient over a broad bandwidth from 1.55 µm to 2 µm. The device was designed, fabricated and characterized at XLIM. In the second chapter, I also present a


BY-NC-ND

source of ultrashort pulses tunable between 1.8 and 2.1 µm that has been designed, built and characterized at XLIM in order to seed the nonlinear amplifier. In the third chapter, a numerical study of the potential of the designed fiber to achieve high energy similariton is presented.


BY-NC-ND

Similariton amplification was achieved in singlemode silica-based fibers at 1.55 µm. However, the energy contained in the pulse is three orders of magnitude lower than that achieved at 1 µm. This is mostly due to the small-core design used to achieve normal dispersion in the gain media. Following Equation I.31, the higher the dispersion and/or the effective mode area, the higher the energy. However, the way to generate normal dispersion in single mode fiber is to reduce the fiber core and increase the core refractive index hence reducing the effective mode area. New ways of generating both high normal dispersion and high effective mode area values in silica-based fibers are required to enable power scaling based on auto-similar amplification at wavelengths where silica exhibits anomalous dispersion.

In the early 90's, the emergence of erbium-doped fiber amplifiers operating in the third telecommunications window allowed information transmission over thousands of kilometers in single mode fibers without any electronic regeneration. Dispersion compensation had quickly been required when considering short pulses propagating in a dispersive media over such long distances. A way to compensate silica dispersion in the erbium C-band has been proposed by Poole and coworkers [26] from Bell Labs by taking advantage of the fact that a higher order mode approaching its cutoff wavelength would produce high normal dispersion. They used a two-mode fiber guiding the fundamental $LP_{01}$ and the first higher order mode, namely the $LP_{11}$. The large waveguide dispersion of $LP_{11}$ near its cutoff arises from the strong wavelength dependence of its electric field distribution (Equation I.16). When a higher order mode approaches its cutoff, it will spatially leak away from the core to the cladding. The overlap of the $LP_{11}$ with the core decreases as the wavelength is increased toward cutoff. The generated dispersion will be negative since the core has a higher refractive index than the cladding. If the mode would leak from a low refractive index media to a high refractive index media, the dispersion would be positive. By doing so, not only has the generated dispersion the required sign to compensate the silica dispersion, but the effective mode area of the mode inherently increases as it approaches the cutoff. The experiment conducted by Poole and coworkers relied on the use of two distinct two-mode fibers. The first one had a cutoff wavelength of 1.93 µm and the specificity of matching the effective indices of the $LP_{01}$ and the $LP_{11}$ around 1.55 µm. This fiber was used to favor the conversion from the fundamental mode to the high order mode. The other fiber had a cutoff wavelength of 1.64 µm and was used as the dispersion compensating fiber. Mode conversion was realized by applying strain on the first fiber by a gold wire wrapped around the bare fiber. The dispersion measured at 1.55 µm was -228 ps/(nm.km) for the $LP_{11}$


BY-NC-ND

and +22 ps/(nm.km) the $LP_{01}$. The overall loss of the device comprising mode converter and different splices was 0.36 dB. Pulses at carrier wavelengths from 1533 nm to 1551 nm could be recompressed in that way.

Higher mode (HOM) fibers were also used for their ability to propagate large single modes. Ramachandran and coworkers [27] demonstrated the excitation and propagation over 5 meters of a $LP_{07}$ mode in a HOM fiber. The mode exhibits 2100 µm² effective area and anomalous dispersion of +35 ps/(nm.km). The HOM fiber design was based on two concentric waveguides. The center core was singlemode. The surrounding core of around 80 µm diameter guides HOMs up to at least the $LP_{07}$. The mode conversion between the fundamental $LP_{01}$ of the center core to the $LP_{07}$ of the multimode core was ensured by long period gratings. This HOM fiber was used as a dispersion compensation element in an Er-doped fiber laser. The active single mode Er-doped fiber exhibits normal dispersion provided by a small–core design. The amplifier was seeded by femtosecond pulses containing 17 pJ of energy at a repetition rate of 46 MHz. The output pulses were strongly chirped due to the normal dispersion regime of the amplification and carried 14 nJ of energy. After 5 m of propagation in the higher order mode of the HOM, the pulses were compressed to 152 fs presenting 61 kW peak power. As the HOM fiber presented a $L_D/L_{NL}$ of 1 some SPM and spectral features were expected during the pulse propagation. The spectral shape of the input pulse was somewhat preserved along the HOM fiber and even after the maximum pulse compression. This method allowed reaching rather high peak power without provoking wavebreaking. Indeed, the authors replaced the HOM fiber by a SMF and the spectrum was strongly broadened.

Another type of higher order mode fibers was used as a gain media to improve the energy scalability of amplifiers. Peng and co-workers [28] used a 2.65 m long Er-doped HOM fiber propagating several higher order modes. The $LP_{0,11}$ of this fiber presented a 6000 µm² effective area. The conversion to and from this higher order mode was realized with two broadband (approximately 150 nm around 1.525 µm) LPGs for both the pump Raman laser at 1.48 µm and signal at 1.553 µm with nearly 99% efficiency. The conversion at the pump wavelength allowed maximum pump-signal overlap, high pump absorption and reduced amplifier length. The input pulses presented less than 500 fs duration containing 0.6 µJ at a repetition rate of 25 kHz. They could be amplified from 16 µJ to 595 µJ in the HOM amplifier without any spectral distortion. The compression line had a 50% efficiency but allowed to reach less than 500 fs pulse duration thus producing over 600 MW peak power. The mode at the output of the HOM amplifier was converted back in a coreless fiber with an 8° end cap to obtain high beam quality. By using a higher order mode in their amplifier the authors proved


BY-NC-ND

that energy scaling could be realized in these high order modes if extra care is taken in the mode conversion.

Note that the dispersion-tailored HOM fiber and large-mode-area (gain) HOM fiber, although named in the same way, are essentially different by design. Up to now, to our knowledge, there is no dispersion-tailored HOMF exhibiting gain and large mode area.

Tailoring the dispersion and the effective area in a rare-earth-doped high order mode fiber could open the path towards power scaling in optical fibers, through direct amplification in normal-dispersion regime.

### II.1. Principle of operation

In cylindrically symmetric fibers, it has been shown that the waveguide dispersion $D_W$ originates from the variation of the radial electric field distribution *E(r)* with wavelength. The modal contribution to the dispersion can be expressed in a convenient form as:

$$D_W \propto \lambda \int_0^\infty \left( \frac{dE(r)}{dr} \right)^2 r dr + \lambda^2 \frac{d}{d\lambda} \left( \int_0^\infty \left( \frac{dE(r)}{dr} \right)^2 r dr \right) \qquad \text{(II.1)}$$

The first term on the right hand side of Eq. (II.1) is always positive whereas the second one can be either negative or positive depending on the spectral variation of the slope of *E(r)*. Usually, *E(r)* spreads out of the core when the wavelength is increased. Thus, *dE(r)/dr* decreases whatever *r*, with increasing wavelength. Consequently the second integral in the right-hand side is a decreasing function of $\lambda$, leading to a negative second term. Therefore, the modal contribution to dispersion is usually negative. To increase the value of the negative dispersion, so as to compensate for the anomalous dispersion of silica it is therefore necessary to increase the rate of spectral variation of *dE(r)/dr*. This effect can be obtained in the vicinity of the cut-off wavelength of a peculiar mode. The fundamental mode has an infinite cut-off wavelength and is therefore not suitable to this purpose. On the other hand each high-order mode has finite cut-off wavelength. In Figure II-1, we consider the first cylindrically symmetric high-order mode, *i.e.* the $LP_{02}$ mode, when it is approaching its cut-off. As the wavelength increases the guided mode tends towards a plane wave in the infinite cladding medium. The slope *dE(r)/dr* is strongly changing slightly below $\lambda_{cut\text{-}off}$, thus producing high negative dispersion. This effect corresponds to a strong inflexion in the modal effective index curve which tends towards the cladding index at the cut-off. According to Eq. (II.1) this inflexion produces high $-D_W$. Few mode step-index fibers have been designed so that a high-order mode cuts off in the telecom window ($\lambda$ = 1.56 µm) [26]. The high-order mode presenting high normal dispersion (-288 ps/nm/km) was used in a dispersion compensating device or to recompress pulses from a mode-locked laser.


BY-NC-ND

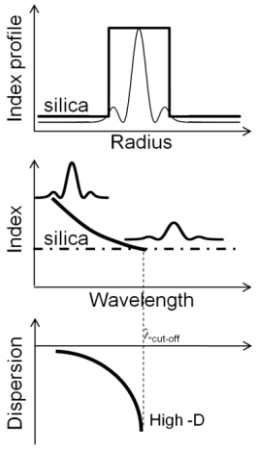


Figure II-1: Principle of operation of a moderately multimode fiber for dispersion control. Top: Generic profile of a step-index moderately multimode fiber. Associated $LP_{02}$ intensity profile. Middle: $LP_{02}$ mode effective index versus wavelength. Insets show the field spreading when $\lambda$ increases. Bottom: $LP_{02}$ dispersion versus wavelength.

## II.2. Design criteria

A key issue in the design of few mode fibers is which higher order mode the signal is to propagate in. Since our goal is high normal dispersion values, one could naturally tend to choose the mode that gives the most desirable dispersion characteristics. However, it turns out that other design issues limit the choice of mode.

The most important amongst these issues is mode beating, also called multi-path interference (MPI), that causes pointing instabilities and noise at the output of a laser. Generally speaking, in order to limit MPI, one should limit the number of guided modes, and thus the possible interference paths in the few mode fiber. This means that the signal should propagate in the lowest order mode that still provides the required dispersion characteristics. For example, as in [26], if we were to select the $LP_{11}$ mode as the propagation mode, then it would be possible to design a fiber with only two guided modes ($LP_{01}$ $LP_{11}$). On the other hand, if we were to select the $LP_{03}$ mode there would have nine guided modes ($LP_{01}$, $LP_{11,}$ $LP_{21}$, $LP_{02}$, $LP_{31}$, $LP_{12}$, $LP_{41}$, $LP_{22}$, and $LP_{03}$). This means that even if the $LP_{03}$ was to exhibit particularly attractive dispersion properties, the increased MPI due to the mode coupling to other modes would be prohibitive. MPI is a measure of mode coupling. Mode coupling will decrease with increasing difference between the effective indices of two considered modes. This characteristic of few-mode fiber can be tailored by design of the refractive index profile.

A second important consideration is polarization dependent behavior. Modes that are not cylindrically symmetric are by nature more susceptible to polarization effects. This effectively restricts the selection of modes to those with cylindrical symmetry, *i.e.*, $LP_{0m}$.

The preceding discussion basically means that the $LP_{02}$ mode is the logical choice for the propagation mode in few mode fibers for dispersion tailoring. In fact, we will see that with


BY-NC-ND

proper fiber design this mode also provides the required dispersion properties. Working near the cut-off is however troublesome. First, any local changes in index will result in cutting-off the mode at a non-desired wavelength. Second, the dispersion slope is very steep and cannot be engineered. Third, working close to the cut-off may imply excess bending loss. This step index RIP hence brings limited flexibility.

### II.3. Improved design

Ramachandran [29] has proposed an improved design of such a few mode fiber (see Figure II-2). The $LP_{02}$ is the mode of interest. The complex RIP incorporates a central high-index multimode core, an adjacent down-doped trench and one high-index ring. The ring confines the $LP_{02}$ mode and therefore rejects the cut-off wavelength towards longer wavelengths, hence providing low loss operation in the telecom window. The ring provides a smooth dispersion variation that allows slope dispersion tailoring. The dispersion magnitude is tuned by the trench.

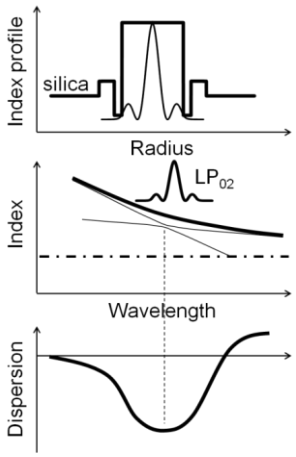


Figure II-2: Principle of operation of an improved design of a few mode fiber for dispersion control. Top: Generic index profile of a few mode fiber. Associated $LP_{02}$ intensity profile. Middle: $LP_{02}$ mode effective index (thick black curve) is a linear combination of the 'core' mode and of the 'ring' mode. The inflexion causes high $-D_W$ around the phase-matching point. The effective index of the $LP_{02}$ is increased above the silica index ensuring low loss guidance. Bottom: $LP_{02}$ dispersion versus wavelength. The additional features (trench, ring) help tailor the dispersion and dispersion slope.

As shown in Figure II-3(b) very high normal dispersion (–500 ps/nm/km) can be reached in this fiber design. The high negative dispersion associated with the low dispersion slope can be useful when considering an application as a parabolic amplifier.


BY-NC-ND

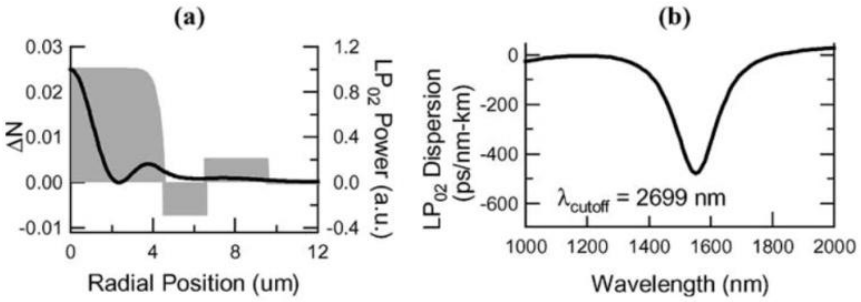


Figure II-3: (a) $LP_{02}$ mode profile at the most dispersive wavelength (solid line) in a few mode fiber (RIP: gray background). (b) Corresponding plot of $LP_{02}$ dispersion versus wavelength. $\lambda_{cut\text{-}off}$ represents the wavelength at which the $LP_{02}$ mode leaks in the cladding [29].

### II.4. Modeling towards optimal design

In the following I present the various steps to design few mode fibers in the context of high-energy amplifiers. I am searching for designs presenting high normal dispersion values, broad wavelength spectrum, large effective mode area and low multi-path interference. MPI will be evaluated through the difference in effective index between the desired mode ($LP_{02}$) and its nearest neighbor. I have concentrated the study on the three-layer profile shown in Figure II-4.

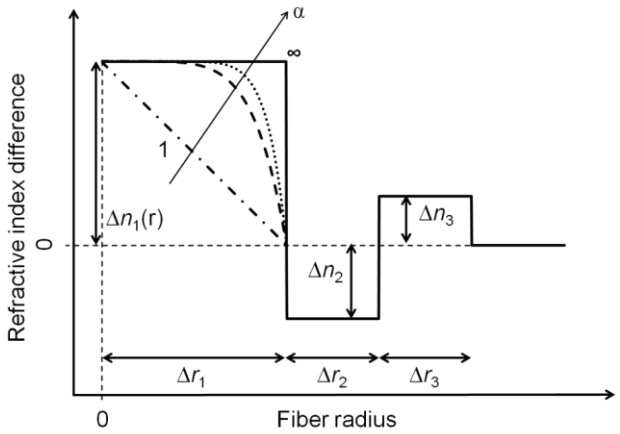


Figure II-4: The various parameters of a typical few mode fiber for dispersion control.

The graded index core is defined by $\Delta n_1(r)$ and $\Delta r_1$. $\Delta n_1(r)$ is given by the following formula:

$$\Delta n_1(r) = \Delta n_1 \sqrt{\left(1 - 2\Delta\left(\frac{r}{\Delta r_1}\right)^{\alpha}\right)} \qquad \text{(II.2)}$$

where $\Delta n_1 = \Delta n_1(0)$, $\alpha$ is the gradient order and $\Delta$ is the relative index difference defined by:

$$\Delta = \frac{(n_4 + \Delta n_1)^2 - n_4^2}{2(n_4 + \Delta n_1)^2} \qquad \text{(II.3)}$$


BY-NC-ND

where $n_4$ is the cladding index, chosen to be equal to that of pure fused silica. $\Delta n_2$ and $\Delta r_2$ are the trench parameters. $\Delta n_3$ and $\Delta r_3$ are the ring parameters.

The profile comprises seven degrees of freedom: three index differences, three thicknesses and the gradient order. It is therefore very unlikely to find a convenient set of parameters from nothing. I have therefore considered the RIP from [29] as a seed:

Table II-1: Refractive index profile from [29]

| | $\Delta r$ | $\Delta n$ |
|---|---|---|
| Core | 4 | $25\times10^{-3}$ |
| Trench | 2.5 | $-8\times10^{-3}$ |
| Ring | 3.5 | $4\times10^{-3}$ |

I have taken $\alpha = 6$ to match the RIP in [29] and then used the scaling properties of Maxwell equations to find a suitable RIP operating at 2 µm. Let us consider the original RIP with parameters $\Delta n$ and $\Delta r$, the scaled RIP with $\Delta n^*$ and $\Delta r^*$, and the scale factors $a$ and $b$ are such that:

$$\Delta n^* = a\Delta n \tag{II.4}$$

$$\Delta r^* = b\Delta r \tag{II.5}$$

The scalar wave equation for the two index profiles will be the same when the wavelength $\lambda$ is scaled as:

$$\lambda^* = b\sqrt{a}\lambda \tag{II.6}$$

The waveguide dispersion $D_W$ then scales according to:

$$D_W^* = \frac{\sqrt{a}}{b} D_W \tag{II.7}$$

According to Eq. (II.4-7) a nominal RIP can be scaled in index and/or in radius to provide any dispersion at any wavelength. The scaling rules have also an important practical aspect: when drawing a fiber during manufacturing, the outer diameter of the fiber as well as all other transverse dimensions may be altered by altering the drawing conditions. This results in scaling of the fiber profile, and allows fine tuning of the dispersion properties during manufacturing.

The original RIP used the deepest trench that can be achieved ($\Delta n_2 = -8\times10^{-3}$) [30]. However, IRCICA-PhLAM, our technological partner, is limited to $\Delta n_2 = -4\times10^{-3}$. $\Delta n$ was then scaled by a factor $a = 1/2$ to cope with this technological limitation. The operating wavelength is then scaled by the inversed squared root of 2. The wavelength of highest $-D_W$ is then


BY-NC-ND

shifted from 1.55 to 1.1 µm. The highest $-D_W$ thus becomes –350 ps/(nm.km). I have then scaled the fiber radii by a factor $b = 2$ in order to shift the operating wavelength to 2.2 µm. The highest $-D_W$ thus becomes –175 ps/(nm.km). The scaled RIP is given in Table II-2 and presents a FOM of 34 fs.

Table II-2: Original and scaled RIP for an operation around 2 µm.

| | Original RIP [29] | | Scaled RIP | |
|---|---|---|---|---|
| | $\Delta r$ | $\Delta n$ | $\Delta n^* = 0.5\Delta n$ | $\Delta r^* = 2\Delta r$ |
| Core | 4 | $25\times10^{-3}$ | $12.5\times10^{-3}$ | 8 |
| Trench | 2.5 | $-8\times10^{-3}$ | $-4\times10^{-3}$ | 5 |
| Ring | 3.5 | $4\times10^{-3}$ | $2\times10^{-3}$ | 7 |
| $\lambda$ [µm] | 1.55 | | 2.2 | |
| D [ps/(nm.km)] | –500 | | –175 | |

This is certainly not the highest $-D_W$ that one can achieve with this technique. The scaled RIP is however a seed for further numerical optimization. In the following we will consider the scaled RIP as the nominal values. As mentioned above each part of the RIP influences the dispersion curve. As shown in Figure II-5, the $LP_{01}$ mode is guided by the core. The $LP_{02}$ is mainly guided by the core but is also dependent on the trench and ring parameters. As shown in Figure II-2, middle, the $LP_{02}$ is accompanied by the $LP_{03}$ which results from the coupling between the 'core' $LP_{02}$ and the 'ring' $LP_{01}$. As shown in the bottom inset of Figure II-5 it is mainly guided by the ring.

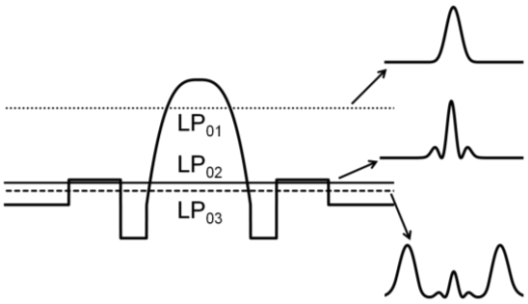


Figure II-5: The various $LP_{0m}$, in intensity, of a typical few mode fiber for dispersion control with their effective index position according to the RIP.

First, the $LP_{03}$ index curve is convex leading to high anomalous dispersion. Second, $n_{e02}$ and $n_{e03}$ are very close. This may lead to MPI. Great care must be taken to cut this parasitic mode, *i.e.* keep its effective index close or even below that of silica, while preserving the $LP_{02}$ mode. Therefore, in order to lower the $LP_{03}$ guidance, we will have to decrease the influence of the ring.

The curvature of the effective index is tuned by the coupling strength between the core and the ring modes. A low coupling strength implies small interaction between the core and the


BY-NC-ND

ring mode and the curvature of the effective index difference will be high at the phase-matching point. This is thus accompanied by large dispersion and small bandwidth. Second the effective index difference $n_{e02}$-$n_{e03}$ will be small. A low coupling strength thus means that both modes are likely to be guided. This situation can be avoided if the core and ring are close to each other, thus limiting the trench thickness to a few microns.

In order to understand the impact of each index layer and search for optimal parameters, it is necessary to study each layer separately. I have modified the scaled RIP according to these general rules. The results are given below.

### II.4.1. Impact of the ring

The width of the ring $\Delta r_3$ was varied by –50 % to 100 % of the nominal value. Results are shown in Figure II-6.

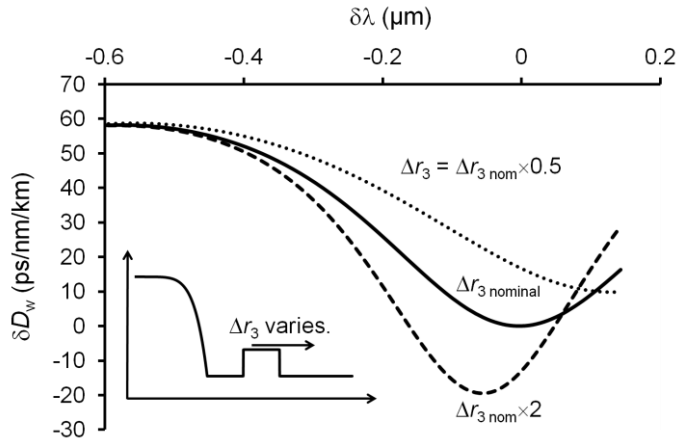


Figure II-6: Impact of the ring thickness $\Delta r_3$ on the dispersion spectrum.

Figure II-6 depicts the fact that enlarging the ring produces high $-D_W$. Second, the dispersion spectrum is shifted towards the shorter wavelengths. Enlarging $\Delta r_3$ comes down to push away the fiber cladding. Thus, it strengthens guidance of the $LP_{02}$ mode. This increase in dispersion comes with a narrowing of the spectrum in which high $-D_W$ can be achieved.

The nominal index difference of the ring $\Delta n_{3\ nom}$ was then varied by $-2\times10^{-3}$ to $+3\times10^{-3}$. Results are shown in Figure II-7.


BY-NC-ND

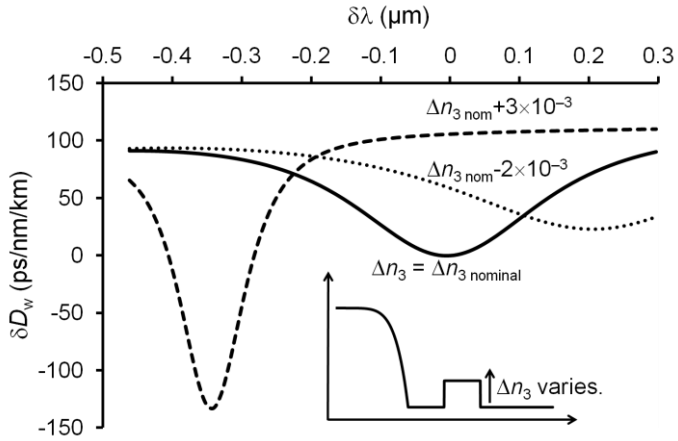


Figure II-7: Impact of the ring index difference $\Delta n_3$ on the dispersion spectrum.

The increase in $\Delta n_3$ strengthens the $LP_{02}$ guiding. The slope of the mode effective index is therefore increased. Thus, it offers access to higher $-D_W$. However, this effect comes also with a wavelength shift to the shorter wavelengths and a narrowing of the high $-D_W$ spectrum. Moreover, the $LP_{03}$ waveguidance is also strengthened, leading to possible MPI. $\Delta n_3$ must be kept on the level of $\Delta n_{3\ nom}$ or below to avoid excess MPI.

The variations in both $\Delta r_3$ and $\Delta n_3$ offer a wavelength shift and an increase in the dispersion value. However, increasing $\Delta n_3$ too much makes the dispersion slope too high and the spectrum too narrow. An increased $\Delta r_3$ does not affect the dispersion and the wavelength shift as much as $\Delta n_3$. Those shifts have to be taken in consideration when designing the RIP of the fiber to obtain the desired dispersion at the desired wavelength.

### II.4.2. Impact of the trench

I have then studied the impact of the trench. The ring has been removed. First, the width of the trench $\Delta r_2$ was varied by – 50 % to 100 % of its nominal value. Results are shown in Figure II-8.

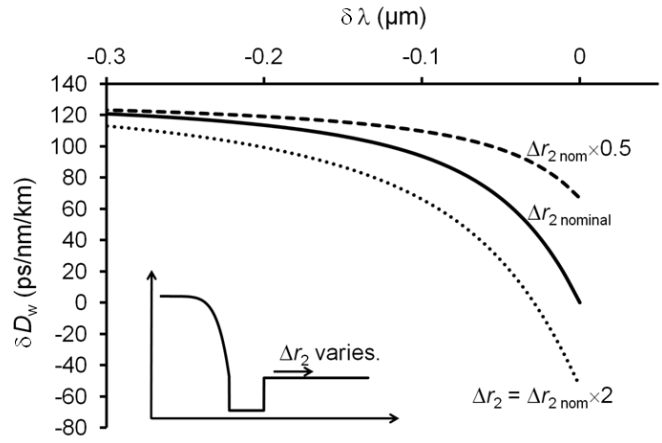


Figure II-8: Impact of the trench thickness $\Delta r_2$ on the dispersion spectrum.


BY-NC-ND

Figure II-8 shows that the thicker the trench the deeper the waveguide dispersion near the cut-off. With an increasing trench width, the $LP_{02}$ is better guided. Therefore, the slope with which the effective index arrives at the value of the cladding one is higher. Therefore, it produces high $-D_W$ near the cut-off wavelength. Increasing the trench thickness comes down to push away the cladding, thus enlarging the index difference between the core and the trench that serves as a cladding. When a ring is added to the RIP the coupling between the core and the ring mode is decreased. Therefore producing higher $-D_W$ values but narrowing the dispersion curve. Hence this situation, even if the desired effect on dispersion is obtained, is not suitable.

The index difference of the trench $\Delta n_2$ was then varied from $-1\times10^{-3}$ to $+2\times10^{-3}$. Results are shown in Figure II-9.

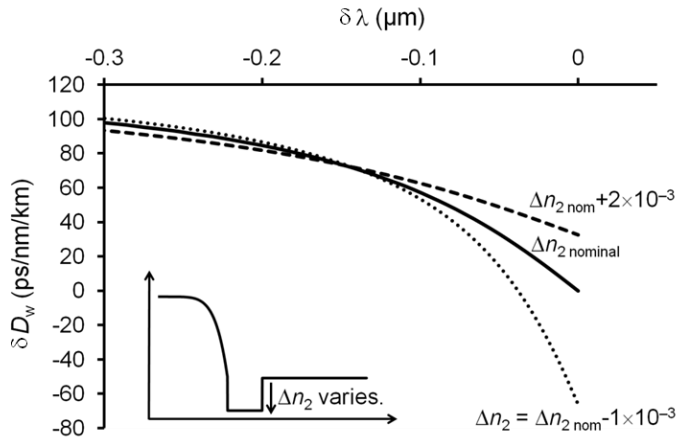


Figure II-9: Impact of the trench index difference $\Delta n_2$ on the dispersion spectrum.

Figure II-9 depicts the effect of an increased trench depth. The lower the $\Delta n_2$ the higher the $-D_W$ near cut-off.

The variations in both $\Delta r_2$ and $\Delta n_2$ offer high $-D_W$ values near the cut-off. However, an increase in $\Delta r_2$ shifts the high $-D_W$ value to the shorter wavelengths. Thus it has to be done to a certain extent. Therefore, we will have to focus on the depth of the trench to obtain high $-D_W$ values. However, the inflexion of the $n_{e02}$ curve at this point would be higher leading to a narrow bandwidth.

A summary of the different phenomena met during those simulations is available in Table II-3.


BY-NC-ND

Table II-3: Summary of the ring and trench contributions to the dispersion spectrum. ('+' stands for an increase).

| | Ring | | Trench | |
|---|---|---|---|---|
| | $\Delta n_3$ + | $\Delta r_3$ + | $\lvert \Delta n_2 \rvert$ + | $\Delta r_2$ + |
| Spectrum shifts | Strongly to the short λ | Slightly to the short λ | | |
| $\lvert D_W \rvert$ | + + | + + | + + | + + |

The trends have been used to determine an optimized RIP. The results are shown in Figure II-10.

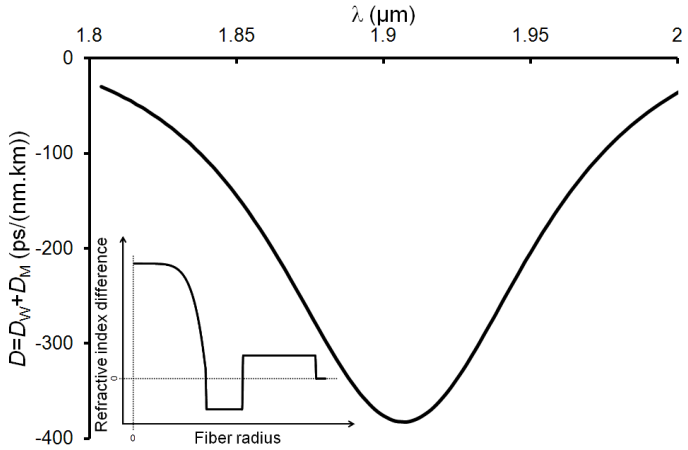


Figure II-10: Chromatic dispersion of the designed RIP versus wavelength. Inset: RIP for improved dispersion. α = 6, $\Delta n_1 = 15\times10^{-3}$, $r_1 = 8$ µm, $\Delta n_2 = -4\times10^{-3}$, $\Delta r_2 = 4$ µm, $\Delta n_3 = 3\times10^{-3}$, $\Delta r_3 = 8$ µm.

The chromatic dispersion is as high as –380 ps/(nm.km) at 1.908 µm ($\lambda_{Dmax}$). The computed $LP_{02}$ mode field area for this RIP is of 353 µm² at $\lambda_{Dmax}$. The optimal fiber presents a figure of merit ($DA_{eff}$) of 134 fs which is as high as Zaouter's [13].

### II.5. Fabricated passive few-mode fiber

A very first version of the fiber design described above was manufactured by the MCVD process at IRCICA/PhLAM. Measured RIP and dispersion curve computed for the $LP_{02}$ mode taking the actual RIP into account are shown in Figure II-11 (a-b). The high index ring is lower than expected, thus increasing the sensitivity of the $LP_{02}$ mode to the curvature. The trench is not step-like, which is expected to impact on the dispersion spectrum of the $LP_{02}$ mode. Despite the discrepancy between the target and the actual RIP, negative dispersion is obtained around 2 µm.


BY-NC-ND

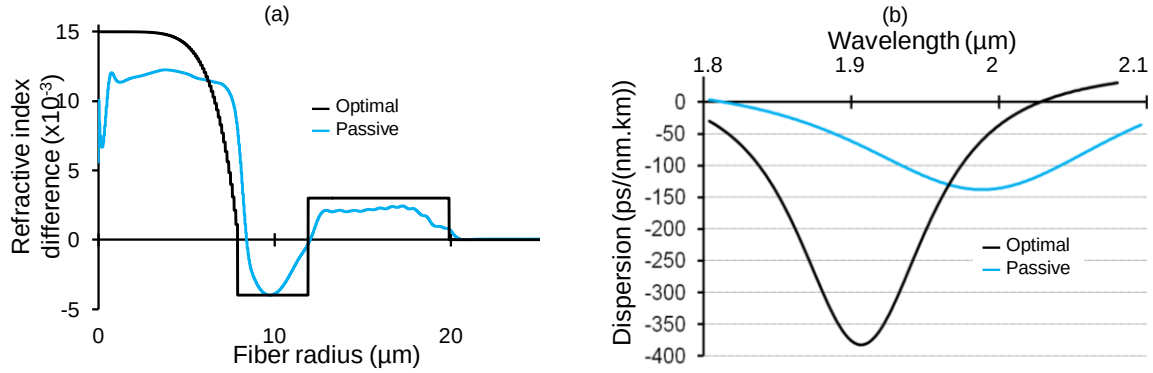


Figure II-11: (a) Measured refractive index difference of the passive (blue) few mode fiber. Black line shows the target RIP. (b) Dispersion curves computed for the two RIPs shown in (a).

The effective areas were computed at the wavelength of minimum dispersion for both fibers enabling to calculate the expected FOM. These values are summarized in Table II-4.

Table II-4: Computed dispersion and effective area of the $LP_{02}$ mode for the target and manufactured fibers at their respective $\lambda_{Dmax}$.

| Fiber | Target | Manufactured |
|---|---|---|
| $\lambda_{Dmax}$ (µm) | 1.908 | 1.99 |
| $\|D_{max}\|$ (ps/(nm.km)) | -380 | -137 |
| $A_{eff}$ (µm²) | 353 | 398 |
| FOM (fs) | 134 | 55 |

## II.6. Conclusion

It is a real scientific challenge to gather large $A_{eff}$ and high $-D$ at long wavelengths in silica fibers since in large core fibers the waveguidance is very weak, leading to negligible $D_W$. In this section, I have presented a fiber design yielding large mode area and strong waveguidance effects, leading to high normal dispersion adjustable by design to any operating wavelength. A few mode fiber maximizing $A_{eff}$ and |D| around 2 µm has been designed taking into account the limitation of the MCVD process. Then a passive fiber was manufactured by the MCVD process. The parameters computed taking the actual RIP into account are $D$ = -137 ps/(nm.km) and $A_{eff}$ = 398 µm$^2$ at the wavelength of 1.99 µm in the fluorescence band of $Tm^{3+}$ ions.


BY-NC-ND

The use of such optical fibers requires selective excitation of the highly dispersive mode or mode conversion from the input single mode fiber into the higher order transverse mode of the few mode amplifying fiber (Figure III-1).

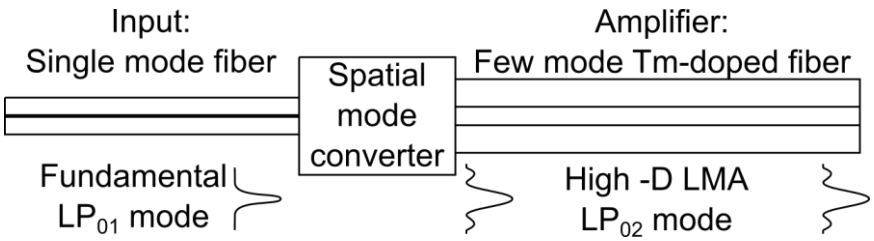


Figure III-1: Scheme of a high-order mode based amplifier. Light propagating in the $LP_{01}$ mode of the input fiber is converted to a high normal dispersion high-order mode of a few mode fiber, the $LP_{02}$ mode for instance.

The challenge in designing a good spatial mode converter is twofold:

- To transfer a maximum fraction of the energy of the input mode into the desired high-order mode,
- To match the conversion bandwidth to the *–D* spectrum.

Moreover, the modal content of these few mode fibers and how it behaves according to the excitation conditions has to be thoroughly investigated in order to make the maximum out of few mode amplifiers.

### III.1. Long period gratings with controlled bandwidth

To selectively couple the input $LP_{01}$ to the desired high-order mode, Poole and coworkers [26] have used grating coupling. Coupling occurs between two modes when the grating period $\Lambda$ is adjusted to match the intermodal beat length given in Equation III.1.

$$\Lambda = 2\pi/\Delta\beta = \lambda/\left(n_{e01} - n_{e02}\right) \qquad \text{(III.1)}$$

This resonant coupling phenomenon has a very narrow bandwidth, on the order of 1 to 3 nm, thus limiting its use in a pulsed amplifier. However, as demonstrated in [29] the bandwidth $\Delta\lambda$ is conversely proportional to the derivative of $\Delta\beta$ with respect to the wavelength, *i.e.* the group index difference. A detuning parameter ($\delta(\lambda) = 0.5(\Delta\beta(\lambda) - 2\pi/\Lambda)$) directly impacting the coupling strength between the two modes can be defined. This detuning parameter allows fine tuning of the grating period. The conversion bandwidth will be the largest as this parameter reaches zero. Therefore, the spectrum of an LPG can be tailored by adjusting the refractive index profile (RIP). However, having a large spectrum for the LPG and a tailored dispersion in this spectrum is quite a technological challenge.


BY-NC-ND

There are several techniques to write LPGs in optical fibers. The electric-arc technique [31] is independent of the fiber composition. The arc is 300 µm wide. Therefore the achievable grating period is longer than 500 µm limiting the index difference $\Delta n_e$ to values under $4\times10^{-3}$ ($\Delta n_e < 4\times10^{-3}$). Furthermore the electric arc induced by a conventional fusion splicer is not cylindrically symmetric. It makes it difficult to couple light efficiently in the $LP_{02}$ mode. The UV technique [31] requires a photosensitive core layer. The grating period can be as short as 100 µm in this case ($\Delta n_e < 20\times10^{-3}$). Therefore, during the fiber design step, it is compulsory to know which technique will be used to manufacture the LPG.

I have computed the LPG transmission in our fiber design. The light is supposed to be launched in the $LP_{01}$ mode of the multimode fiber and collected in the $LP_{01}$ mode at the fiber output. A strong dip in the transmission spectrum is expected where the coupling from the $LP_{01}$ to the $LP_{02}$ takes place. The goal is to obtain the broadest dip while paying attention to maximize the $LP_{02}$ dispersion.

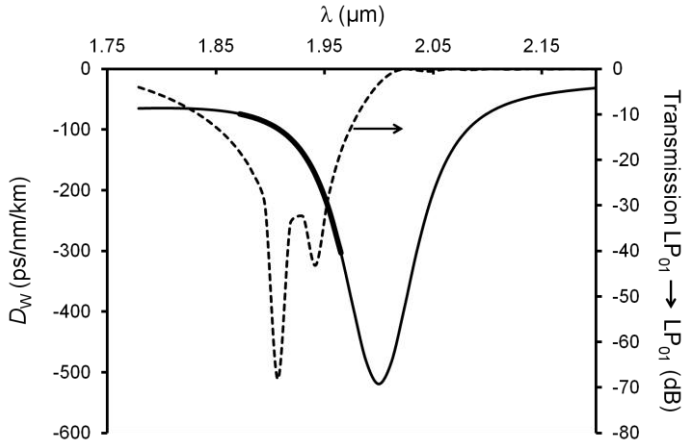


Figure III-2: Waveguide dispersion versus wavelength for the $LP_{02}$ mode of dispersive few mode fiber. Transmission of the LPG (dotted curve) versus wavelength on the right scale. $\Lambda$ = 206.9 µm.

As shown in Figure III-2, the highest computed dispersion value is –519 ps/nm/km at $\lambda_{Dmax}$ = 2 µm. The transmission bandwidth of the LPG, calculated at –20 dB, is $\Delta\lambda$ = 93 nm around $\lambda_{LPG}$ = 1.92 µm. In this spectrum, the dispersion varies from –70 to –300 ps/nm/km. Those results are the best we came to for a broadened spectrum LPG achievable by means of the UV technique ($\Lambda$ = 206.9 µm). However, the pulse propagating in the fiber should be centered on $\lambda_{Dmax}$ to avoid a too strong impact of higher order dispersion. The two peaks in the transmission of the mode converter are due to the detuning parameter being slightly positive allowing to produce two different coupling. This results in broadening the conversion spectrum.


BY-NC-ND

Since the LPG transmission is linked to the group index difference between both modes, the central wavelength of the LPG spectrum is given by the intersection of $n_{g01}(\lambda)$ and $n_{g02}(\lambda)$. Figure III-3 shows group indices of the $LP_{01}$ and $LP_{02}$ modes versus wavelength.

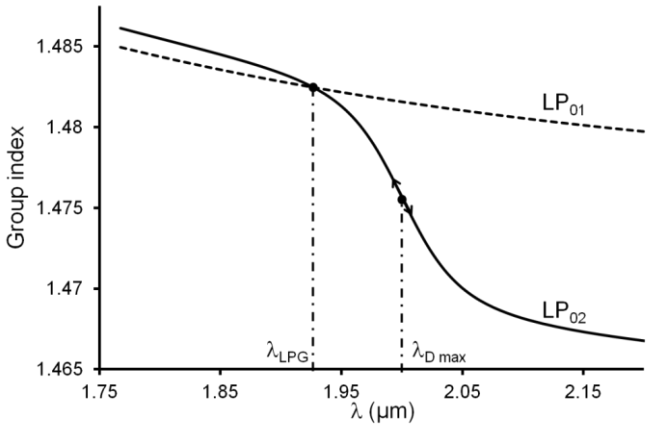


Figure III-3: Group indices of the $LP_{02}$ and $LP_{01}$ (dotted curve) modes versus wavelength.

On the other hand, the dispersion of the $LP_{02}$ mode is maximal at the wavelength of maximal slope of the group index $n_{g02}$. As we can see, the crossover point between $n_{g01}$ and $n_{g02}$ is far from the point of highest slope, hence the mismatch between the central wavelength of the LPG and $\lambda_{Dmax}$.

To tune the crossover point, one can either decrease the $LP_{01}$ group index or increase the $LP_{02}$ group index. First, the guiding properties of the $LP_{02}$ are complex and depend on all the RIP variables. Second, an increase of the effective index of the $LP_{02}$ is accompanied by the possibility to guide other higher order modes, therefore producing more MPI possibilities. Hence, I chose to decrease the $LP_{01}$ group index by lowering the core refractive index difference by $8x10^{-3}$. As shown in Figure III-4, the group indexes of both modes are decreased but the crossover point is now closer to the point of highest slope of the $LP_{02}$ group index.


BY-NC-ND

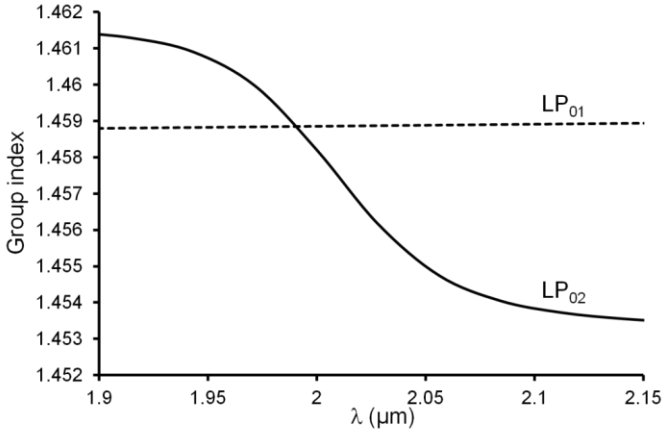


Figure III-4: Group indices of the $LP_{02}$ and $LP_{01}$ (dotted) modes versus wavelength in a dispersive few mode fiber adapted for LPG inscription.

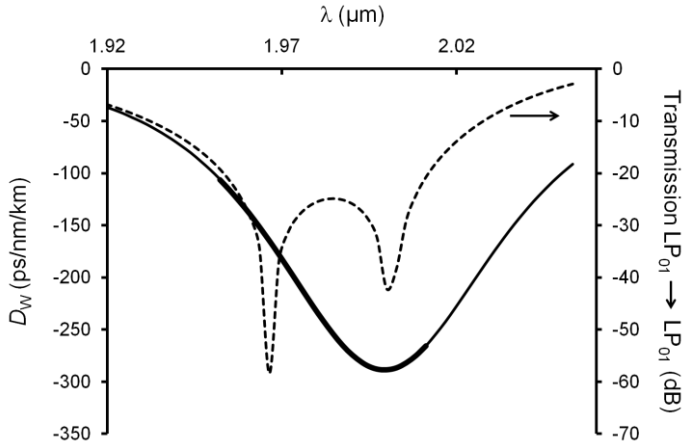


Figure III-5: Waveguide dispersion versus wavelength in a dispersive few mode fiber adapted for LPG inscription. Transmission of the LPG (dotted curve) versus wavelength on the right scale. $\Lambda$ = 413.4 µm.

Figure III-5 depicts the waveguide dispersion for a decreased $\Delta n_1$ as well as the LPG transmission for $\Lambda$ = 413.4 µm. As we can see, both curves are matching. The highest dispersion value is of –289 ps/nm/km at $\lambda_{D\ max}$ = 2 µm. The transmission bandwidth of the LPG is now equal to 60 nm around $\lambda_{LPG}$ = 2 µm with dispersion values ranging from –106 to –265 ps/nm/km. The computed $LP_{02}$ mode field area for this RIP is as high as 670 µm² at $\lambda$ = 2 µm.

A collaboration with professor H. Limberger, from the École Polytechnique Fédérale de Lausanne (EPFL) in Switzerland, was established to explore the feasibility of LPGs on our fibers. I realized a short-term scientific mission (STSM) of three weeks at EPFL to gather knowledge on the realization of LPGs and attempt to make LPGs.


BY-NC-ND

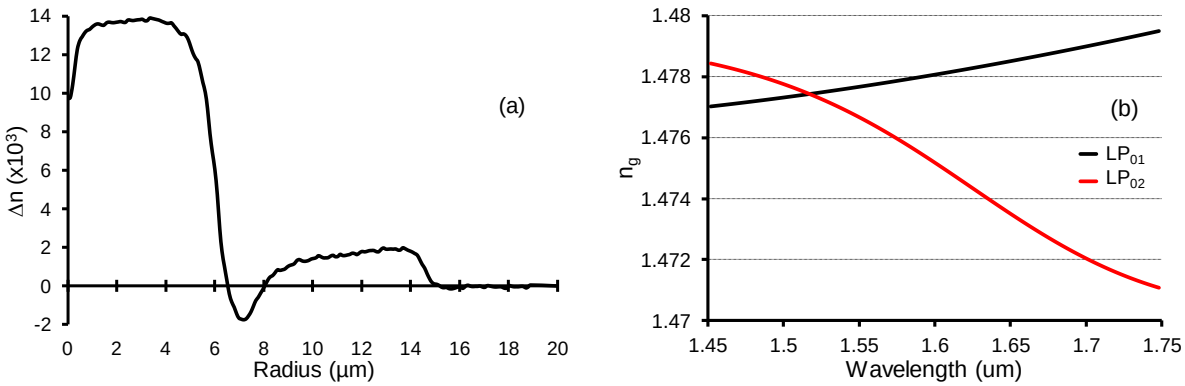


Figure III-6: (a) Measured refractive index difference of the 1.5 µm-FMF and (b) Calculated group index of the $LP_{01}$ (black) and $LP_{02}$ (red) modes.

Before the mission, a few mode fiber with a desired $LP_{01}$-$LP_{02}$ phase matching around 1.5 µm was fabricated and its refractive index profile measured (Figure III-6). Using the measured RIP and an in-house mode solver the refractive group index were calculated as a function of wavelength. Samples of this 1.5 µm-FMF were sent to EPFL in order to gather knowledge on fiber handling and photosensitivity. Fiber Bragg gratings have been fabricated using an ArF laser and a phase mask technique ($\Lambda$=1060 nm) by EPFL-PhD student Soham Basu. Figure III-7-(a) shows the evolution of FBG wavelength transmission spectra with time. The transmission spectra show oscillations due to multimode interference, MMI, (yellow and red color) and mode coupling due to the FBG. The FBG couples light from the fundamental mode to the backward propagating $LP_{01}$ and higher order modes (deep blue color). A strong $LP_{01}$-$LP_{01}$ reflection was obtained for 12 mm long FBG. Figure III-7-(b) summarizes the peak wavelength positions at the end of the irradiation. This allowed calculating the effective index values of the individual modes in order to fine tune the simulation during the STSM (Table III-1).

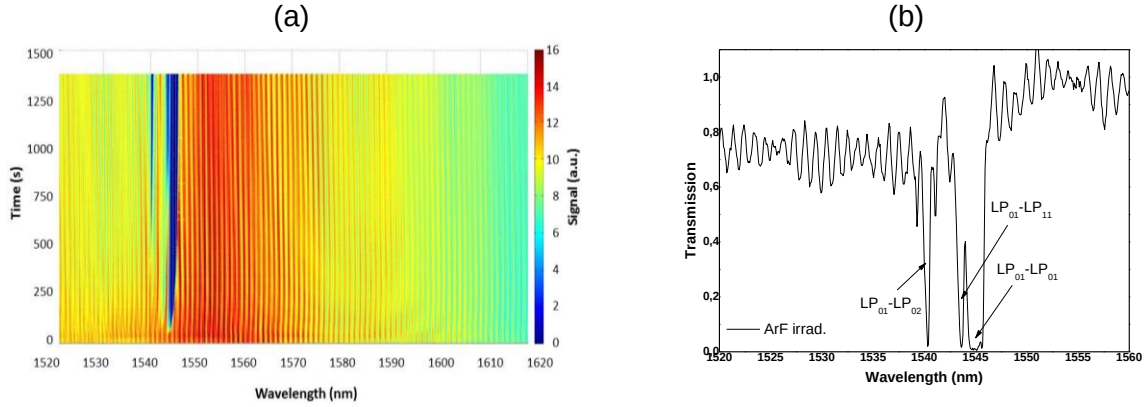


Figure III-7: (a) Evolution of FBG transmission according to time in the 1.5 µm-FMF. (b) FBG transmission spectrum at t = 1690 s)

Upon arrival intensive computations were carried out so as to match the simulated curves to the measured points. As the group index matching between the $LP_{01}$ and the $LP_{02}$ mode was


BY-NC-ND

around 1.54 µm, the calculated pitch for a 2 cm broadband LPG centered at 1.54 is 164.81 µm.

Table III-1: Summary of the calculated simulated mode effective indices at the measured wavelengths.

| Mode | Measured $n_{eff}$ | Initial simulated $n_{eff}$ | $\lvert n_{measured} - n_{initial} \rvert$ | Best simulated $n_{eff}$ | $\lvert n_{measured} - n_{best} \rvert$ |
|---|---|---|---|---|---|
| $LP_{01}$ | 1.45632 | 1.45522 | $1.12\times10^{-3}$ | 1.45660 | $0.28\times10^{-3}$ |
| $LP_{11}$ | 1.45262 | 1.45180 | $0.82\times10^{-3}$ | 1.45316 | $0.54\times10^{-3}$ |
| $LP_{02}$ | 1.44740 | 1.44650 | $0.90\times10^{-3}$ | 1.44761 | $0.21\times10^{-3}$ |

As the group indices are critical for broadband mode conversion and the application, optical low coherence reflectometry (OLCR) measurements using a commercial HP reflectometer were performed at 1560 nm. Careful observation of the OLCR spectrum depending on the excitation conditions (mechanical alignment) allowed identifying the $LP_{01}$ and $LP_{02}$ modes (Figure III-8) within the observed OLCR peaks. To identify the higher order peaks more investigation is needed. Figure III-9 shows the result of a cutback measurement for $LP_{01}$ mode. A group index (slope) of $n_g(LP_{01}) = 1.4767\pm0.0001$ was obtained.

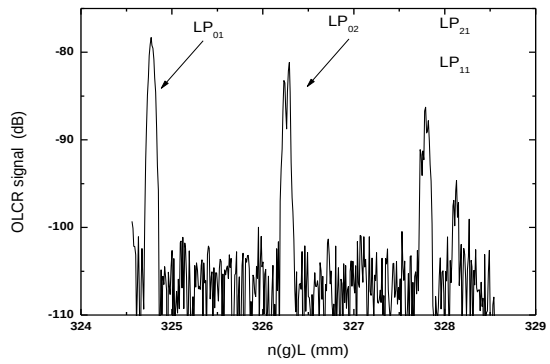


Figure III-8: OLCR spectrum of 1.55 µm-FMF end reflection measured with 1560 nm source.

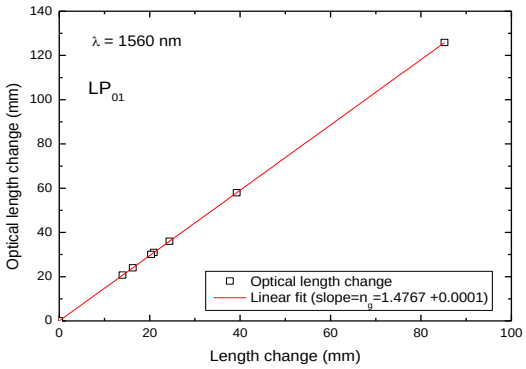


Figure III-9: Cut back measurement of $LP_{01}$ OLCR peak of 1.55 µm-FMF.

The higher order modes were heavily dependent on cleave angle and the determination of peak position with high precision was hampered by the presence of a double peak or an asymmetric peak shape. Further investigations are still ongoing so as to get the group indices of other modes especially the $LP_{02}$.

The ArF laser used for FBG fabrication was unfortunately no longer available for the STSM. The irradiation was therefore performed using the Argon laser (244 nm, Sabre FRED). A set-up was put into place and tested that allows for irradiation of the fiber using a scanning technique. The Argon beam was highly focused in order to achieve high cw intensity. The fiber, its holders, and the amplitude mask were moved repeatedly across the focused Argon


BY-NC-ND

beam over a length of 20 mm. Since the overall intensity of this laser and the fiber photosensitivity were low, a long exposure time was required so as to get some change in the measured spectra. Several irradiations were to be performed with different mask periods. From the measured difference in effective index values ($LP_{02}$-$LP_{01}$) mode converter wavelength were expected to be between 1500 and 1900 nm. Figure III-10-(a) shows a mode converter fabricated at 1697 nm with a grating pitch of around 170 µm. The MC at 1697 nm corresponds to a group index difference of 0.001 and seems to convert 40% of power from the $LP_{01}$ to the $LP_{02}$. Very good agreement with the calculated values is shown in Figure III-10-(b) for a grating pitch of 171.2 µm.

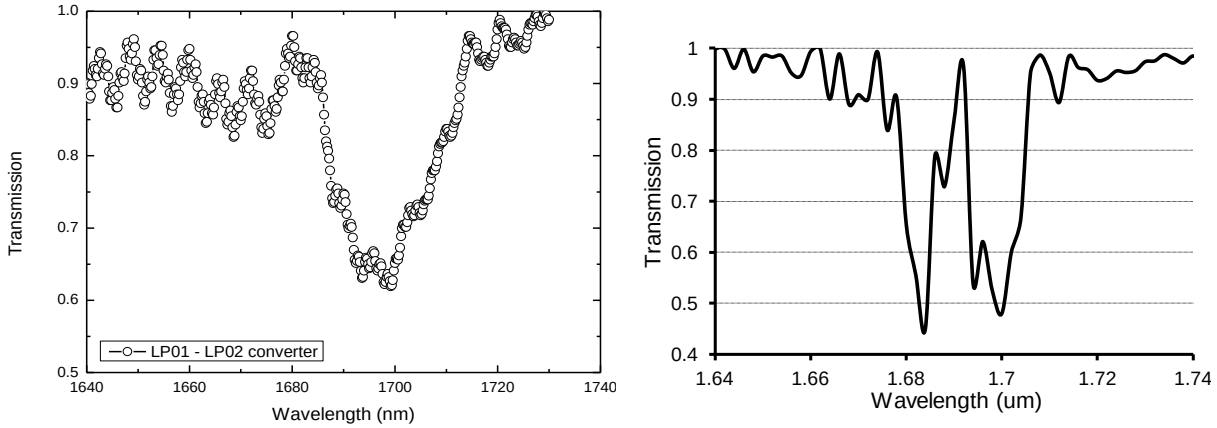


Figure III-10: (a) Measured transmission loss spectrum indicating a $LP_{01}$-$LP_{02}$ mode converter around 1.7 µm for a 2 cm LPG with around 170 µm pitch. (b) Simulated transmission loss spectrum for a 2 cm LPG with a 171.2 µm pitch

The irradiated fibers were connected to single mode fibers and excited by a Supercontinuum Source (bandwidth from 0.35 to 2.20 µm), the spectrum was recorded via an Optical Spectrum Analyzer (Ando, 0.6 – 1.75 µm). Two more LPGs were fabricated with different grating pitch but did not give any significant change on the spectrum.

Perfect match between the dispersion curve and the LPG conversion bandwidth requires fine tuning of the refractive index profile. Furthermore, once the RIP is mastered, the photosensitivity of the fiber must also be increased to allow efficient mode conversion. These technical challenges could not be reached during this thesis. Therefore, another type of all-fiber mode converter was explored.

### III.2. Modeling and realization of a dedicated mode converter

The main issue when dealing with LPG based mode converter is broadening of the transmission spectrum of the LPG while matching $\lambda_{LPG}$ and $\lambda_{Dmax}$. In this section, I present my experimental work on an *achromatic* mode converter fabricated at XLIM. This spatial mode converter tailors the electromagnetic wave by subtle changes of the longitudinal geometry of


BY-NC-ND

the ‘waveguide’. Lai and coworkers [32] proposed the hole-inflation technique as a way to modify the longitudinal geometry of photonic crystal fibers (PCF). This device, which converts the $LP_{01}$ mode to the $LP_{02}$ mode, is depicted in Figure III-11. To realize this device, the second ring of 12 holes is plugged and glued. The PCF is then pressurized by one end to raise the pressure in the unplugged holes. By heating this fiber, the pressurized holes inflate while the plugged ones collapse abruptly to form a new annular core around the original core (Figure III-11-B). Suppose the light is launched through section A. The air holes between the ring and the core in section B are large enough to avoid any coupling from the central core to the ring core. A second use of the inflation process is then done with the six holes between the core and the ring being glued. By heating and tapering (Figure III-11-C) the already processed section of fiber, the authors were able to collapse the innermost ring of holes (Figure III-11-C) and produce a large single core (Figure III-11-D). Then, they created two mode converters by cleaving the twice-processed fiber in the middle.

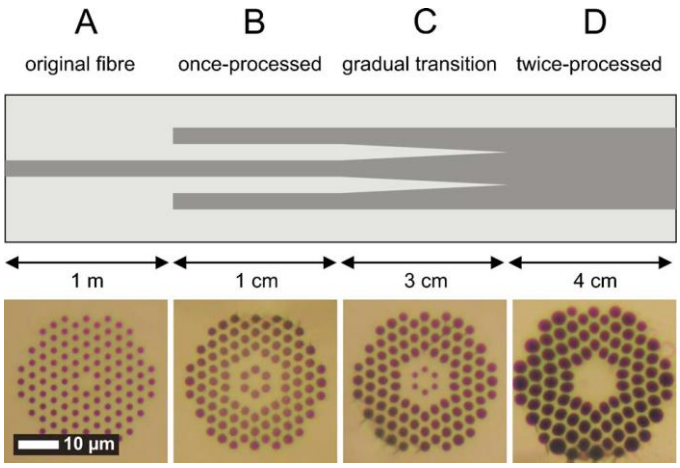


Figure III-11: Top, Schematic longitudinal cross section of the inflation-based mode converter, showing core areas in dark gray. Bottom: optical micrographs of the holey region in the cleaved fiber in each of sections A–D, on the same scale. From [32].

The light went from section A as a $LP_{01}$ since the used PCF was single-mode. In section B, the ring is bigger than the core, therefore the fundamental mode of section B is the one guided in the ring. However, since there is no coupling between the core and the ring the light is still guided in the core that is in a high-order mode of the entire structure. With the proper gradual transition in section C, the light confined in the core is slowly coupled to the fundamental ring mode. Therefore, in section D, the light is a linear combination between the ring and the core mode: the $LP_{01}$ with a hexagonal ring as shown in Figure III-12. As the transition is slow (adiabatic) this mode is still the high-order mode of section D and is the $LP_{02}$ mode (by symmetry preservation). According to the authors MPI < –15 dB can be achieved with this technique.


BY-NC-ND

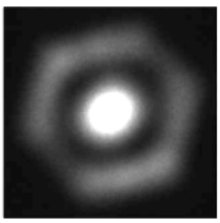

Figure III-12: Measured near field output at λ = 1 µm. From [32].

Contrary to the LPG, this device is not based on resonant coupling and is therefore not λ-dependent.

I have run numerical computations with the Comsol Multiphysics package to understand the physical behavior of this device. I have first drawn the layout of a holey structure with hexagonal symmetry. The central hole was filled with silica to simulate the signal core. The second layer of holes (12 holes) was also filled with silica as shown in inset 1 of Figure III-8. This configuration mimics that obtained in section B in Figure III-6-B. A mode calculation was carried out to obtain the lowest m-order $LP_{0m}$ modes. Numerical simulations show that two independent $LP_{01}$ modes coexist: the $LP_{01}$ ring mode (hexagonal ring shape) and the $LP_{02}$ core mode (Gaussian). We have labeled these modes according to the usual nomenclature for single-core fibres, that is to say, according to the value of their respective effective index. The mode with highest effective index is therefore labeled $LP_{01}$ and the next $LP_{0m}$ mode is labeled $LP_{02}$.

Then, I have decreased gradually the diameter of the 6 innermost holes from their nominal value to 0 (see insets 1 to 7) to model the collapse happening during the heating/tapering process. In my modeling the fiber is not tapered down. The same modes as above were considered. The variation of their respective effective index and intensity distribution are plotted in Figure III-13 versus the size of the innermost holes. If the adiabaticity criterion is fulfilled, light injected in the $m^{th}$ mode keeps traveling in this mode despite modification of the waveguide architecture and is not relabeled. For instance, if light is injected in the Gaussian-like core mode at the input end (inset 1), and if the device is adiabatic (slow collapse), light stays in the mode with this mode number. This is exemplified in Figure III-13 by the smooth variation of the effective index curves. Therefore, despite dramatic modification of the overall structure, light launched into the Gaussian like mode at the input propagates down the transition in this first high-order mode ($LP_{02}$ mode of the whole structure) and exits the structure as a mode exhibiting both a central lobe and a ring lobe. When the innermost holes are collapsed, that is to say when the fibre has a single mode, the mode resembles a ‘usual’ $LP_{02}$ mode (inset 7).


BY-NC-ND

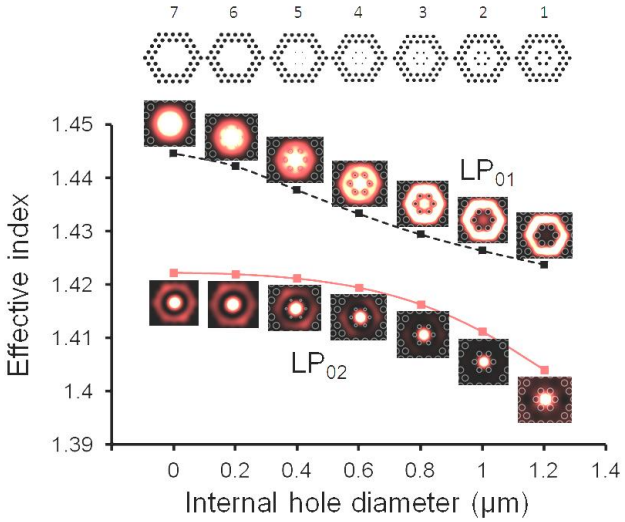


Figure III-13: Computed effective indexes of the '$LP_{01}$' ring mode and the '$LP_{02}$' of the adiabatic mode converter versus the diameter of the six internal holes. Insets represent the intensity profile for each mode. Insets 1–7 show the internal modification of the guiding structure.

This $LP_{02}$ mode is however not cylindrically symmetric. Another study was carried out to make sure that proper excitation of the $LP_{02}$ mode of our moderately multimode fiber can be achieved. The output end of the converter was scaled so that the core diameter in 7 is equal to that of the moderately multimode fiber (~16 µm). The electric field amplitudes of both the $LP_{02}$ modes match as shown in Figure III-14. The transmission coefficient from the converter $LP_{02}$ to the fiber $LP_{02}$ is $a_{02-02}$ = 90 %. Less than 1 % of the input light is launched into the fiber $LP_{01}$. The remaining power is launched into leaky modes, hence loss.

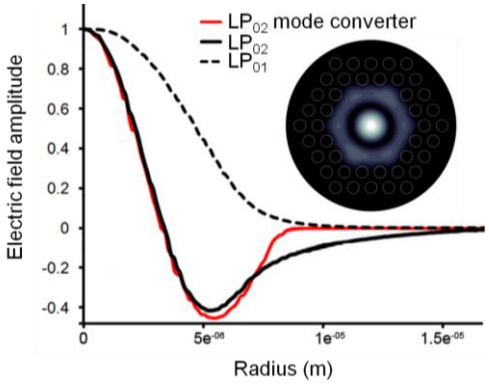


Figure III-14: Computed normalized electric field amplitudes for the $LP_{02}$ mode of the converter and the $LP_{01}$ and $LP_{02}$ modes of the few mode fiber. The inset is the computed intensity of the $LP_{02}$ mode of the converter.

It is worth noting that the electric field amplitude of the fiber $LP_{02}$ exhibits a tail (Figure III-14, thick black curve at radius equal to 10 µm) related to the ring. This tail is intrinsically related to the desired dispersion behavior. It thus cannot be avoided. Therefore, the transmission coefficient between both $LP_{02}$ modes cannot be increased over 90%.


BY-NC-ND

In the implementation of the hole-inflation technique the signal is carried by the PCF itself. In our application, the signal comes from downstream standard singlemode fibered elements, much like in the ferule technique proposed by Tim Birks, from CPPM, Bath, UK. Prof. Philippe Di Bin and Etienne Tartaret run a rather different set-up for processing holey *canes*. Manufacturing of a holey secondary preform (or cane) is depicted in Figure III-15. This holey preform is composed of capillary tubes stacked as a hexagon. The hexagon is then sleeved in a maintaining tube. In order to keep the hexagonal structure thin silica rods are stuck between the tube and the structure. The primary preform is then drawn down into several canes a few mm in diameter.

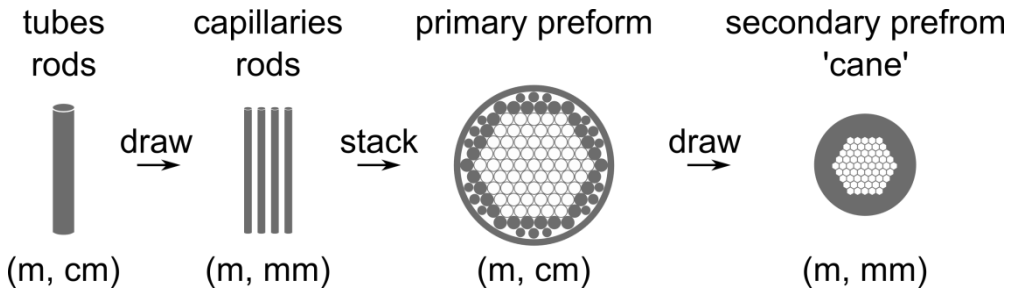


Figure III-15: Fabrication of a holey preform (or cane).

A singlemode fiber is then plugged in the central hole of the holey cane (in green in Figure III-16). The second ring of holes is plugged by the same method (in red in Figure III-16). Using the hole-inflation technique, the plugged holey cane is then heated by a burner while both ends of the cane translated ensuring slowly varying tapered transitions as depicted in Figure III-16. A cleave in the middle of the device is realized to obtain the mode converter (Figure III-16-(b)).

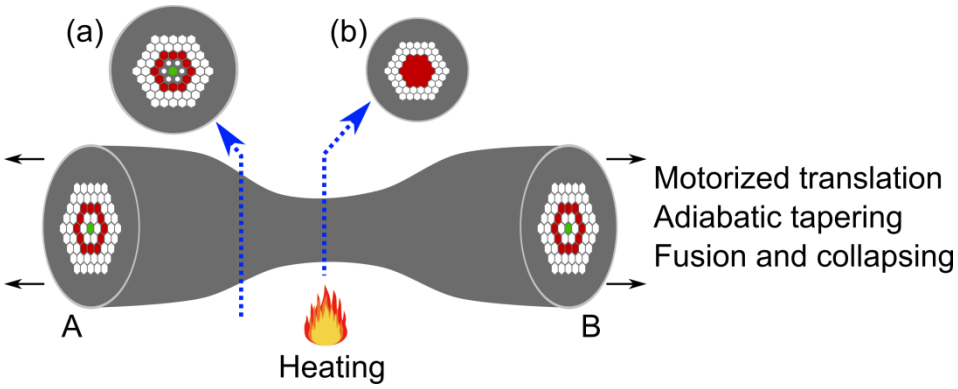


Figure III-16: Operation principle of the manufacturing of the mode converter.

We have decided to design and fabricate spatial mode converters with this set-up. Etienne Tartaret manufactured such a converter using a holey cane fabricated at XLIM. A micrograph of the cane is shown in Figure III-17. The central hole was plugged with a standard telecommunication single mode fiber SMF28. The preform was then processed and cleaved


BY-NC-ND

so that the core region is approximately 17 µm in diameter as can be seen in Figure III-17-(b) to fit the passive fiber core dimensions (Figure II-11-(a) blue).


Figure III-17: (a) Micrograph of the holey cane used to manufacture the adiabatic converter. (b) Micrograph of the output end facet of the manufactured converter.

### III.3. Passive few mode fiber excited by the $LP_{02}$ mode converter

The central fiber was then spliced to two ASE sources emitting on the erbium and thulium band respectively. The near field intensity at the output of the converter was observed by means of a thermal camera (Pyrocam). The observed near field intensities are shown in Figure III-18. As we can see, the intensity patterns are shaped by the spatial light converter and seem to be weakly wavelength dependent. In Figure III-18-(b), the camera gain was increased in order to see the whole ring resulting in the saturation of the central lobe.

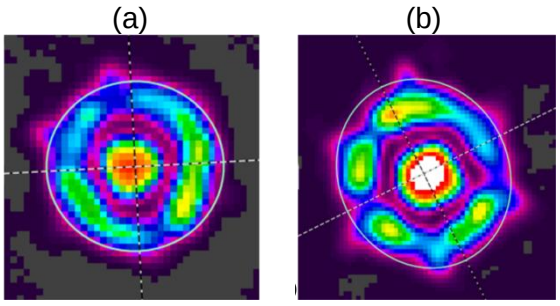


Figure III-18: Near field output of the mode converter excited by (a) an Erbium ASE source and (b) a Thulium ASE source.

A radial scan of the magnified and collimated near field was performed to gather another clue on the weak wavelength dependence. At each point of this scan, the spectrum was collected. Those measurements are summarized by Figure III-19.


BY-NC-ND

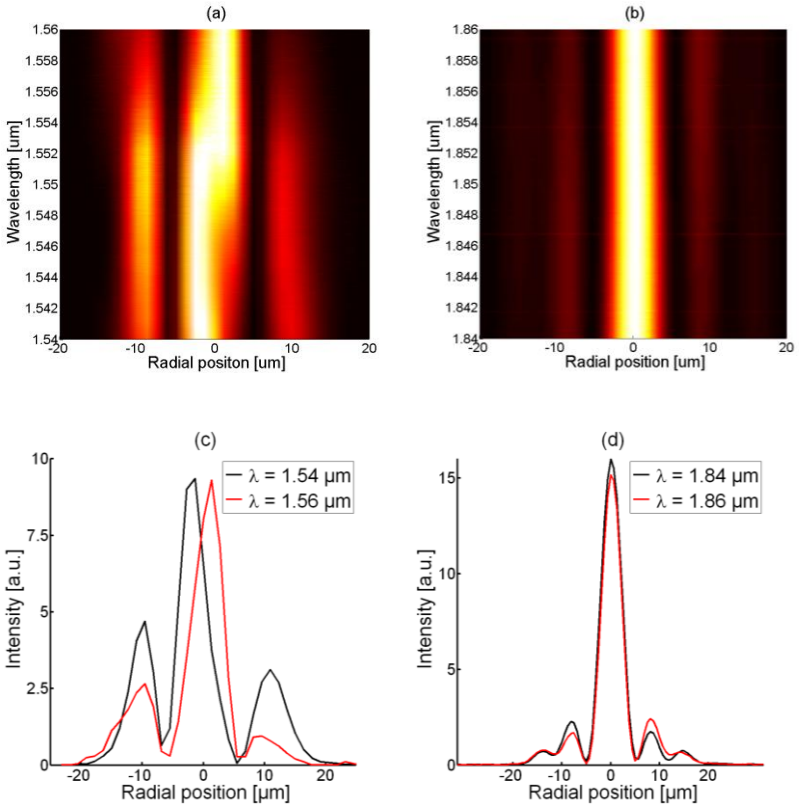


Figure III-19: Radial scan of the output near field of the mode converter excited by (a) the Erbium ASE source with 41 points of measurements and (b) the Thulium ASE source with 101 points of measurements. (c) and (d) are the respective radial traces at the beginning and the end of both bandwidths.

The spectral evolution is rather constant over tens of nanometers in both bandwidths. Furthermore, the intensity zeros are well defined in both bands. The weak wavelength dependence over 300 nm of bandwidth is thus confirmed.

Then, a 20 m long piece of passive few mode fiber (which exhibits a core size really close to that of the mode converter) was butt coupled to the mode converter end facet. The mode converter was successively excited by both ASE sources as shown schematically in Figure III-20.

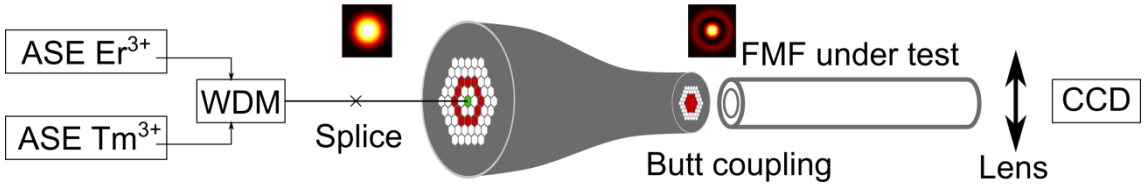


Figure III-20: Experimental set-up to evaluate selective modal excitation of the passive few mode fiber.

The field intensity at the output end of the passive few mode fiber is shown in Figure III-21. The $LP_{02}$ intensity pattern can be observed. The fiber was perturbed and coiled to check if


BY-NC-ND

the guided mode would couple to any other mode of the fiber or if the excitation was realized in both core and ring creating a virtual $LP_{02}$ mode. No intensity changes were observed, indicating weak coupling to other guided modes. The outer ring did not blink during this process. If blinking would have been observed that would have meant that the excitation was realized in both ring and core and that a 'false' $LP_{02}$ was recorded.

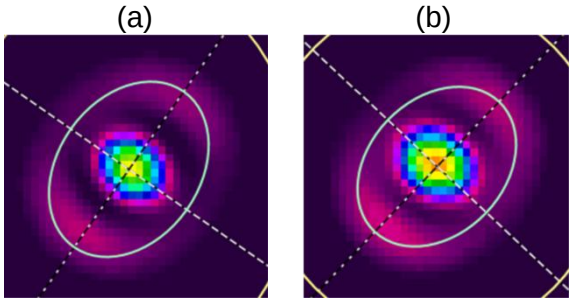


Figure III-21: Near field output of the passive few-mode fiber when excited by the mode converter with (a) the Erbium ASE source and (b) the Thulium ASE source.

### III.3.1. S² measurement on the passive few mode fiber excited by the mode converter

In order to quantitatively understand the behavior of this kind of mode converter I have developed at XLIM the spatially- and spectrally-resolved imaging technique ($S^2$) technique proposed by Nicholson [33]. Explanations of the S2 as well as a description of the various experiments carried out during my PhD are presented in Appendix 1. In the following, I will only present the experimental results obtained with the association "mode converter-passive FMF" using the Erbium and the Thulium ASE sources. Table III-2 shows the *calculated* differential group delays normalized by the fiber length ($fDGDs = \left(\left|\Delta n_g\right|/c\right)/L_{fibre}$) values for all possible interferences in both bandwidths.

Table III-2: Calculated differential group delays normalized by the fiber length in (a) the Erbium bandwidth and (b) the Thulium bandwidth. In both cases, the green cells show the fDGDs involving the $LP_{02}$ mode.

(a)

| | fDGDs (ps/m) | | | |
|---|---|---|---|---|
| | LP11 | LP21 | LP02 | LP31 |
| LP01 | 5.18 | 10.78 | 10.46 | 86.36 |
| LP11 | | 5.60 | 5.27 | 10.67 |
| LP21 | | | 0.32 | 5.08 |
| LP02 | | | | 5.40 |

(b)

| | fDGDs (ps/m) | | |
|---|---|---|---|
| | LP11 | LP21 | LP02 |
| LP01 | 6.19 | 11.52 | 4.47 |
| LP11 | | 5.33 | 1.73 |
| LP21 | | | 7.05 |

In the Erbium band, the $LP_{31}$ is guided but is close to its cut-off hence its high fDGD with the $LP_{01}$.

#### III.3.1.1. Erbium bandwidth

In this measurement, the spectral resolution of 1 pm allowed for a temporal window as wide as 10 ps/m. If the $LP_{01}$ and the $LP_{02}$ produce an interference peak, temporal aliasing may


BY-NC-ND

occur as the $LP_{02-01}$ fDGDs is superior to the time window. This interference peak would thus be seen at a delay of 0.46 ps/m. This peak may overlap with the $LP_{02-21}$ interference peak (0.32 ps/m) and produce a plateau. The recovered modes are presented in Figure III-22.

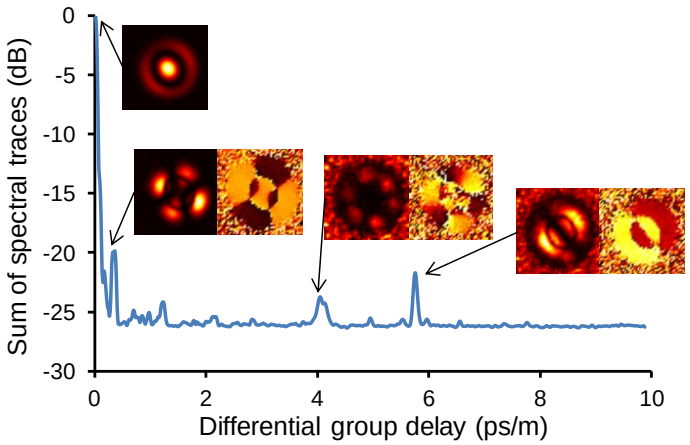


Figure III-22: $S^2$ measurement of the passive few-mode fiber excited by the mode converter on the Erbium emission bandwidth for 20 m of fiber. 3 retrieved parasitic modes: $LP_{21}$, $LP_{31}$ and $LP_{11}$.

The $LP_{01}$ was not retrieved in these measurements. This was attributed to the aliasing that will nearly superimpose both the $LP_{01}$ and $LP_{21}$ interference peaks. However a plateau is not observed hence the MPI of the $LP_{01}$ must be lower than the noise floor (~-50 dB). The measured MPIs and fDGDs are presented in Table III-3.

Table III-3: Measured differential group delays and multi-path interferences for the association between the mode converter and the passive few mode fiber around 1.55 µm.

| Measurement of | $LP_{21}$ | $LP_{31}$ | $LP_{11}$ |
|---|---|---|---|
| fDGD (ps/m) | 0.35 | 4.06 | 5.76 |
| MPI (dB) | -38 | -42 | -40 |

Very good agreement with the calculated fDGDs can be observed. Furthermore, the excitation can be said pure since 99.97% of the total power is guided by the $LP_{02}$.

### III.3.1.2. Thulium bandwidth

Using the Thulium ASE source, the only retrieved parasitic mode is the $LP_{11}$ with a slightly higher MPI of -35 dB. The high temporal noise at short delays is attributed to the water absorption peaks in this spectral window (see Appendix A.1.3). The recovered modes are presented in Figure III-23.


BY-NC-ND

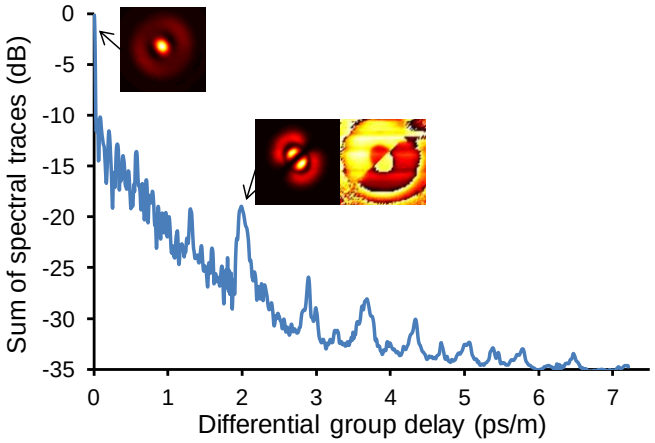


Figure III-23: $S^2$ measurement of the passive few-mode fiber excited by the mode converter within the Thulium emission bandwidth for 20 m of fiber. Only one retrieved parasitic mode: $LP_{11}$.

Both $LP_{01}$ and $LP_{21}$ were not retrieved in these measurements. This can be explained by excitation proportions being lower than the noise floor (~-50 dB). The parasitic mode measured characteristics are presented in Table III-4.

Table III-4: Measured differential group delays and multi-path interference values for the association mode converter-passive few mode fiber in the Thulium bandwidth.

| Measurement of | $LP_{11}$ |
|---|---|
| fDGD (ps/m) | 2.01 |
| MPI (dB) | -35 |

Very good agreement with the calculated fDGD is observed. Again, the excitation can be said pure since 99.97% of power is contained in the $LP_{02}$ mode.

These results constitute the first quantitative measurement of the excitation purity of a higher order mode by a device different than a LPG.

### III.4. SFSS from 1.6 to 2 um: pulsed seed source for similariton amplifier

Matching the input pulse central wavelength to $\lambda_{Dmax}$ allows reducing the impact of higher order dispersion terms. Hence, a pulsed source able to achieve the spectral matching between the pulse and the dispersion curve of the $LP_{02}$ mode is highly desirable. I have designed and fabricated a source of wavelength tunable ultrashort pulses covering the spectral region from 1.6 to 2 µm. This source is based on the self-frequency shift process of a soliton (see I.1.2) and its scheme is presented in Figure III-24. The pulse train is generated by an all-fiber self-starting mode-lock laser generating 1 ps pulses with an average power of 0.7 mW at a wavelength of 1.56 µm with a FWHM of 4 nm. The pulses are stretched to avoid any nonlinear amplification. At the output of the pre-amplifier, the pulses are a few ps in duration with an average power of 10 mW. Then the pulses are directly amplified in a large mode area Er-doped fiber amplifier. Finally a piece of singlemode passive fiber is used to


BY-NC-ND

shift the central wavelength further in the infrared. A high-pass filter with a cut-off wavelength of 1.6 µm is placed after the output of the singlemode fiber.

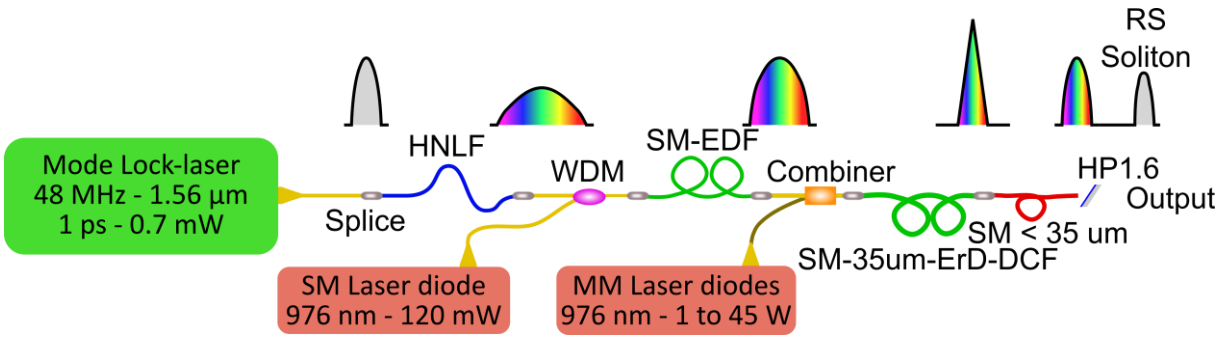


Figure III-24: Setup scheme for the self-frequency shifted soliton source. Upper line is the temporal shape along the setup with colors representing the pulse chirp (grey stands for chirp equal to 0). Standard singlemode (SM) fibers are represented in yellow, multimode (MM) fibers in dark yellow. HNLF highly nonlinear fiber, WDM Wavelength Division Multiplexer, SM-EDF single mode erbium doped fiber, ErD-DCF Erbium doped double-clad fiber, HP1.6 high-pass filter with 1.6 µm cut-off wavelength.

By fine-tuning the high power pump diodes of the last stage of amplification, the energy stored in the pulses is varied thus producing ejected solitons that will experience different wavelength shift according to the input pump power. This dependence of the pulse central wavelength on the pump power is shown in Figure III-25.

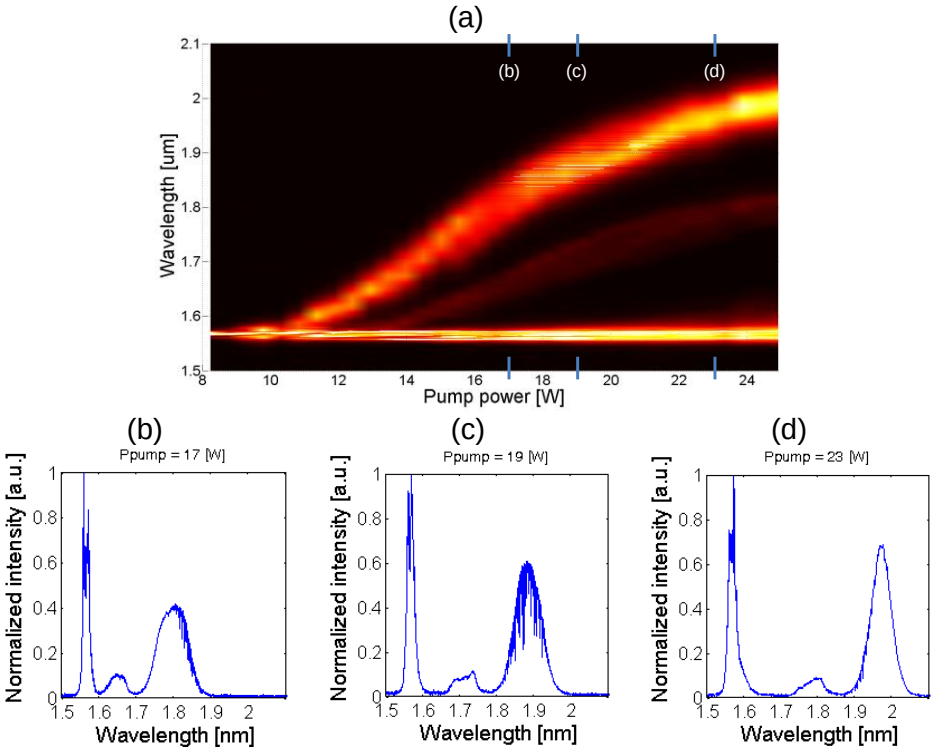


Figure III-25: (a) Measured evolution of the spectral profile at the output of the Raman frequency-shifting fiber versus the pump power delivered to the last stage amplifier. (b-d) Measured spectra at various pump power of 17, 19 and 23 W respectively showing tunability from 1.8 to 1.99 µm.


BY-NC-ND

The central wavelength of the output pulse can be swept from 1.8 to 1.99 µm to match $\lambda_{Dmax}$ of the realized fibers. The pulse presents a spectral bandwidth ranging from 36 to 44 nm FWHM with an average power ranging from 250 mW to 300 mW. As the output, the filtered pulse is a fundamental soliton. It is Fourier-limited as shown in the auto-correlation trace in Figure III-26 and presents a duration of 100 fs FWHM. These parameters will be used as feeding parameters for the GNLSE solving software.

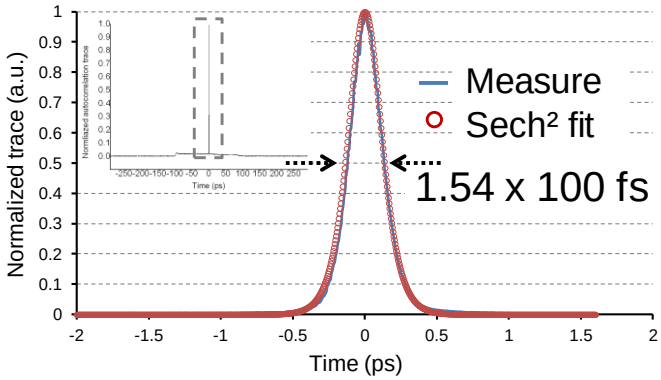


Figure III-26: Autocorrelation trace (blue) and hyperbolic secant squared fit (red circles) of the output pulse centered at 1.9 µm wavelength. Inset is the full autocorrelation trace showing the measuring range pedestal spanning from -100 to 100 ps.

### III.5. Dispersion measurement

The dispersion of the $LP_{02}$ mode has been measured using the setup in Figure III-27.

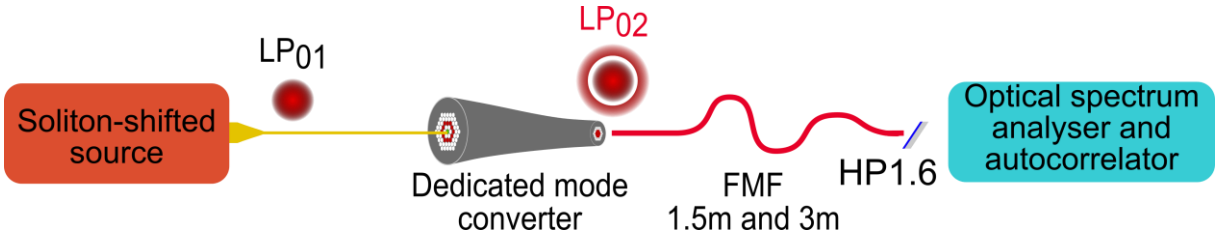


Figure III-27: Dispersion measurement setup using the SFSS source centered at 1.95 µm, the dedicated mode converter and the passive few mode fiber

The soliton-shifted source was centered at 1.95 µm. The source output was fusion spliced to the dedicated mode converter input. The mode converter output was successively butt-coupled to 3 m and 1.5 m of the passive FMF. Measuring the auto-correlation trace and the pulse spectrum at the output of the few-mode fiber in both configurations allowed evaluating the dispersion around 1.95 µm. Figure III-28 shows the measurements of the auto-correlation trace and spectrum in both cases. During the experiment, the spectral width changed by 5 nm and the central wavelength drifted from 1.949 to 1.942 µm.


BY-NC-ND

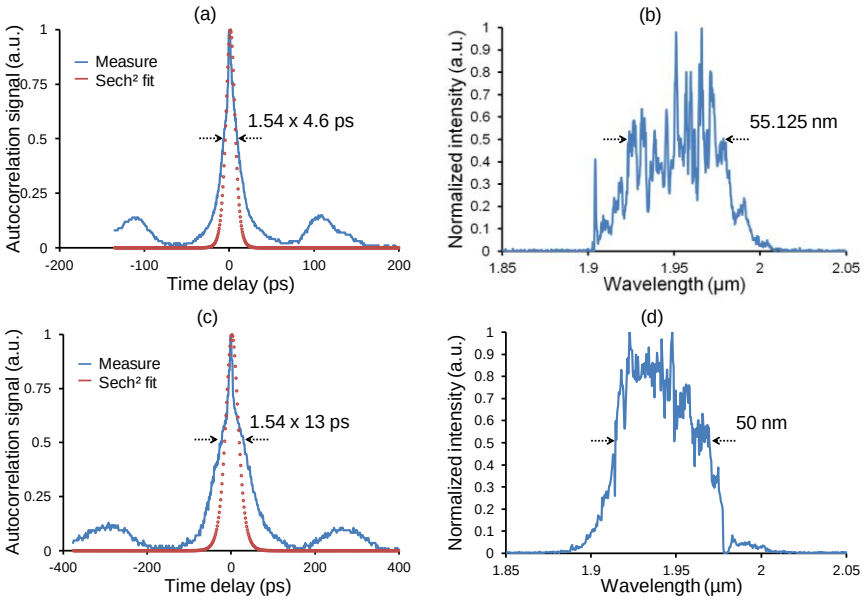


Figure III-28: Dispersion measurement with the SSFS source at 1.95 µm. (a) Autocorrelation trace and (b) output spectrum for 1.5 m of passive few mode fiber excited by the mode converter. (c) Autocorrelation trace and (d) out spectrum for 3 m.

The following equation was used to evaluate the dispersion:

$$D = \frac{\Delta t}{L\Delta\lambda} \qquad \text{(III.2)}$$

with L the fiber length ($1.5\text{x}10^{-3}$ km), $\Delta t$ the FWHM duration difference (8.4 ps) and $\Delta\lambda$ the FWHM spectral bandwidth (ranging from 50 to 55 nm). The evaluated dispersion is comprised between -102 and -112 ps/(nm.km) in very good agreement with the modeled value of -108 ps/(nm.km). Side lobes can be observed in both autocorrelation traces. However, contrary to what was observed by Morin [34] (in French), these ripples are not consistent with other guided modes at this wavelength. This potentially comes from the SSFS initial pulse centered at 1.56 µm which propagates in a totally different dispersion regime.

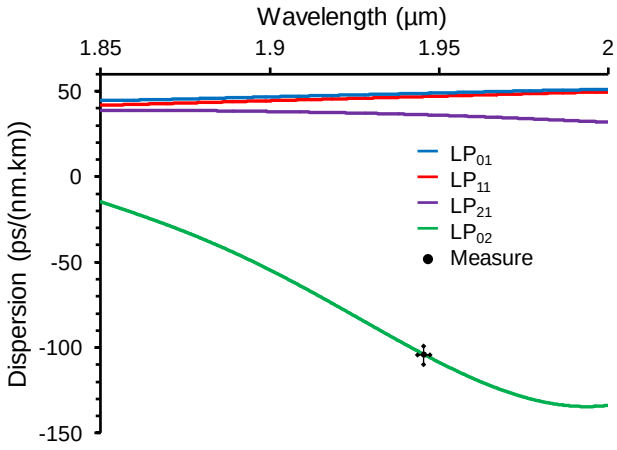


Figure III-29: Dispersion measurement compared to expected value.


BY-NC-ND

As can be seen in Figure III-29, the only mode presenting normal dispersion is the $LP_{02}$. Through this measurement, I confirmed a very good excitation by the mode converter of the $LP_{02}$ mode in a pulsed regime and the viability of this type of fiber to produce normal dispersion in the short-wavelength infrared (SWIR). Moreover, this constitutes the first measurement, to my knowledge, of the dispersion of a higher mode using an excitation device other than a LPG.

### III.6. Conclusion

In this chapter I have shown that the $LP_{02}$ mode of a dispersion-tailored FMF can be excited at two remote wavelengths of 1.55 and 2 µm by means of an adiabatic mode converter. This device was designed and realized at XLIM using the hole-inflation technique. The adiabatic mode converter allowed proper excitation of the $LP_{02}$ with close to 100% efficiency in the passive few-mode fiber as shown by the spectrally- and spatially-resolved imaging technique. A tunable self-frequency shifted soliton source providing 100 fs pulses with 250 mW average power from 1.6 to 2 µm was realized. The mode converter and the tunable source were used to measure the chromatic dispersion of the $LP_{02}$ mode around 1.95 µm. To my knowledge, this is the first report on a fiber providing high normal dispersion (-108 ps/nm/km) at long wavelengths, far above the telecom window. Unfortunately, the output facet of the mode converter was deteriorated during experiments. A new cleave was performed without success preventing any satisfactory coupling into the few-mode fiber. Very recently, Dr. Correa from CREOL provided us with photonic lanterns [35]–[38] that are being tested. Nonetheless, these first experimental results show that, despite discrepancy between the target RIP and the measured one, large normal dispersion and large effective area can be achieved in the same fiber mode in the Tm-ion emission band near 2 µm. Armed with these preliminary results I now describe the design, fabrication and characterization of an active few-mode fiber.


BY-NC-ND

It is now clear that dispersion-tailored FMF can be designed, fabricated and properly excited to yield high normal dispersion in the SWIR. In this chapter I evaluate the potential hold by the FMF design in the context of parabolic amplification via numerical simulations. First I describe the numerical procedure used. Then I highlight the results that can be obtained taking the limitations of the MCVD process into account. Finally, I describe a very first manufactured active fiber and comment on its ability to be used as a parabolic amplifier.

## IV.1. Singlemode TDFA

Up to now, the TDFA was not modeled in the lab. Key parameters such as the relaxation lifetime and the cross-sections have been measured elsewhere and have been made publicly available. However various datasets are available [39]–[42] which correspond to various glass matrices. In order to feed the software with proper TDF parameters a singlemode alumino-germano-silicate Tm-doped fiber was fabricated and characterized at IRCICA/PhLAM. The glass matrix of this fiber will be used in further developments of active few mode fiber. The refractive index profile of this fiber and its radial distribution of Thulium ions are plotted in Figure VI-1(a).

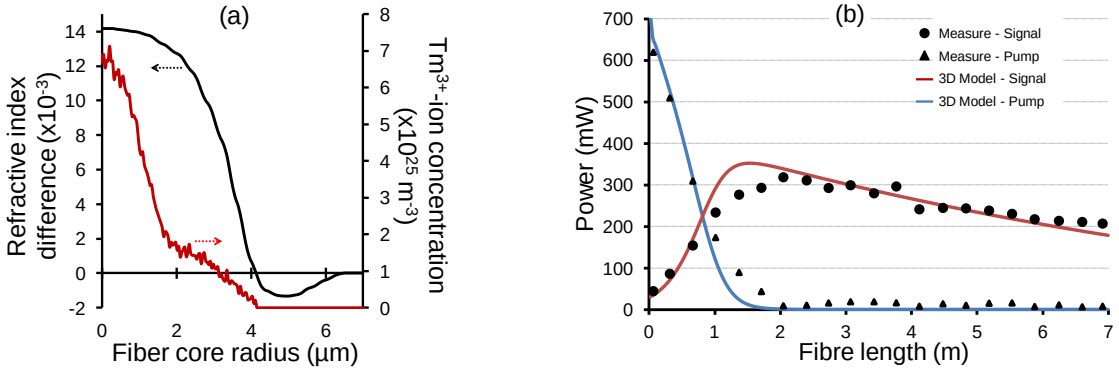


Figure IV-1: (a) Measured refractive index difference (black) and Thulium ion concentration (red) of the singlemode Tm-doped fiber. (b) Characterization in amplification regime ($P_{signal\_in}$ = 30 mW - $\lambda_{signal}$ = 1950 nm, $P_{pump\_in}$ = 670 mW - $\lambda_{pump}$ = 1560 nm)

It is worth noting that the radial distribution of Thulium ions is rather different than that of other dopants ($Al_2O_3$ and $Ge_2O_3$), which contribute to the RIP. The maximal Thulium ion concentration is $7\times10^{25}$ $m^{-3}$. The distribution decreases in the core and vanishes at the core/cladding interface. The Tm ion distribution cannot be approximated by a step distribution and must be taken into account in the calculation as it drastically reduces the overlap integral between the light and the active ions.


BY-NC-ND

TDFAs can be resonantly pumped in the telecom window at ~1.56 µm by EDFAs. High-power TDFAs can also be pumped at 793 nm. The latter is useful providing the cross-relaxation mechanism is efficient. This mechanism is efficient in highly-doped TDF, which is not the case in the research fibers developed during this PhD. Therefore, the pump wavelength lies around 1.56 µm and the pump radiation is supplied by a high-power cw singlemode EDFA.

I have built a singlemode EDFA supplying 1.2 W of power at 1560 nm. This source is based on a ring oscillator composed of two WDM (the first one protects the diode), a 70/30 output (30) coupler, 3 m of singlemode Er-doped fiber and an isolator. The ring laser is pumped by a singlemode laser diode emitting 140 mW at 976 nm. This seed is then amplified in an Er/Yb-doped DCF pumped using a 2+1:1 combiner by two multimode laser diodes each emitting 6.5 W at 976 nm. The output of the amplifier was connected to an isolator to avoid any back reflection. The schematic is presented in Figure IV-2.

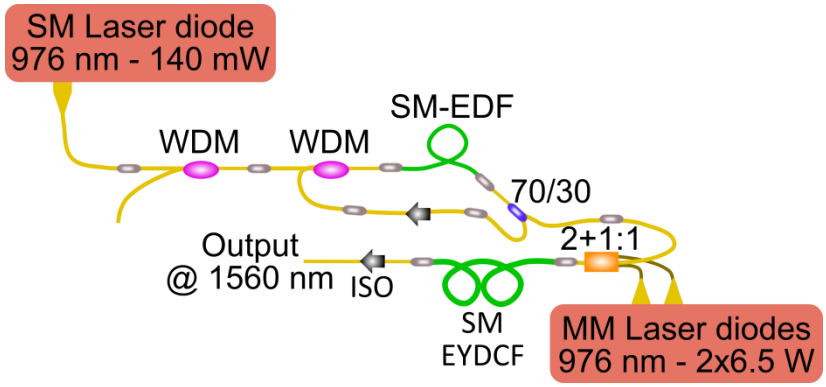


Figure IV-2: Schematic of the high-power CW singlemode EDFA. ISO Isolator, 70/30 ring output coupler with 30 being the output arm, 2+1:1 pump combiner and EYDCF Erbium/Ytterbium doped double-clad fiber.

I have then characterized the fiber in amplification regime. The fiber was core-pumped at 1560 nm. I have measured the output signal power as a function of the fiber length and plotted the results in Figure VI-1(b) (black dots and triangles). The gain is low due to the small amount of Tm-ions interacting with the light.

Then the TDFA was modeled taking into account the actual RIP and Tm-ion distribution. Several datasets known from the literature for TDF, including the relaxation lifetime and emission and absorption cross-sections, were implemented successively in the software. Good quantitative agreement was obtained for a dataset provided in [41]. The fluorescence lifetime is 560 µs. Emission and absorption cross-sections are plotted in Figure IV-3. These values will be used in further developments of active few-mode fiber.


BY-NC-ND

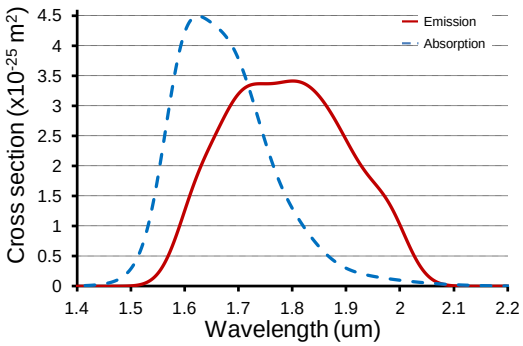


Figure IV-3: $Tm^{3+}$ absorption (dashed-blue) and emission (red) cross-sections leading to a good quantitative agreement between the measured and calculated evolutions of the pump and signal powers along the fabricated fiber.

## IV.2. Numerical procedure

The goal of this paragraph is to evaluate the potential hold by a Tm-doped version of the fiber design shown in Figure IV-3 for parabolic amplification of ultrashort pulses in the vicinity of 2 µm. The RIP and the expected Tm-ion concentration are schematically depicted in Figure IV-3.

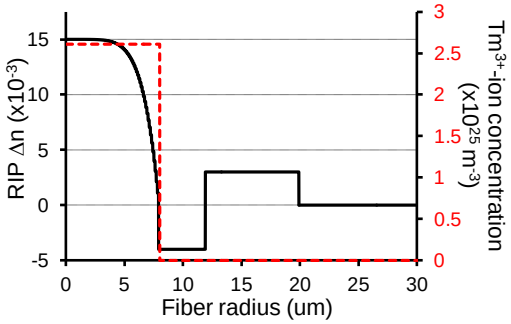


Figure IV-4: Refractive index profile (black) of a $Tm^{3+}$-doped few-mode fiber. $\alpha = 6$, $\Delta n_1 = 15\times10^{-3}$, $r_1 = 8$ µm, $\Delta n_2 = -4\times10^{-3}$, $\Delta r_2 = 4$ µm, $\Delta n_3 = 3\times10^{-3}$, $\Delta r_3 = 8$ µm. The active ions distribution is flat in the core (red dotted). The $Tm^{3+}$ concentration is equal to $2.6\text{x}10^{25}$ $m^{-3}$ (mean value of the SMF $Tm^{3+}$ concentration).

Numerical modeling of a core-pumped few-mode TDFA has been carried out using an in-house developed software according to the process depicted in Figure IV-3.


BY-NC-ND

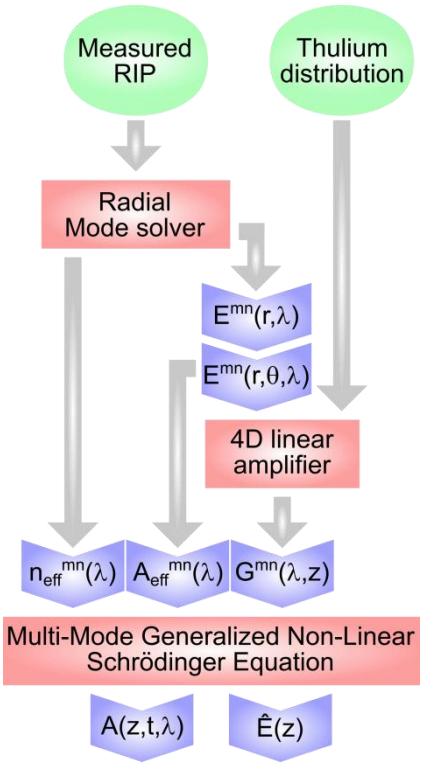


Figure IV-5: Numerical process based on three different in-house programs (red rectangles) fed by the measured RIP and Thulium distribution (green circles) to obtain several sets of data (blue arrows) resulting in the pulse spectral, temporal and energetic evolution along its amplification in the core-pumped few-mode TDFA.

First, a mode solver for cylindrically symmetric fibers is fed by the refractive index profile of the amplifying fiber shown in Figure IV-2. The mode solver gives every $LP_{mn}$ mode (superscripts *m* and *n* correspond to azimuthal and radial indices) characterized by the following parameters:

- effective index variations $n_{eff}^{mn}(\lambda)$,
- effective modal area variations $A_{eff}^{mn}(\lambda)$
- radial electrical field distribution variations $E^{mn}(r,\lambda)$.

Then, $E^{mn}(r,\lambda)$ is symmetrized according to the azimuthal number *m* to give $E^{mn}(r,\theta,\lambda)$.

At the pump wavelength (C-band), the $LP_{01}$, $LP_{11}$, $LP_{21}$, $LP_{02}$ and $LP_{31}$ modes are guided (Figure IV-4). The $LP_{31}$ cut-off wavelength is around 1.7 µm. In the Tm emission band, the fiber will propagate the four lowest-order LP modes.

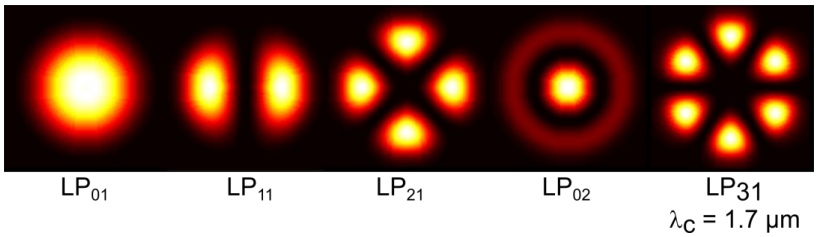


Figure IV-6: Guided LP modes of the few-mode TDF at $\lambda$ = 1.56 µm.


BY-NC-ND

Then, the rate equations for the multimode amplifier are solved by taking into account the transverse distributions of electrical field for each co-propagated mode [43]. This software gives the $LP_{02}$ gain versus wavelength and longitudinal position $G_{02}(\lambda,z)$. This model takes gain saturation into account. $G_{02}(\lambda,z)$ is of paramount importance to properly model gain narrowing in ultrashort pulse amplifiers. It also accounts for the influence of ASE (carried by any guided mode) and the effect of the shape of the pump in the core-pumping regime.

Finally, the GNLSE with gain (Eq I.11) is solved for in order to determine the spectral and temporal properties of a pulse envelope carried by the $LP_{02}$ mode in this amplifier. The nonlinear program is fed by $n_{eff}^{02}(\lambda)$, $G_{02}(\lambda,z)$ and $A_{eff}^{02}(\lambda)$.

### IV.2.1. Multimode amplification in continuous wave regime

A schematic of the numerical procedure for modeling multimode amplification in continuous wave regime is shown in Figure II-14.

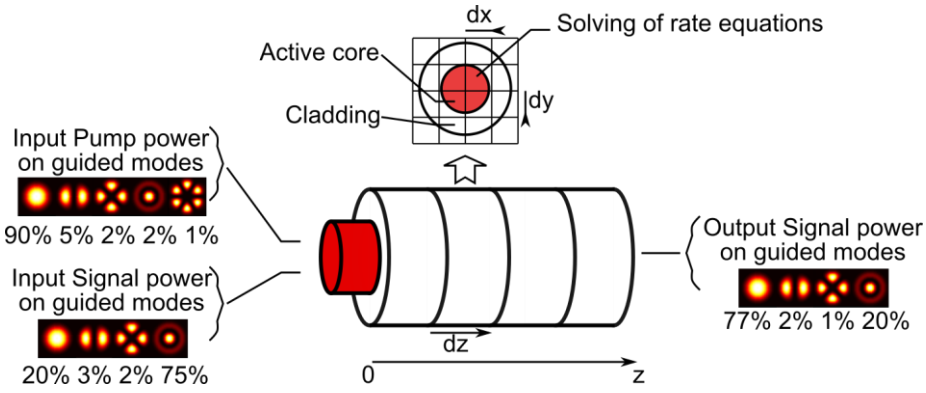


Figure IV-7: Modeling of a core-pumped multimode amplifier. The input powers of the pump and signal are split among the guided modes at the respective wavelengths. The output data give the new modal weights (and therefore modal power) at each wavelength.

The population inversion $N_2(x,y,z) - N_1(x,y,z)$ is discretized in all three spatial coordinates with steps dx, dy and dz. The signal and pump input radiations are linear combinations of $\alpha^{mn}(\lambda)\, E^{mn}(x,y)$ where $\alpha^{mn}(\lambda)$ is the modal weight at wavelength $\lambda$ at the input of the fiber. The rate equations are solved in each elementary section (dx×dy) in order to evaluate the longitudinal variation of population inversion $N_2(x,y,z) - N_1(x,y,z)$ and $\alpha^{mn}(z)$ [43]. The signal and pump *output* radiations are then linear combinations of $\alpha^{mn}(L)\, E^{mn}(x,y)$. Amplified spontaneous emission (ASE) is evenly distributed among the guided modes.

#### IV.2.1.1. Dependence of the gain on the pump wavelength

First I considered a singlemoded $LP_{02}$ amplifier using the Optimal RIP for the modeled fiber, both the pump and signal are carried by the $LP_{02}$ mode. This core-pumped TDFA was modeled to obtain the spectral and spatial dependence of the gain ($G = P(z,\lambda)/P(0,\lambda)$) for


BY-NC-ND

various pump wavelengths. The amplifier was seeded by a signal centered at $\lambda_{Dmax}$ (1.907 µm) with a 40 nm bandwidth FWHM carrying 250 mW of power. The signal spectrum is given a hyperbolic secant squared shape to model the high-repetition rate (48 MHz) pulsed signal. The pump wavelength was varied from 1.535 µm, 1.550 µm, and 1.560 µm (C-band EDFA) while the pump power was kept at 6 W. The spectral and spatial variation of the gain is shown in Figure IV-6 for the three pump wavelengths. The contour line at value equal to one represents transparency. The area below this line represents absorption.

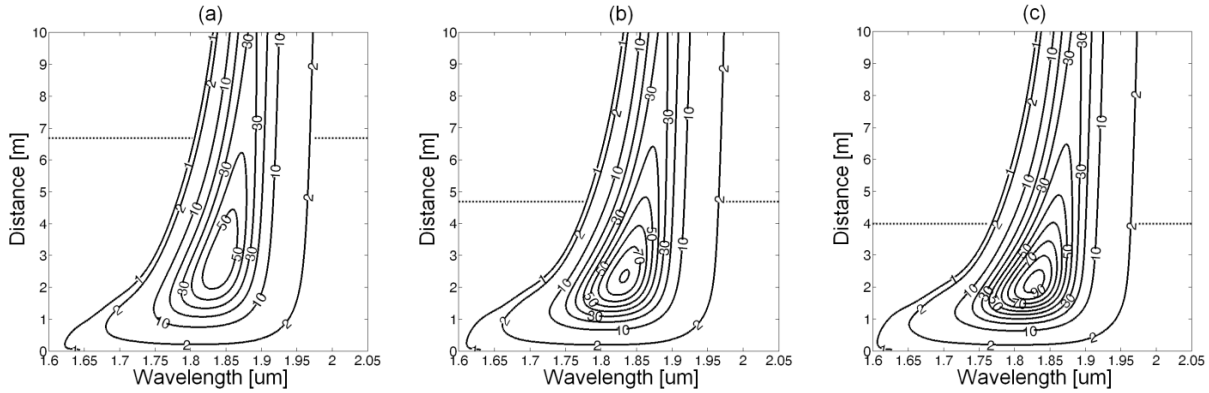


Figure IV-8: Results from modeling of $LP_{02}$ cw TDFA. Spectral and spatial evolution of the gain for (a) $\lambda_p$ = 1.535 µm, (b) 1.55 µm, (c) 1.56 µm. Optimal lengths for maximal output power are (a) 6.66 m, (b) 4.75 m, (c) 3.97 m, shown by dotted lines.

The TDFA must provide a gain bandwidth wide enough to amplify at least 50 nm of pulse bandwidth so as to avoid pulse deterioration by *e.g.* gain filtering. Moreover the optimal length ($L_{opt}$, where the amplified signal is maximized) must be as long as possible to take advantage of the dispersion provided by the dispersion-tailored fiber. In the three cases, the output signal power at $L_{opt}$ is around 4.7 W. At short wavelengths, TDFA gain is lower than one while at longer wavelength $L_{opt}$ is too short to take advantage from the dispersion. Along the amplification, at the pump wavelength of 1.535 µm, the pulse spectral FWHM increases from 40 nm to 48 nm in the first two meters. Afterwards, the FWHM shrinks down to 37 nm at $L_{opt}$ and to 33 nm after 10 m of propagation as shown in Figure IV-9.

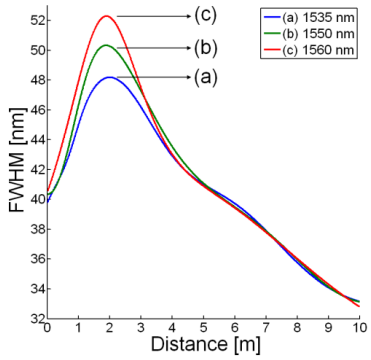


Figure IV-9: Spectral FWHM evolution along the amplification in the TDFA according to the pump wavelength (a-blue) 1535 nm, (b-green) 1550 nm and (c-red) 1560 nm.


BY-NC-ND

During amplification, any abrupt saturation process might impact the propagation of a similariton. In case (a), the distributed gain over 10 m of fiber indicates a smooth progression towards saturation and is therefore the best compromise between achievable gain, bandwidth and saturation. Furthermore, the wider the spectral breathing along the amplification the more the pulse can be distorted by the gain. These results indicate that the pump wavelength should be around 1535 nm.

#### IV.2.1.2. Spatial evolution of the $LP_{02}$ weight along amplification

Second, the study of the amount of power carried by the $LP_{02}$ mode along amplification has been carried out according to the pump and signal modal content. For a matter of clarity, I will present the results on configurations involving only two modes, the $LP_{01}$ and $LP_{02}$, since they are more likely to couple to each other. Three cases for the pump modal content are studied and for each, four cases for the signal modal content will be presented as summarized in table IV-1. As in the first study, the amplifier was seeded by a signal centered at $\lambda_{Dmax}$ (1.907 µm) with a 40 nm bandwidth FWHM carrying 250 mW of power. The pump wavelength is 1535 nm with 6 W of power.

Table IV-1: Studied numerical cases for the evolution of the amount of power carried by the $LP_{02}$ mode along the amplifier.

| | | | | | | | |
|---|---|---|---|---|---|---|---|
| Pump | Case name | A | | B | | C | |
| | LP | 01 | 02 | 01 | 02 | 01 | 02 |
| | Weight (%) | 100 | 0 | 50 | 50 | 0 | 100 |

| | | | | | | | | | |
|---|---|---|---|---|---|---|---|---|---|
| Signal | Case n° | 1 | | 2 | | 3 | | 4 | |
| | LP | 01 | 02 | 01 | 02 | 01 | 02 | 01 | 02 |
| | Weight (%) | 10 | 90 | 5 | 95 | 1 | 99 | 0.1 | 99.9 |

The pump radiation will be either in the fundamental mode (Case A) or in the $LP_{02}$ mode (Case C) or equally distributed among the two modes (Case B). A controlled input excitation of the few-mode fiber $LP_{02}$ mode with some residual power launched in the fundamental mode at the signal wavelength is assumed (Cases n°1 to 4). Feeding the multimode linear amplifier software with the parameters in table IV-1 gives the curves shown in Figure IV-10.


BY-NC-ND

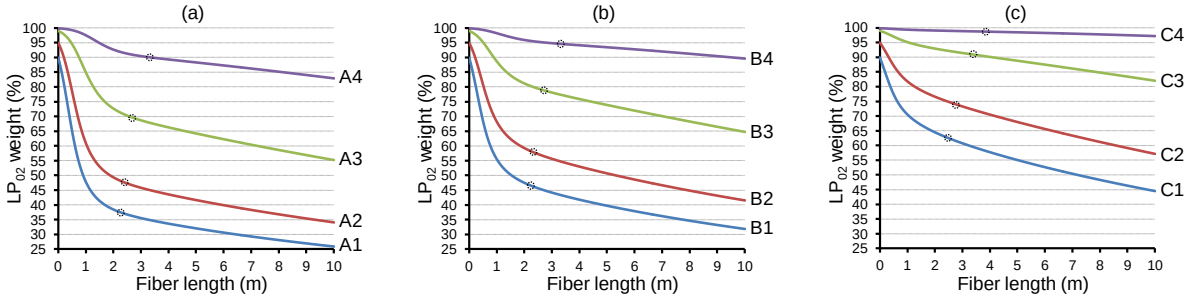


Figure IV-10: $LP_{02}$ weight evolution along amplification in (a) case A, (b) case B and (c) case C. Black dotted circles are the respective $L_{opt}$ where the amount of power in the $LP_{02}$ mode is the highest.

From these results, two observations can be made. First, in every case, the weight of the $LP_{02}$ mode is decreasing along the amplifier. However, the strongest modal degradation is observed in case A (Figure IV-10-(a)). This can be explained by the fact that the Tm ions are pumped in the fundamental mode only, thus the inverted population maps the $LP_{01}$ mode intensity. Therefore, the modal content at the amplifier output changes dramatically due to an enhanced amplification of the portion of the signal launched in the $LP_{01}$ mode. Second, $L_{opt}$ is decreased from 6.66 m to less than 4 m when compared to what was expected by the gain spectral and spatial dependences explained in the previous point. This can be explained by the modal competition occurring during amplification. $L_{opt}$ is calculated when the amount of power in the $LP_{02}$ is the highest however along the amplification the weight of the $LP_{02}$ mode decreases thus the balance between those two parameters produce a lower $L_{opt}$. It can be noticed that the higher the $LP_{02}$ weight the longer $L_{opt}$ (Case C1-4 in Figure IV-10-(c)). The different power carried by the $LP_{02}$ at each $L_{opt}$ is summarized in table IV-2. The highest power is obtained for the case C4 where the pump is fully carried by the $LP_{02}$ and the input signal has the highest weight of $LP_{02}$.

Table IV-2: Calculated $L_{opt}$ and power carried by the $LP_{02}$ mode at $L_{opt}$ in every case combination.

| Case | A | | | | B | | | | C | | | |
|---|---|---|---|---|---|---|---|---|---|---|---|---|
| N° | 1 | 2 | 3 | 4 | 1 | 2 | 3 | 4 | 1 | 2 | 3 | 4 |
| $L_{opt}$ (m) | 2.11 | 2.25 | 2.62 | 3.26 | 2.28 | 2.42 | 2.82 | 3.43 | 2.58 | 2.78 | 3.27 | **3.8** |
| $P_{02}(L_{opt})$ (W) | 1.7 | 2.2 | 3.2 | 4.1 | 2.13 | 2.64 | 3.6 | 4.4 | 2.88 | 3.44 | 4.26 | **4.64** |

The amount of power that is not carried by the $LP_{02}$ mode will be useless in the similariton amplifier. It is thus compulsory to have the highest weight of $LP_{02}$ at both pump and signal wavelengths to take full advantage of both the dispersion and the amplifier.


BY-NC-ND

### IV.2.1.3. Enhanced design

A way to release the constraint on the modal conversion at the pump wavelength has been explored. This solution relies on the delocalization of the fundamental from the active media by modifying the RIP. Using the knowledge gathered in Chapter II, the enhanced profile presented in the Figure IV-11-(a) has been tuned so that its $LP_{02}$ will produce roughly the same amount of dispersion as the optimal profile but centered at $\lambda_{Dmax}$ = 1.85 µm (Figure IV-11-(b)). At this wavelength, the $LP_{02}$ mode presents an effective area of 440 µm². The opto-geometrical parameters are summarized in table IV-3.

Table IV-3: Opto-geometrical parameters of the enhanced few-mode fiber and $LP_{02}$ characteristics at $\lambda_{Dmax}$.

| | Enhanced RIP | |
|---|---|---|
| | Δn | Δ*r* |
| Depressed active core | $8\times10^{-3}$ | 3 |
| Core | $16\times10^{-3}$ | 9 |
| Trench | $-4\times10^{-3}$ | 4 |
| Ring | $3\times10^{-3}$ | 9.5 |
| $D_{02}(\lambda_{Dmax})$ [ps/(nm.km)] | -350 | |
| $A_{eff}^{02}(\lambda_{Dmax})$ [µm²] | 440 | |
| FOM [fs] | 136 | |

The $\lambda_{Dmax}$ was shorten allowing a balanced amplification of the pulse spectral components. This is due to two phenomena opposing each other. On one hand, as the mode is generating dispersion, its overlap integral with the gain media is decreasing (Figure IV-11-(c)) hence unbalancing the spectral amplification in favor of the short wavelengths. On the other hand, the longer the amplifier, the higher the gain at longer wavelengths. When taking into account both phenomena, we can expect a balanced amplification of the pulse at the fiber output.

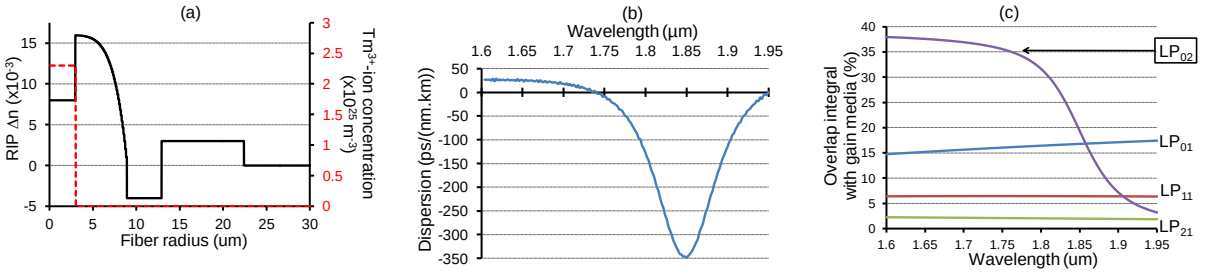


Figure IV-11: (a) Enhanced RIP and $Tm^{3+}$ modeled distribution. (b) Calculated dispersion curve of the $LP_{02}$ mode in this design. (c) Overlap integral for each mode.

The same study concerning the spatial evolution of the $LP_{02}$ weight along the amplifier has been carried out giving the curves in Figure IV-12. As can be seen, not only is the signal


BY-NC-ND

input weight preserved but it also increases along the amplifier in every cases. Furthermore, $L_{opt}$ has been increased by factors spanning from 5 to 10 due to the low overlap integrals.

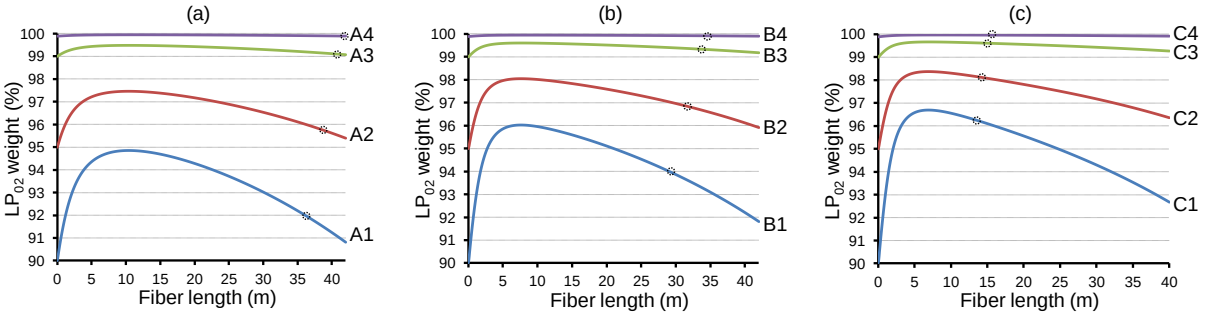


Figure IV-12: $LP_{02}$ weight evolution along amplification in the Enhanced design few-mode fiber in (a) case A, (b) case B and (c) case C. Black dotted circles are the respective $L_{opt}$ where the amount of power in the $LP_{02}$ mode is the highest.

The different power carried by the $LP_{02}$ at each $L_{opt}$ is summarized in table IV-4. The output powers are in most cases comparable to the best achieved power when using the optimal RIP. These observations show that the constraint on the mode conversion at the pump wavelength has been removed. More precisely, it has been somewhat transferred to a constraint on $L_{opt}$ as in any singlemode amplifier.

Table IV-4: Calculated $L_{opt}$ and power carried by the $LP_{02}$ mode at $L_{opt}$ in the Enhanced design in every case combination at the pump wavelength of 1.535 µm. (bold figures underline output power higher than the highest possible power using the optimal design).

| Case | A | | | | B | | | | C | | | |
|---|---|---|---|---|---|---|---|---|---|---|---|---|
| N° | 1 | 2 | 3 | 4 | 1 | 2 | 3 | 4 | 1 | 2 | 3 | 4 |
| $L_{opt}$ (m) | 35.4 | 37.9 | 40.9 | 41.9 | 29.1 | 31.3 | **33.6** | **34.3** | **14.3** | **14.7** | **15** | **15.1** |
| $P_{02}(L_{opt})$ (W) | 4.18 | 4.37 | 4.53 | 4.56 | 4.36 | 4.5 | **4.63** | **4.65** | **4.77** | **4.87** | **4.94** | **4.96** |

By increasing the pump wavelength we can decrease $L_{opt}$. The pump wavelength was set to 1.59 µm to underline the strength of the link between the pump wavelength and $L_{opt}$. The achieved weights are slightly increased by 1 point in every case. The $L_{opt}$ were decreased by a factor of 3 as shown in table IV-5 while the output power was slightly increased to reach a limit around 5.13 W.

Table IV-5: Calculated $L_{opt}$ and power carried by the $LP_{02}$ mode at $L_{opt}$ in the enhanced design in every case combination at the pump wavelength of 1.590 µm.

| Case | A | | | | B | | | | C | | | |
|---|---|---|---|---|---|---|---|---|---|---|---|---|
| N° | 1 | 2 | 3 | 4 | 1 | 2 | 3 | 4 | 1 | 2 | 3 | 4 |
| $L_{opt}$ (m) | 12.7 | 13 | 13.4 | 13.4 | 11.2 | 11.5 | 11.8 | 11.8 | 5.8 | 5.9 | 5.9 | 6 |
| $P_{02}(L_{opt})$ (W) | 4.98 | 5.09 | 5.17 | 5.19 | 4.93 | 5.03 | 5.1 | 5.12 | 4.98 | 5.06 | 5.13 | 5.14 |


BY-NC-ND

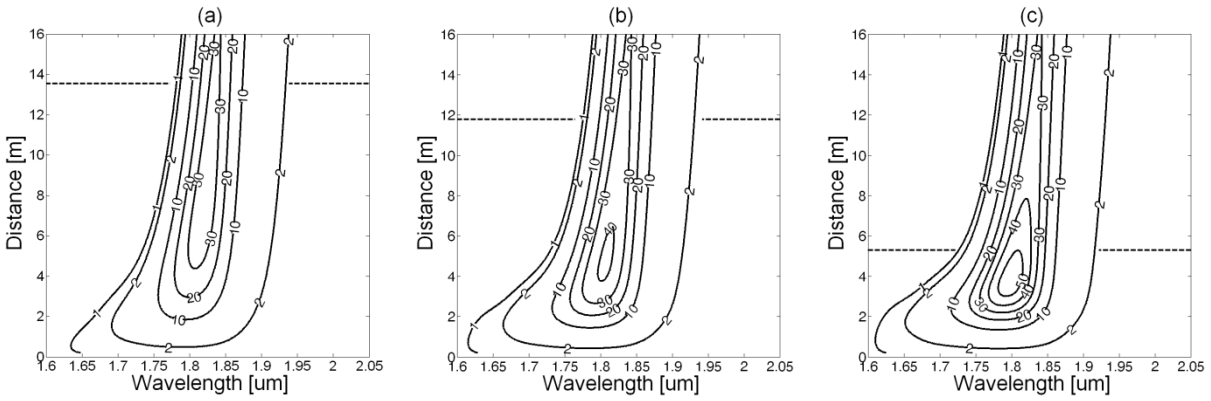


Figure IV-13: Results from modeling of $LP_{02}$ cw TDFA in the enhanced few-mode fiber design. Spectral and spatial evolution of the gain for case (a) A4 (b) B4 (c) C4. Optimal lengths for maximal output power are shown by dotted lines.

From these results, we can say that the enhanced design transferred the pump modal conversion constraint to a kind of $L_{opt}$ constraint. As can be seen in table IV-5, converting the pump mode to the $LP_{02}$ will decrease the required amplifier length by 2 all other things being equal. This decrease in length will produce strong variations of the gain in short pieces of fiber. As we wanted to avoid these fluctuations it would even be better to carry the pump on the fundamental mode of this fiber as confirmed by the spectral gain evolutions along the fiber presented in Figure IV-13. A preform of this fiber is currently being realized at IRCICA/PhLAM.

### IV.2.2. Nonlinear modeling

Here will be presented the different calculations realized on the optimal profile. I have focused my study on the evolution of the spectral and temporal properties of a pulse carried only by the $LP_{02}$ mode during its propagation in a dispersion-tailored active few-mode fiber. Equation I.31

$$\hat{E} = \frac{c}{8gn_2}\frac{D^2(\Delta\lambda)^3 A_{eff}}{\lambda}$$

gives the maximum extractable energy before wavebreaking. Applying this equation to the computed optimal RIP with the same parameters as in I.2.3.1 ($g$ = 1.9 Np/m and $\Delta\lambda_{full}$ = 105 nm) we obtain the results summarized in table IV-6.

IV-6: Calculated maximum extractable energy of an amplified similariton in the optimal design.

| Fiber | Optimal |
|---|---|
| $\lambda_{Dmax}$ (µm) | 1.908 |
| $\lvert D_{max}\rvert$ (ps/(nm.km)) | -380 |
| $A_{eff}$ (µm²) | 353 |
| **$\hat{E}$ (µJ)** | **27** |


BY-NC-ND

The energy of a similariton propagating in the $LP_{02}$ mode in this fiber can reach 27 µJ before wavebreaking. This equation, relies on several approximations: the gain is constant along the fiber; the dispersion and effective area are not wavelength-dependent. In order to understand whether this equation is valid in more realistic conditions, I have modeled the propagation of an ultrashort pulse in the optimal fiber design by solving the GNLSE. I have assumed a constant gain of 1.9 Np/m, a constant effective area of 353 µm² while wavelength dependence of *D* was included. Two seed pulses were tested, an unrealistic 1 ps pulse and a realistic 100 fs to study the equation I.31 and the influence of effective area and gain dependence to wavelength.

#### IV.2.2.1. Constant effective modal area and gain

This study is focused on the evaluation of similariton wavebreaking. A similariton wavebreaking can be identified in two ways. First, the temporal or spectral shape is no more a parabola hence the pulse is no more a similariton. Second, the chirp has to be linear, if the chirp is no more linear we cannot define the pulse as a similariton.

##### IV.2.2.1.1. Unrealistic 1 ps pulse

The seed pulse in this numerical simulation is an unchirped soliton with the characteristics reported in table IV-7.

Table IV-7: Input pulse temporal and spectral characteristics.

| Pulse characteristic | Value |
|---|---|
| $\Delta t$ (ps) | 1 |
| $\Delta\lambda$ (nm) | 4 |
| $\hat{E}$ (nJ) | 10 |
| Chirp | 0 |

Its temporal and spectral shapes are represented in Figure IV-14. This pulse was deliberately set to unrealistic values since the purpose of this simulation was to quickly reach wavebreaking to compare the model and what was expected by Equation I.31.


BY-NC-ND

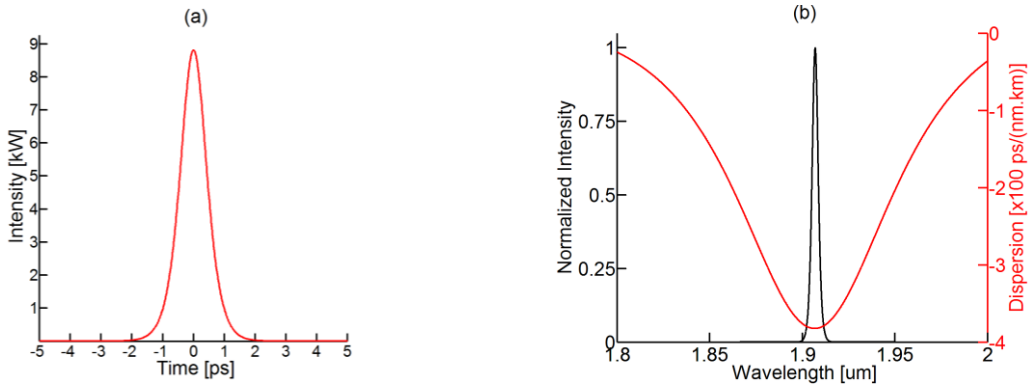


Figure IV-14: Numerical simulations of the input (a) temporal ($\Delta t$ = 1 ps) and (b-black) spectral profile ($\Delta\lambda$ = 4 nm) of the pulse carrying 10 nJ of energy seeding the core-doped optimal few-mode fiber with constant gain (1.9 Np/m), assuming constant effective area of 353 µm² and wavelength dependent dispersion (b-red).

The temporal and spectral shapes at the fiber output are presented in Figure IV-15-(a-b). The soliton launched into the fiber amplifier shapes, in the temporal domain, towards a parabola after few centimeters of propagation in the fiber. Then, the parabolic temporal shape is maintained and enlarged along amplification as can be expected from a similariton. Figure IV-15-(a) shows the strong temporal breathing along the amplifier from 1 ps to 40 ps. In the same time, the pulse spectrum also broadens due to nonlinear Kerr effect. The pulse energy grows exponentially from 10 nJ to 20 µJ without wavebreaking.

The pulse temporal profile is slightly distorted, though, due to higher-order dispersion parameters ($\beta_3$, $\beta_4$,…) included in the simulation.

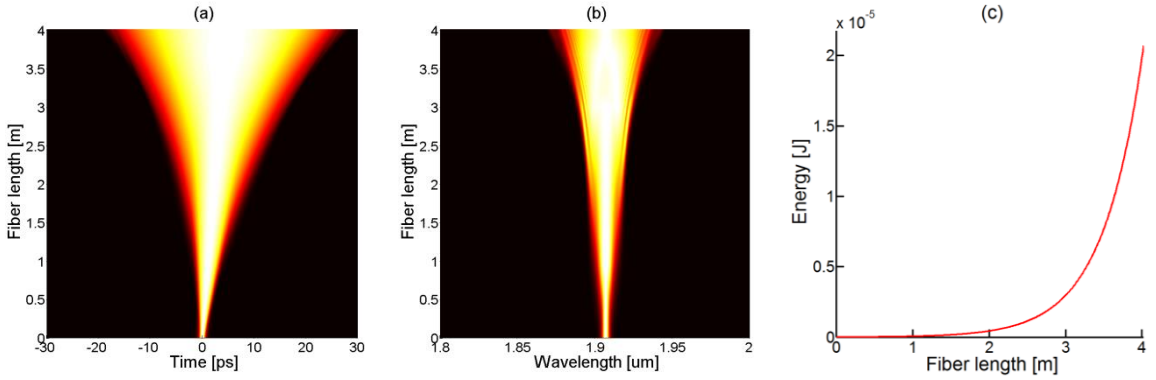


Figure IV-15: Numerical simulations showing the longitudinal evolution of (a) temporal and (b) spectral profiles of a pulse propagating in the optimal few-mode fiber, assuming constant effective area of 353 µm² and wavelength dependent dispersion. The profiles are normalized to 1 at each position. (c) Evolution of the pulse energy along the amplifier (constant gain of 1.9 Np/m).

The wavebreaking can be identified by looking at the pulse envelope and the chirp. On one hand, if the envelope has located features, then wavebreaking is starting as shown by Figure IV-16-(b-c).


BY-NC-ND

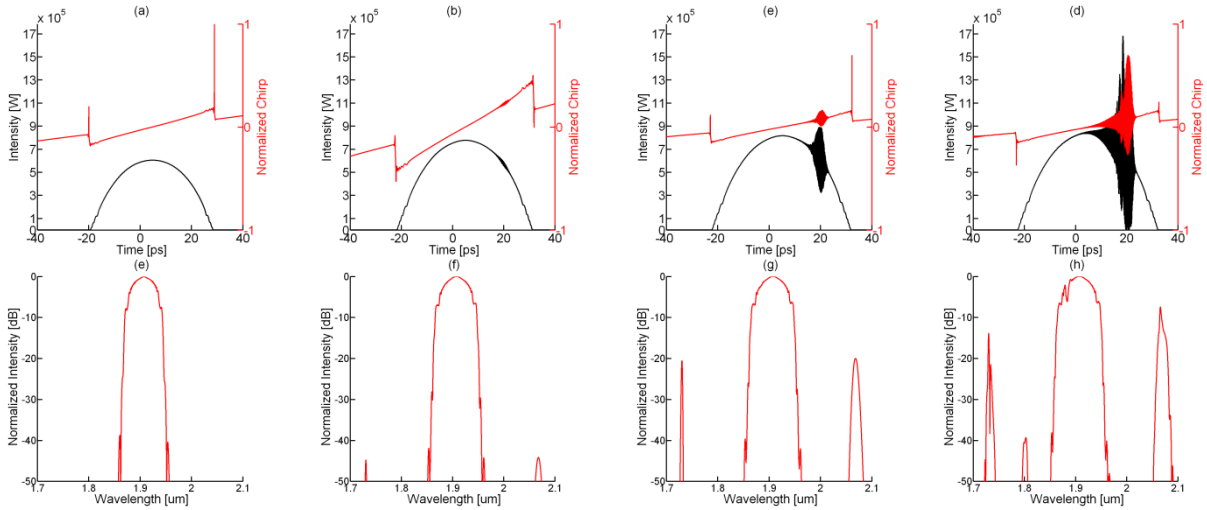


Figure IV-16: Numerical simulations showing evolution of the temporal (first row) and normalized spectral (second row) profiles of the pulse for various fiber lengths: (a-e) 4 m, (b-f) 4.19 m, (c-g) 4.23 m and (d-e) 4.25m.

In Figure IV-16-(b), wavebreaking is starting, the pulse temporal shape starts to locally oscillate due to nonlinear process occurring at both zeros of the modeled dispersion of the $LP_{02}$ mode (1.73 µm and 2.08 µm). After few centimeters, the pulse will present stronger oscillations as shown in Figure IV-16-(c-d) due to the constant gain. At longer pieces of fiber, every wavelength will experience the constant gain and nonlinear effects will occur and overwhelm the pulse. Nonetheless, the energy comprised in the pulses presented in the first row of Figure IV-14 is above 20 µJ as shown in Table IV-8.

Table IV-8: Numerical simulations showing the achieved energy in the active optimal few-mode fiber with constant gain of 1.9 Np/m, constant $A_{eff}$ of 353 µm² and wavelength dependent dispersion.

| Figure label | Fiber length (m) | Energy (µJ) |
|---|---|---|
| a | 4 | 20.2 |
| b | 4.19 | 28.7 |
| c | 4.23 | 30.7 |
| d | 4.25 | 32.15 |

The wavelengths at the zeros of dispersion exceed the -100 dB threshold at 23.8 µJ of energy at the fiber length of 4.1 m. Afterwards, temporal features are noticeable. The generation of wavelength on or near the zeros of dispersion is the limitation to the energy scaling of a similariton.

A lossless double-passing compression line was modeled to check the compressibility of the amplified pulse. This compression line only compensates for the two first orders of dispersion ($\beta_1$ and $\beta_2$). This line is composed of two transmission gratings with a resolution of 560 lines/mm (PCG-560-2000-933 from Ibsen photonics) placed at the Littrow angle (34°). For a distance between the two gratings of 5.37 cm, the pulse in Figure IV-16-(a) is compressed down to 180 fs FWHM (Figure IV-17). The compressed pulse presents


BY-NC-ND

unbalanced side bands due to higher order dispersion not compensated for by the gratings. This results in having 55% of the pulse energy contained in the 180 fs central peak allowing reaching 61.8 MW peak power.

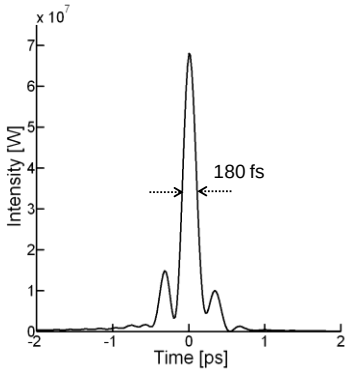


Figure IV-17: Numerical simulations showing the compression of the output pulse (z = 4 m) down to 180 fs FWHMI by a grating compressor in the case of the unrealistic input pulse (10 nJ, 1 ps, 4 nm).

These results are presented to underline the possibilities of similariton amplifiers when considering a constant distributed gain (1.9 Np/m) and effective area (353 µm²). The pulse, carried by a purely excited highly dispersive $LP_{02}$, can be recompressed to 180 fs pulse duration with over 10 µJ energy in its central lobe.

#### IV.2.2.1.2. Realistic 100 fs pulse

However, with an input pulse with a broader spectrum as is the case for fs pulse, SPM could be triggered closer to the dispersion zeros limiting the stored energy before wavebreaking. Notwithstanding, the spectral power density is drastically lowered compared to ps pulses, thus the SPM process that will impose the wavebreaking should be reached later in the fiber when compared to the unrealistic ps pulse. To underline this assumption a realistic fs pulse was used all other things being equal. Table IV-9 summarizes the realistic pulse characteristics.

Table IV-9: Input pulse temporal and spectral realistic characteristics taken from the SFSS source.

| Pulse characteristic | Value |
|---|---|
| $\Delta t$ (fs) | 100 |
| $\Delta\lambda$ (nm) | 40.5 |
| $\hat{E}$ (nJ) | 5.2 |
| Rep_rate (MHz) | 48 |
| Average power (mW) | 250 |
| Chirp | 0 |

Figure IV-18 shows the temporal and spectral profile of this pulse; plus the dispersion and the effective area evolutions according to wavelength.


BY-NC-ND

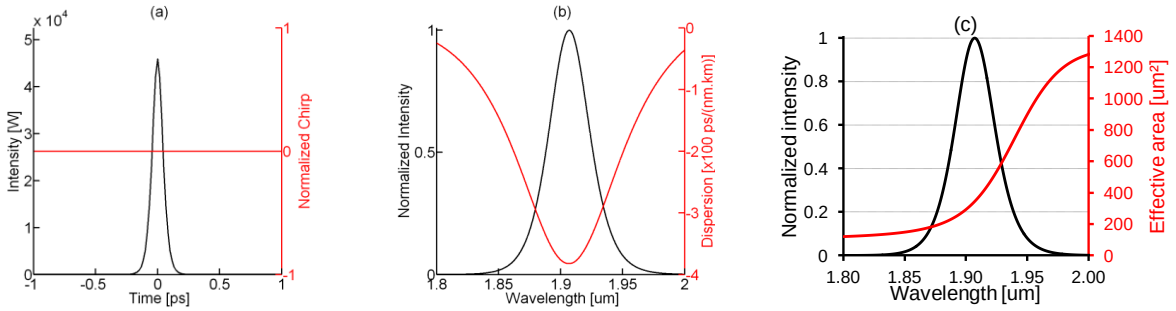


Figure IV-18: (a) temporal and (b-c) spectral profiles of the realistic seed pulse. In (b) the red curve shows the dispersion. In (c) the red curve shows the effective area.

Figure IV-19 presents the normalized temporal and spectral shape evolution in the fiber amplifier when seeded with the realistic pulse and the energy evolution along the amplifier. It can be noticed that after 4 m of fiber, the spectral shapes is widening due to SPM process. The effect on the pulse temporal and spectral shapes is in no way comparable to the unrealistic pulse behavior. Nevertheless, the temporal shape is still an homothetic transformation (Figure IV-20-(a-c)) whereas this is not the case for the spectral shape (Figure IV-20-c). The chirp departs from the linear case as shown in Figure IV-20-(d).

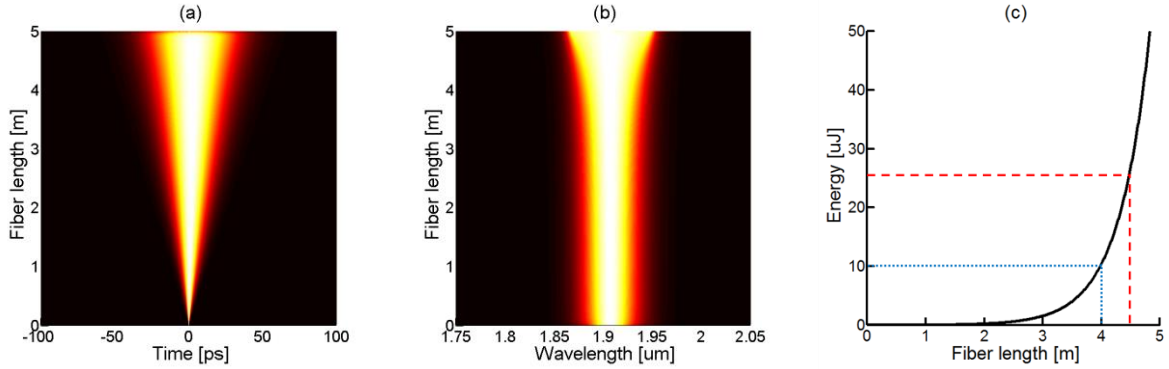


Figure IV-19: Numerical simulations showing the normalized temporal (a) and spectral (b) shape of the pulse along the fiber amplifier. (c) is the energy evolution along the fiber (dotted blue line shows the energy at 4 m and dashed red line at 4.5 m). The input pulse is the realistic pulse from the SFSS source.


BY-NC-ND

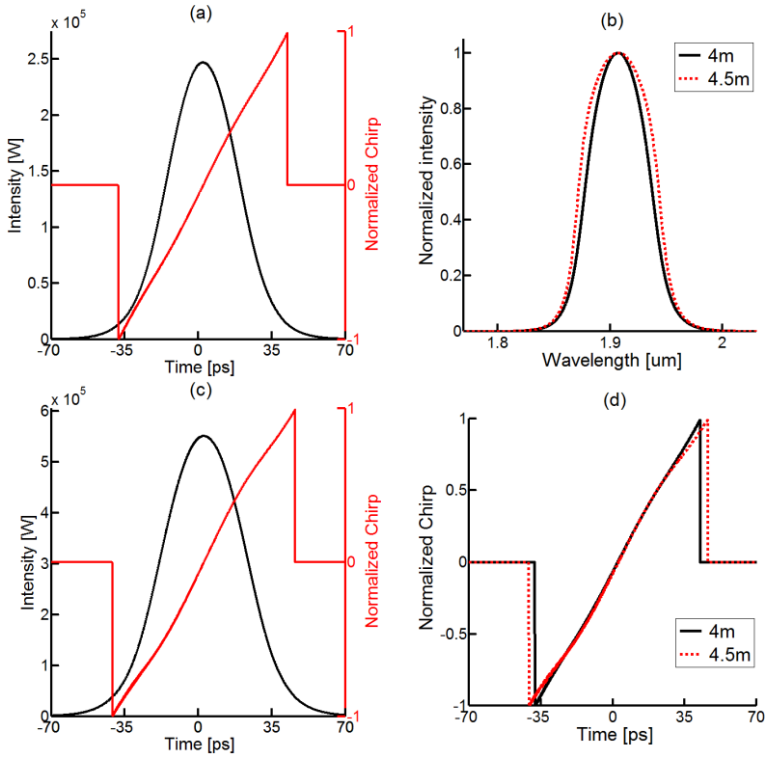


Figure IV-20: Numerical simulations showing (a) the temporal shape and chirp of the pulse after 4 m of fiber. (b) the normalized pulse spectra after 4 and 4.5 m of fiber. (c) the temporal shape and chirp of the pulse after 4.5 m of fiber. (d) The chirp parameter of the pulse after 4 and 4.5 m of fiber. The input pulse is the realistic pulse from the SFSS source.

The maximum energy contained in the pulse while keeping a linear chirp (after 4 m of fiber) is 10.2 µJ. The pulse can be recompressed from 39 ps FWHM to 183 fs by the same gratings compressor line with a distance of 5.6 cm (Figure IV-21). The fraction of energy in the central recompressed lobe is 43% leading to 23.9 MW peak power.

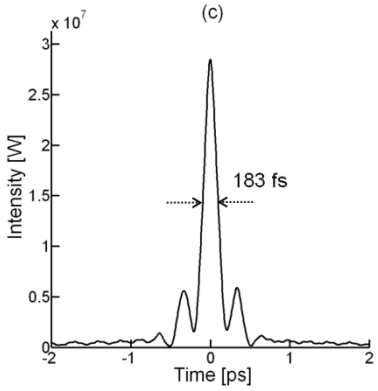


Figure IV-21: Numerical simulations showing the compression of the output pulse (z = 4 m) down to 183 fs FWHMI by a grating compressor in the case of the realistic input pulse (5.2 nJ, 100 fs, 40 nm).


BY-NC-ND

### IV.2.2.2. Effective modal area

For the $LP_{02}$ mode, the dispersion variation arises from a variation in radial electric field distribution, hence it is accompanied with a large variation of the effective area. The wavelength dependence of the effective area is also likely limiting factor that must be taken into account in the modeling. For example, the variation of effective area of the $LP_{02}$ mode versus wavelength is plotted in Figure IV-22. It varies from 149 to 899 µm² between 1.85 and 1.95 µm. This variation directly impacts the calculated value of $\gamma$. The impact of the effective area wavelength dependence is stronger when using the unrealistic pulse since the spectral shape is generated via SPM.

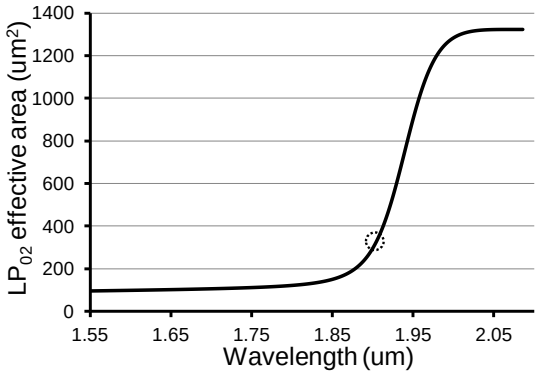


Figure IV-22: Calculated $LP_{02}$ effective area according to wavelength in the optimal fiber. Dotted circle is $A_{eff}^{02}(\lambda_{Dmax})$ = 353 µm².

#### IV.2.2.2.1. Unrealistic 1 ps pulse

During the amplification of the unrealistic 1 ps pulse, the nonlinearities are prone to happen at the blue edge of the pulse due to a lower effective area. Thus, the generation of new frequencies via SPM is no more balanced. This results in producing a 'wall-effect' on the red edge of the pulse, as shown in Figure IV-23-(b), which is directly related to the steep slope of $\gamma$ with wavelength. This results in stopping the spectral, and thus the temporal, broadening.

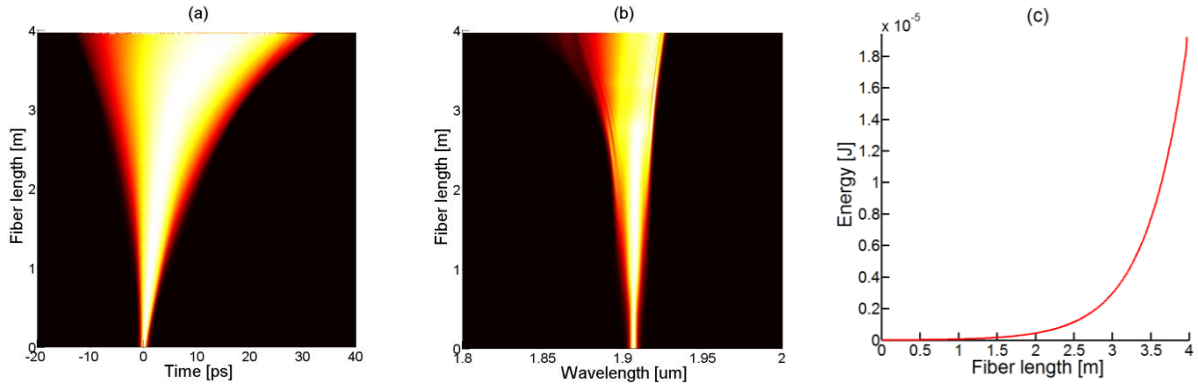


Figure IV-23: Numerical simulations showing (a) temporal and (b) spectral profile of the unrealistic pulse propagating in the optimal few-mode fiber with wavelength-dependent dispersion and effective area. Gain is constant (1.9 Np/m). (c) Evolution of the pulse energy along the amplifier.


BY-NC-ND

The Figure IV-24 shows temporal and spectral profiles as well as the temporal profile of “recompressed” pulse for two cases where wavebreaking is not negligible. Top row shows that SPM happens mainly at short wavelengths due to much reduced effective area unbalancing the temporal and spectral shapes.

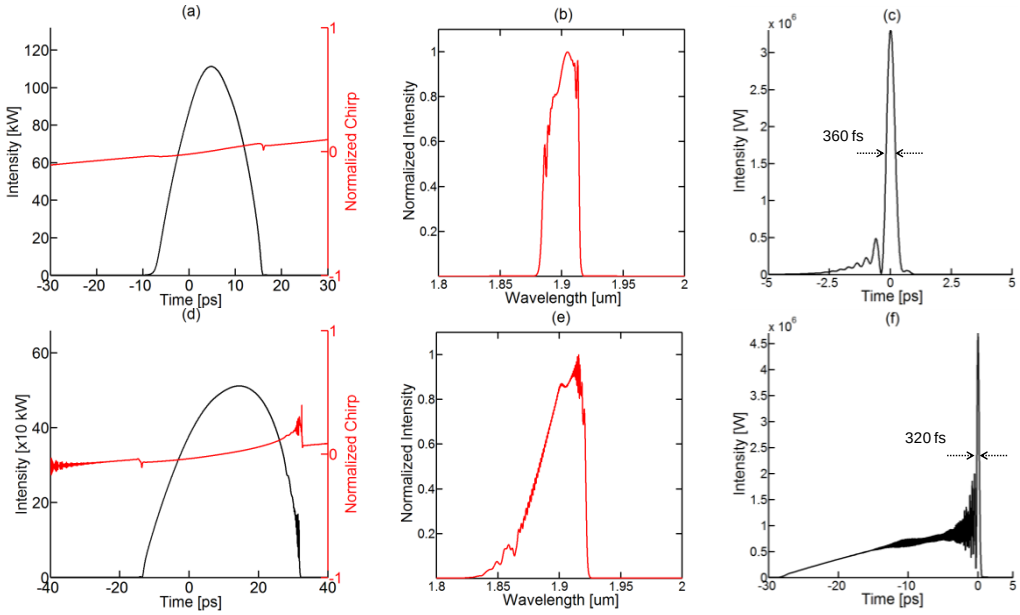


Figure IV-24: Impact of the wavelength dependence of effective area on the pulse. (a) Temporal shape, (b) spectral shape with started SPM and (c) recompressed pulse with 50% energy in central lobe at the fiber length of 2.7 m. (d) Unbalanced temporal shape, (e) highly perturbed spectrum and (f) recompressed pulse with 8% energy in central lobe at the fiber length of 3.9 m.

The chirp, shown in red in the figures above, is no more linear. For reasonably low chirps, the recompressed pulse exhibits a long temporal trail (Figure II-24-(c) and –(f)). This results in lowering the achieved energy before wavebreaking to 1.6 µJ. The FWHM of the recompressed pulse is now 360 fs. Before wavebreaking, the pulse temporal shape is severely unbalanced and SPM has created new shorter wavelength resulting in the impossibility of realizing recompression as shown in Figure IV-24-(d-f).

#### IV.2.2.2.2. Realistic 100 fs pulse

In this case, the ‘wall-effect’ is delayed and only happens after 4 m of fiber (Figure IV-25-(a)). This is due to the delayed generation of wavelengths on the blue side of the pulse as spectral power density is lower. The effective area dependence to wavelength triggers the same effects but with a lower impact compared to a longer pulse. However, the amplified SPM at low effective areas provoke a wavebreaking at 4.7 m as shown in Figure IV-25-(b). 10 µJ can also be expected at 4 m of fiber while at 3.6 m the energy is 4.5 µJ (Figure IV-25-(c) dashed red and dotted blue curves, respectively).


BY-NC-ND

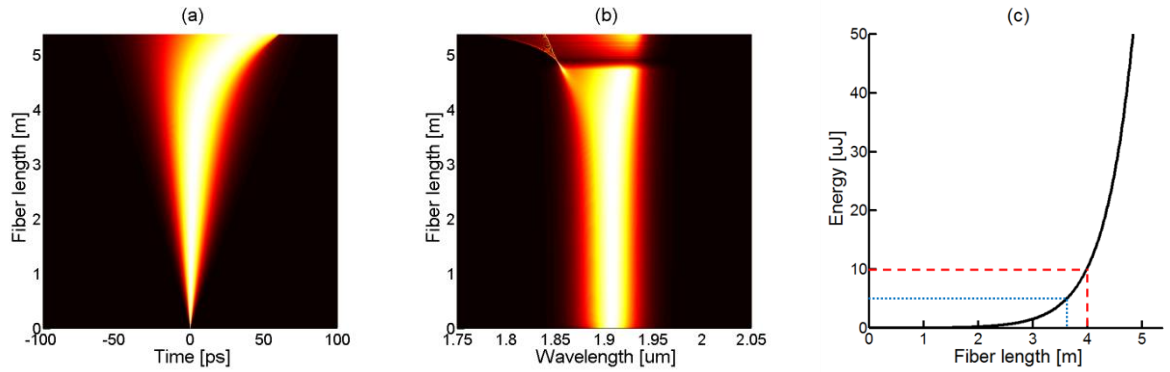


Figure IV-25: Numerical simulations showing (a) temporal and (b) spectral profile of the realistic pulse propagating in the optimal few-mode fiber with wavelength-dependent dispersion and effective area. Gain is constant (1.9 Np/m). (c) Evolution of the pulse energy along the amplifier (dotted blue line shows the energy at 3.6 m and dashed red line at 4 m)

However, the effect of the effective area on the pulse spectrum can be seen as early as at 4 m of fiber. As the pulse experience different $\gamma$ parameters along its spectrum it provokes an unbalance in the spectral growth (Figure IV-26-(b)). This disequilibrium has a direct impact on the pulse chirp (Figure IV-26-(d)) and thus prevent good recompression with the modeled gratings as shown with the unrealistic pulse. The pulse presented in Figure IV-26-(a) can be recompressed from 34 ps FWHM to 183 fs with a grating distance of 5.15 cm (Figure IV-27). The energy fraction contained in the central lobe is 46% leading to 11 MW peak power.

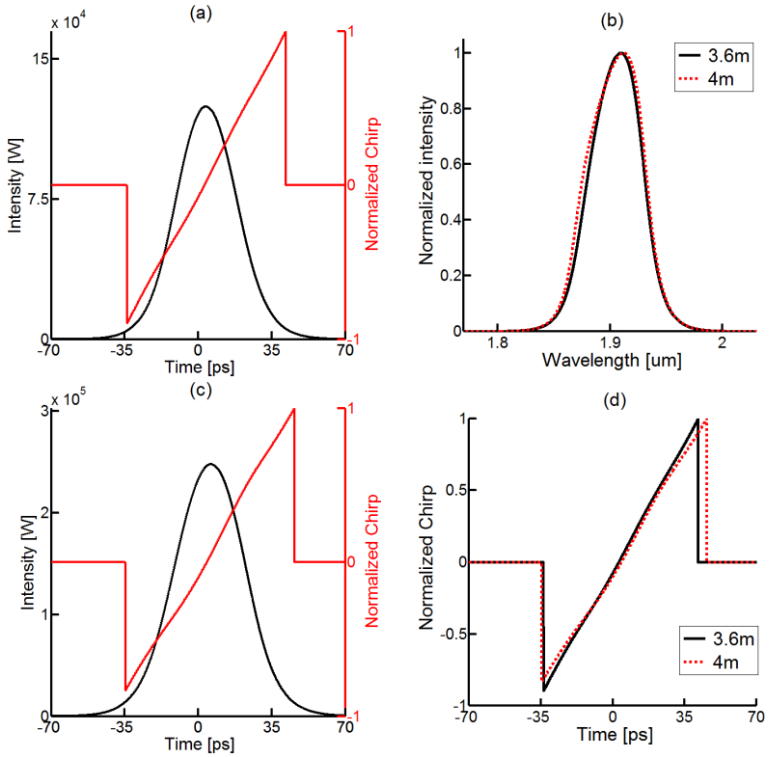


Figure IV-26: Numerical simulations showing (a) the temporal shape and chirp of the pulse after 3.6 m of fiber. (b) the normalized pulse spectra after 3.6 and 4 m of fiber. (c) the temporal shape and chirp of the pulse after 4 m of fiber. (d) The chirp


BY-NC-ND

parameter of the pulse after 3.6 and 4 m of fiber. The input pulse is the realistic pulse from the SFSS source.

The effective area wavelength dependence is a first limitation to the energy scaling of a similariton. The maximum reachable energy without any deformation is scaled by a factor 6 going from 27 to 4.5 µJ when including the effective area variation in the GNLSE. Nevertheless, the microjoule milestone is still in the scope when considering a constant gain over every wavelength. Moreover, the realistic pulse gives better results when the effective area wavelength dependence is considered. Therefore, only the realistic pulse will be studied in the following.

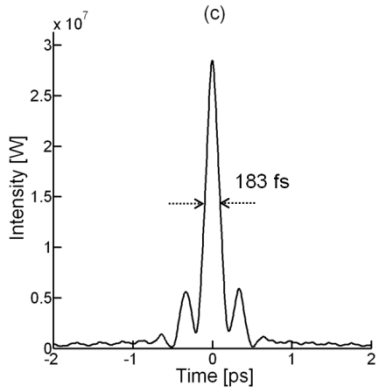


Figure IV-27: Numerical simulations showing the compression of the output pulse (z = 4 m) down to 183 fs FWHMI by a grating compressor in the case of the realistic input pulse (5.2 nJ, 100 fs, 40 nm).

### IV.2.2.3. Gain

The gain dependence to wavelength and fiber length is modeled by feeding the GNLSE with the results of the linear amplification model (Figure II-16-(a)). The effective area is kept constant and equal to 353 µm². In the spectral domain, the shorter wavelengths generated by SPM will experience gain in the first meter of fiber. The blue wing of the pulse will then be gradually reabsorbed, preventing any large spectral broadening via nonlinear effects at short wavelength. This explains the pulse recall observed on the time and spectral domain presented in Figure IV-28-(a-b). The energy is now limited to 99 nJ at $L_{opt}$ equal to 8.78 m due to the gain longitudinal and spectral influence. The pulse shape at $L_{opt}$ is a similariton as shown in figure IV-29-(a-b). The pulse is however delayed of 25 ps due to the back and forth imposed by the SPM combined to available gain at short wavelength along the amplification. During this back and forth, the pulse experience a lot of different high order dispersion values along its spectrum that cannot be recompressed by the compressor line. Nevertheless, for a grating distance of 18.4 cm, the pulse can be recompressed from 66.5 ps to 192 fs with a central lobe containing 63% of the total energy. This leads to a 325 kW peak power.


BY-NC-ND

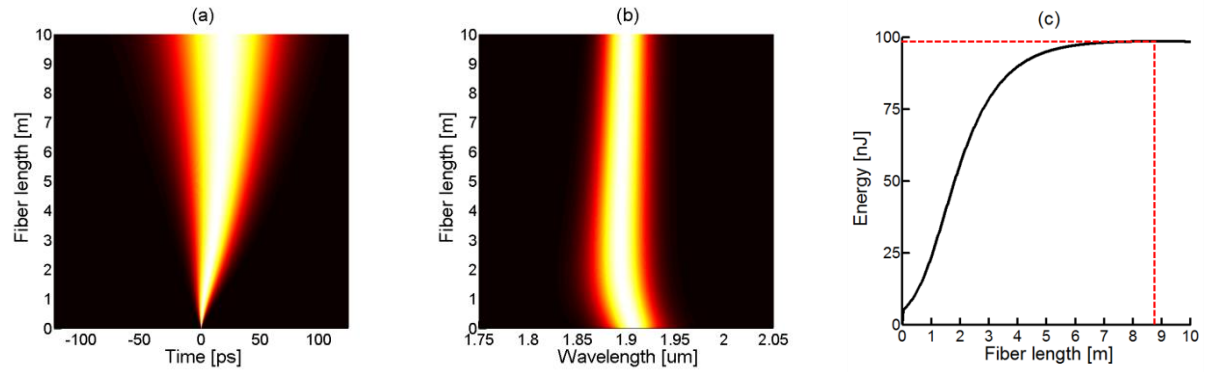


Figure IV-28: Numerical simulations showing (a) temporal and (b) spectral profile of the realistic pulse propagating in the optimal few-mode fiber with wavelength-dependent dispersion and gain. Effective area is constant (353 µm²). (c) Evolution of the pulse energy along the amplifier (dashed red line shows the energy at $L_{opt}$)

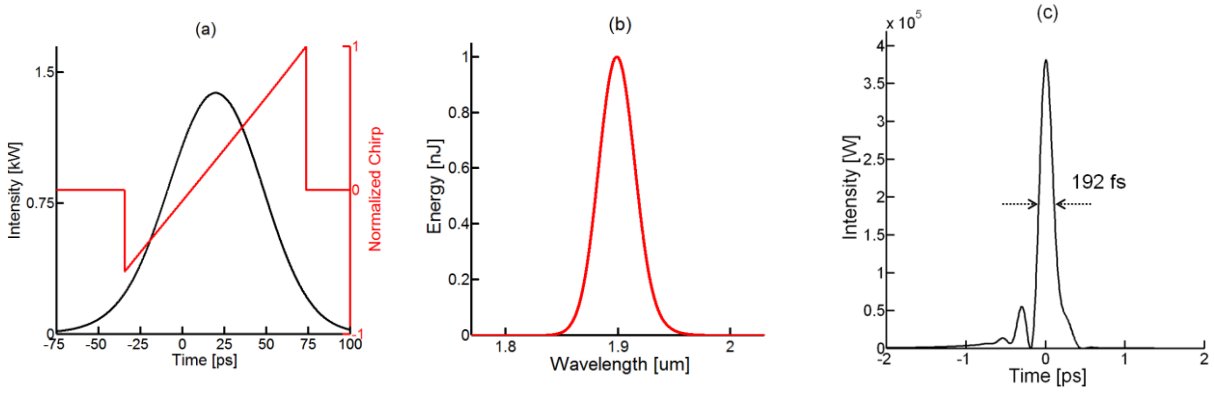


Figure IV-29: Numerical simulations showing (a) temporal and (b) spectral profile of the pulse at $L_{opt}$ in the optimal few-mode fiber with wavelength-dependent dispersion and gain. Effective area is constant (353 µm²). (c) Recompressed pulse with 192 fs duration.

The inclusion of the gain spectral and longitudinal dependence drastically reduces the energy that can be aimed for lowering the value from over 4 µJ to 100 nJ.

### IV.2.2.4. Effective area and gain

Both effective area and gain dependence to wavelength were then implemented in the GNLSE giving the pulse normalized temporal and spectral evolutions along the fiber shown in Figure IV-30-(a-b). The inclusion the effective are dependence to wavelength reduces the $L_{opt}$ to 7 m. This can be explained by the enhanced SPM produced at the blue side of the pulse being amplified at the beginning of the fiber. These wavelengths will have stored more energy compared to the constant effective area case. A balance in total energy between the re-absorption of these wavelengths and the amplification of the red part of the pulse is established. The highest value of energy can therefore be reached at shorter pieces of fiber but with a spectrum centered at a shorter wavelength compared to the constant effective area case. This is confirmed by the spectral shape of the pulse at $L_{opt}$ shown in Figure IV-31-(b). The energy at $L_{opt}$ is 100 nJ which is close to what we had obtained with a


BY-NC-ND

constant effective area. No other change in the pulse behavior can be noticed from the inclusion of the effective area variation according to wavelength.

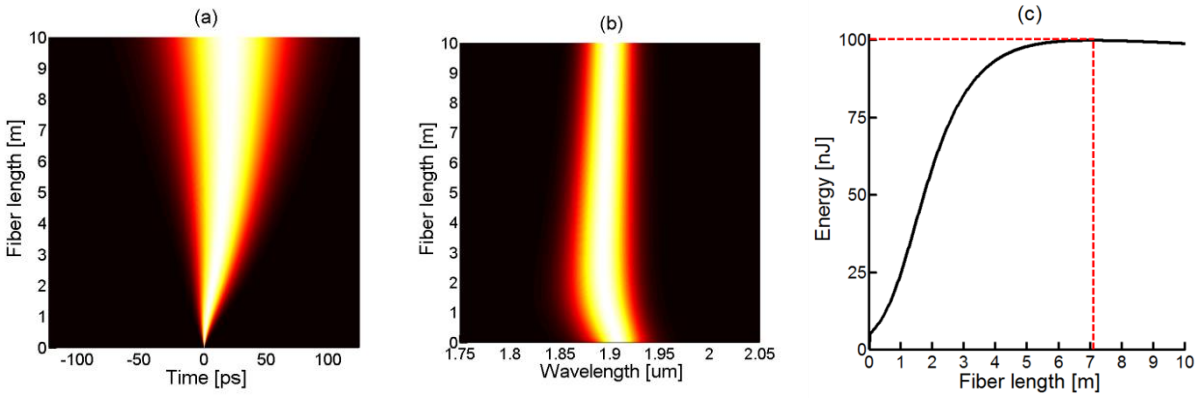


Figure IV-30: Numerical simulations showing (a) temporal and (b) spectral profiles of the realistic pulse propagating in the optimal few-mode fiber with wavelength-dependent dispersion, effective area and gain. (c) Evolution of the Energy along the fiber amplifier (dashed red line is the energy at $L_{opt}$).

In Figure IV-31 are shown the temporal and spectrum intensities at $L_{opt}$ and the recompressed pulse. The temporal broadening of the pulse is asymetric due to lower wavelengths being generated and amplified leading to a pulse FWHM of 58.4 ps with a 18.7 ps delay. SPM does not occur at longer wavelengths due to the large effective area, one order of magnitude larger than that at shorter wavelengths as well as low distributed gain. The spectral broadening is thus limited by the gain and the absorption at shorter wavelengths and by the large effective area at longer wavelengths. Moreover, the shorter wavelengths will experience different higher order dispersions (sign of beta4) compared to the longer wavelengths. This delays the pulse and makes it asymmetric. Due to those limiting effects, the output energy is reduced to 100 nJ. However, the output pulse can still be recompressed down to 192 fs. The central peak contains 52% of the total energy leading to 272 kW peak power.

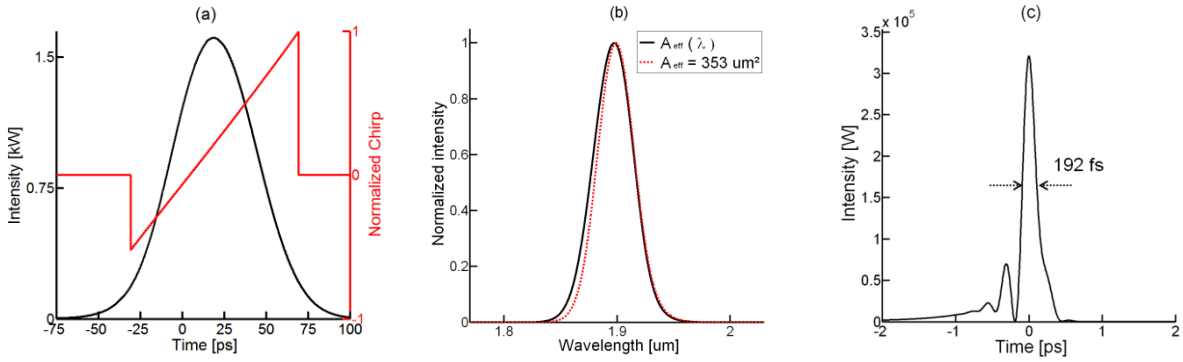


Figure IV-31: Numerical simulations showing (a) temporal and (b) spectral profiles of the realistic pulse at $L_{opt}$ in the optimal few-mode fiber with wavelength-dependent dispersion, effective area and gain. (c) Temporal shape of the recompressed pulse with 192 fs duration FWHM containing 52% of the output energy.


BY-NC-ND

We are far from the µJ threshold in this configuration. However, if the input average power of 250 mW is kept, thus keeping the same modeled distributed gain, it is possible to seed the parabolic amplifier with higher energy by lowering the input repetition rate. Thus, the repetition rate was swept from 10 MHz to 48 MHz to confirm that this fiber could produce close to the µJ level of energy. The results are summarized in Tab IV-10.

Table IV-10: Results from numerical simulations showing the maximum extractable energy as a function of the input pulse energy. The input average power is equal to 250 mW.

| Repetition rate (MHz) | $E_{in}$ (nJ) | $L_{opt}$ (m) | $E_{Lopt}$ (nJ) | $\Delta t_{compressed}$ (fs) | Energy fraction in central lobe (%) | Peak power (MW) |
|---|---|---|---|---|---|---|
| 48 | 5 | 7.04 | 100 | 192 | 52 | 0.272 |
| 30 | 16.7 | 5.96 | 161 | 192 | 48 | 0.402 |
| 10 | 50 | 4.18 | 511 | 175 | 36 | 1.05 |

Seeding with more energy results in taking advantage of the gain in the blue part of the spectrum thus reduces $L_{opt}$. Megawatt class pulses can be expected after compression when taking extra care on the input energy. There is still room for improvement when considering the gain of the fiber having a spectrum that is not perfectly matched with the pulse.

### IV.3. Fabricated active few-mode fiber

A very first active fiber has been manufactured by the MCVD process at IRCICA/PhLAM. Measured RIP and dispersion curve computed for the $LP_{02}$ mode taking the actual RIP into account are shown in Figure IV-28 (a-b). As is the case for the passive fiber, the high index ring is lower than expected increasing the sensitivity of the $LP_{02}$ mode to the curvature. The trench actually vanishes, which is expected to impact on the dispersion value. Despite the discrepancy between the target and the actual RIP, negative chromatic dispersion is obtained around 2 µm. The minimal value is -68 ps/nm/km at 1928 nm comprised in the Tm-ion emission band. The calculated effective area of the $LP_{02}$ mode at $\lambda_{Dmax}$ is 399 µm² giving an expected FOM of 27 fs.

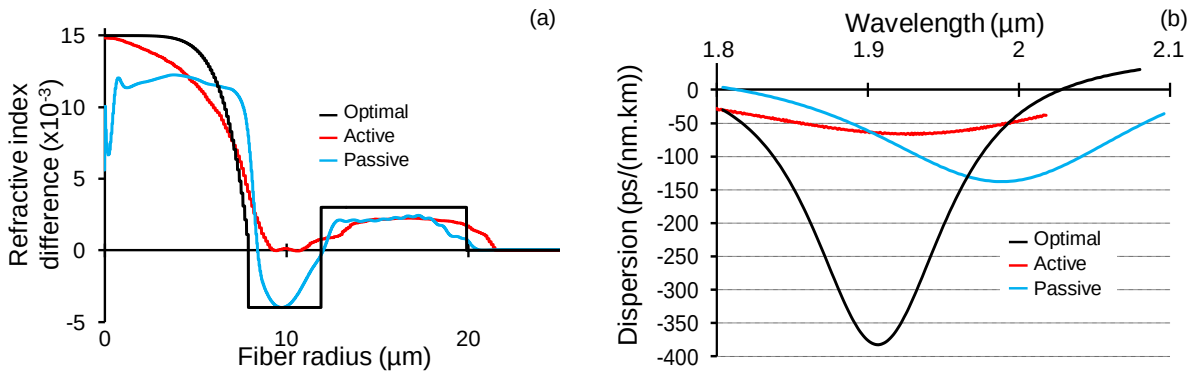


Figure IV-32: (a) Measured refractive index difference of the active (red) and passive (blue) few mode fiber. Black line shows the target RIP. (b) Dispersion curves computed for the three RIPs shown in (a).


BY-NC-ND

In order to evaluate the potential hold by this fiber for parabolic amplification, I have seeded the GNLSE with the modal parameters ($A_{eff02}(\lambda)$, $n_{eff02}(\lambda)$ and $G_{02}(z,\lambda)$ computed taking the active fiber RIP into account. The $LP_{02}$ is supposed to be the single excited mode. Figure IV-29-(a) shows $G_{02}(z,\lambda)$ calculated with an input hyperbolic secant spectral distribution centered at $\lambda_{Dmax}$ = 1.928 µm with 250 mW of input power. The pump power was 6 W at the wavelength of 1.535 µm. The input pulse parameters are taken from Table IV-9. The longitudinal evolution of the temporal and spectral profiles are shown in Figure IV-29-(b-c). The stored energy within the pulse longitudinal evolution is presented in Figure IV-29-(d).

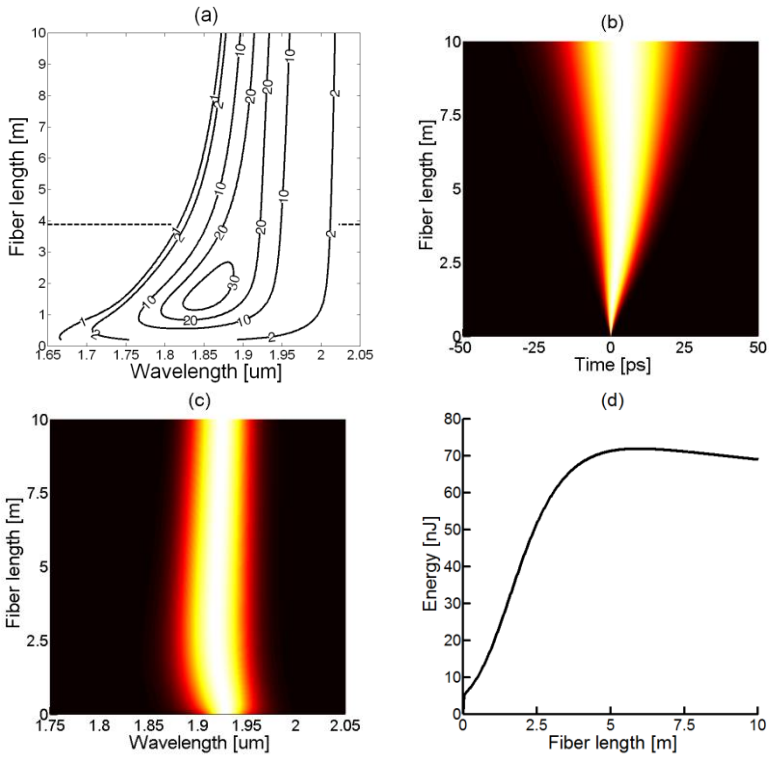


Figure IV-33: Numerical simulations showing (a) the gain of the $LP_{02}$ mode according to wavelength and fiber length in the realized active few-mode fiber. (b-c) The pulse temporal and spectral shapes along the amplifier. (d) The energy evolution along the amplifier.

SPM is balanced over the pulse bandwidth (balanced temporal shape) thanks to the rather slow variation of effective area, from 254 to 540 µm², in the bandwidth 1.85-1.97 µm. Furthermore, high gain is available at short wavelengths up to 3 m of fiber allowing the amplification and propagation of the new wavelengths generated through SPM. After 4 m, these wavelengths are reabsorbed leading to some asymmetry in the pulse spectrum. Nevertheless, similariton pulse propagation is maintained along the whole fiber. This is confirmed by the linear chirp achieved at the output of the fiber (Figure IV-30-(a)). The energy at $L_{opt}$ is 72 nJ. The amplifier thus presents 11.6 dB of gain. The pulse temporal and


BY-NC-ND

spectral shapes at $L_{opt}$ are presented in Figure IV-30-(a-b) and its maximal achieved compression in Figure IV-30-(c).

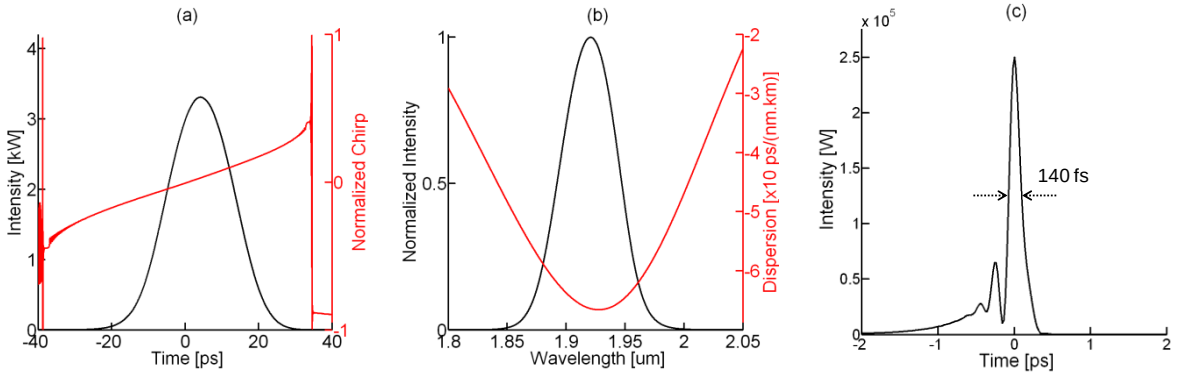


Figure IV-34: Numerical simulations showing (a-b) the temporal and spectral shape of the amplified pulse at $L_{opt}$. (c) The temporal profile of the recompressed pulse with 140 fs duration. The central lobe contains 55% of the output energy.

The pulse can be compressed down to 140 fs FWHM with a grating distance of 3 cm. The central lobe contains 55% of the output energy. This leads to over 230 kW peak power. As in 6.2.2., the repetition rate was lowered to increase the amount of input energy, the results are presented in Table IV-10.

Table IV-11: Numerical simulations showing the scalability in peak power in the active few mode fiber for different input energy with constant average power (250 mW).

| Rep_rate (MHz) | $E_{in}$ (nJ) | $L_{opt}$ (m) | $E(L_{opt})$ (nJ) | $\Delta t_{compressed}$ (fs) | Energy fraction in central lobe (%) | Peak power (MW) |
|---|---|---|---|---|---|---|
| 48 | 5.2 | 5.95 | 72 | 140 | 46 | 0.237 |
| 30 | 8.3 | 5.45 | 114 | 140 | 43 | 0.350 |
| 10 | 25 | 4.31 | 330 | 120 | 36 | 1 |

As with the optimal fiber, lowering the repetition rate to 10 MHz allowed reaching the milestone of 1 MW peak power. This is mainly due to the low effective area variation enabling the SPM generation over a broader spectrum compared to the optimal fiber.

In both cases, we are far from the limitations dictated by the fiber geometrical characteristics, namely dispersion and effective area. The barrier that has to be surpassed is the fiber gain behavior that forbids energy scaling.

### IV.4. Conclusion

A singlemode Tm-doped fiber was manufactured at IRCICA-PhLAM to study the efficiency of the glass matrix that will be further used in the active few-mode fiber. The $Tm^{3+}$-ion radial distribution had to be taken into account to allow reaching very good agreement between the model and the measurements. An in-house (3+1)D (x,y,z and $\lambda$) amplifier software was used to model the $LP_{02}$ mode gain evolution according to fiber length and wavelength ($G_{02}(z,\lambda)$). In order to push away the gain saturation, the pump wavelength has to


BY-NC-ND

be lowered and was thus fixed to 1.535 µm. Along the amplification, the modal weight of the $LP_{02}$ could suffer strong changes due to the low overlaps between the modes carrying the pump and the signal. To lower the strength of the modal weight reduction it has be demonstrated that the pump should also be carried by the $LP_{02}$. Another way was studied using an enhanced design of the fiber. The incorporation of a central dip in the RIP allowed lowering the overlap between the gain media and the fundamental mode. This enhanced design transfers the necessity of mode conversion at the pump wavelength to a necessity of long pieces of fiber. The length of an amplifier based on this design can be managed by changing the pump wavelength. Moreover this design increases the $LP_{02}$ modal weight along the amplification. This design is currently being manufactured at IRCICA-PhLAM.

Armed with these parameters, the in-house GNLSE software has been fed by several parameters: the pulse characteristics of the SFSS source; the dispersion, the effective area and the gain of the $LP_{02}$ mode. The proposed optimal design allows reaching 0.1 µJ at $L_{opt}$. The pulse could be recompressed to 192 fs with a central lobe containing 52 % of the energy leading to 270 kW peak power.

A very first active few-mode fiber presenting high $-D$ was manufactured and numerically studied. This fiber could allow reaching over 230 kW peak power in a recompressed pulse of 140 fs. If the repetition rate is lowered all other things being equal, the 1 MW milestone can be reached with this fiber.


BY-NC-ND

## General Conclusion and prospects

The goal of this thesis was to pave the way towards the demonstration of all-fiber format high energy amplification at 2 µm. Parabolic amplification is a good candidate but this amplification regime is prohibited in silica at 2 µm due to the large anomalous dispersion of the material. Furthermore, according to $\hat{E} = c/(8gn_2) \times D^2(\Delta\lambda)^3 A_{eff}/\lambda$ high energy amplification at 2 µm would need a special Tm-doped fiber with both high normal dispersion (*–D*) and large effective mode area ($A_{eff}$). Waveguiding effects are inhibited by nature in large mode area singlemode fibers thus preventing the design of single large mode area fibers with high *–D* at 2 µm.

Ramachandran and coworkers [27], [29] have widely used the possibilities offered by high order modes in terms of dispersion control in the telecom window using passive few mode fibers. These modes exhibit high *–D* and large mode area near their respective cut-offs. However, optimized designs for direct amplification to high energy in the normal dispersion regime were never reported up to now.

In this thesis, I have presented the different steps to design a fiber that can be manufactured by MCVD and that gathers all attributes necessary to initiate parabolic amplification around 2 µm. The proposed fiber presented a W-like refractive index profile (RIP) and guided the first four LP modes. The dependence of the dispersion curve of the $LP_{02}$ mode to the RIP is strong. The $LP_{02}$ mode of the modeled fiber exhibits a high negative dispersion value of $D$ = -380 ps/(nm.km) at $\lambda_{Dmax}$ = 1.908 µm with a corresponding effective mode area of 353 µm². A passive version was first realized by our partner IRCICA/PhLAM. Despite the discrepancy between the target fiber and the realized fiber, the calculated $LP_{02}$ mode of the later exhibits a dispersion value of -137 ps/(nm.km) combined with an effective area of 393 µm² at $\lambda_{Dmax}$ = 1.99 µm. This fiber constitutes the first milestone towards parabolic amplification at 2 µm. However, careful launching into the $LP_{02}$ mode is necessary to take advantage of its exceptional modal parameters at this wavelength.

Two ways to realize a selective excitation of the $LP_{02}$ mode in the passive fiber have been investigated during this thesis and are presented in the second chapter. On one hand, the use of Long Period Gratings (LPG) was studied. A collaboration between XLIM and the Ecole Polytechnique Fédérale de Lausanne (EPFL) in Switzerland has been established during this thesis to manufacture LPGs in our fibers. The fiber in which the LPGs were written presented high normal dispersion around 1.55 µm for the $LP_{02}$ mode while the mode matching between the fundamental and the $LP_{02}$ modes was expected around 1.54 µm. The first result we obtained was a 40% mode converter around 1.7 µm using a grating period of


BY-NC-ND

170 µm. During this study I concluded that LPGs add another degree of complexity on the RIP in order to match the mode conversion bandwidth with the high normal dispersion bandwidth.

On the other hand, a spatial mode converter was manufactured at XLIM using the hole-inflation technique in a PCF cane. This mode converter allowed the spatial structuration of light from the input SMF to a $LP_{02}$–like mode at its output. Contrary to LPGs, no spectral filtering due to the conversion bandwidth was expected as the conversion was realized over a broad spectral bandwidth of 400 nm from 1.5 µm to 1.9 µm. This spatial mode converter thus holds potential to convert both pump and signal radiations. This mode converter was then used to excite the passive few mode fiber sample. However, a camera image did not allow us to conclude on the purity of excitation. During my thesis, I have implemented at XLIM the spectrally- and spatially-resolved imaging technique ($S^2$) as first described by Nicholson and coworkers [33]. Using this technique on the association 'mode converter-passive few mode fiber' gave state-of-the-art results in terms of purity of excitation of a higher order mode. Parasitic modes presented multi-path interference values lower than -35 dB at 1.55 µm and at 1.87 µm. This type of mode converter constitutes the second milestone towards parabolic amplification at 2 µm. The output facet of the dedicated mode converter made at XLIM was unfortunately damaged and could not be used anymore. Dr. Correa from CREOL provided us with photonic lanterns [35]–[38] to further investigate on high purity mode excitation. These lanterns are still under test.

As explained in Liu's thesis [5], the amplification of parabolic pulses require the input pulse duration to be on the order of 100 fs. To address this mater, I fabricated a pulse source based on self-frequency shifted soliton producing 100 fs duration pulses with an average power of 250 mW. This source is tunable from 1.6 µm to 2 µm by adjusting the pump power of the last stage amplifier that produces the Raman-shifted soliton. This source allowed us to measure the $LP_{02}$ dispersion in the passive few mode fiber at the wavelength of 1.95 µm, $D$ = -106 ps/(nm.km), in very good agreement with the calculated value of -108 ps/(nm.km).

The last chapter summarizes the numerical studies on an active version of the calculated fiber in both linear and nonlinear amplification. The glass matrix efficiency was first measured in a singlemode Tm-doped fiber. Then, a (3+1)D (x,y,z and $\lambda$) amplifier software modeling the modal gain competition taking the transverse distribution of $Tm^{3+}$-ion allowed us to compute the spectral and longitudinal evolution of the $LP_{02}$ modal gain. By design, the dispersive fiber presents a decreasing overlap between the active-core and the $LP_{02}$ mode with wavelength. This results in deteriorating the modal purity along the amplification. A solution (controlled dip in the Tm-doped portion of the refractive index profile) was proposed


BY-NC-ND

to enhance the modal purity along the amplification. This fiber is being manufactured by our partner IRCICA-PhLAM.

In the in-house GNLSE solving software were injected the spectral and longitudinal evolution of the $LP_{02}$ gain combined with both the fiber geometrical characteristics and the SFSS source pulse parameters. The proposed optimal design allows reaching 0.1 µJ at $L_{opt}$. The pulse could be recompressed to 192 fs with a central lobe containing 52 % of the energy leading to 270 kW peak power.

A very first active few-mode fiber presenting high $-D$ was manufactured and numerically studied. This fiber could allow reaching over 230 kW peak power in a recompressed pulse of 140 fs. If the repetition rate is lowered all other things being equal, the 1 MW milestone can be reached with this fiber.

In terms of prospects, the use of photonic lanterns as mode converters makes easy the excitation of the $LP_{02}$ mode. We are currently investigating on the photonic lanterns that were delivered to XLIM. Their use in an ultrashort pulse laser would be a world first. Using this device with the current active fiber might lead to a proof of concept of parabolic amplification at 2 µm. However, the expected excitation purity with such devices is on the order of -10 dB [37]. The association of the photonic lanterns with the enhanced design fiber will surely produce interesting results and demonstrate the energy scaling via parabolic amplification at 2 µm. We are also studying the homemade spatial mode converter with special care paid to a monolithically integrated system.


BY-NC-ND

## Appendix. Experimental determination of the modal content by means of S2 imaging

The beam quality at the output of the fiber as always been thoroughly investigated. Since standard fiber lasers operate on the fundamental mode which have a nearly Gaussian shape the well-known $M^2$ measurement was sufficient in most cases to describe the output beam. However, there exist situations in which the $M^2$-parameter is low (indicating good beam quality), yet the beam contains a significant amount of higher-order mode content [44]. The resulting modal interference causes beam fluctuations in the far-field. With the renewed interest on multimode fibers, other type of characterizations arose that can be sorted into two categories. On one hand, there are methods that need a prior knowledge of the measured fiber. From the known modal content and the output beam shape one can retrieve any weight of each mode participating to the formation of the output pattern. Using a modal decomposition into LP modes [45] the intensity of each modes can be retrieved. An enhanced version have been proposed [46] using wavefront analysis so as to get the intensity profiles and the phase of each modes constituting the output beam. On the other hand, techniques that make no assumptions about the fiber under test have been demonstrated. These techniques rely on the fact that the fiber modes travel at different group velocities. Hence, one can retrieve each excited mode using a fair amount of fiber length ensuring temporal separation of each mode. Techniques such as Spectrally- and Spatially-resolved imaging ($S^2$) [33], optical low-coherence interferometry [47], [48] and cross-correlation imaging ($C^2$) [49] are available and do require either a fixed spectral range and a spatial sweep or a fixed spatial range and a spectral sweep. In our case, the measurement of the modal content is to be realized over the erbium and thulium emission bandwidths on an unknown fiber modal content. For most of the second category techniques mentioned above, the only, and fast, way is to use a tunable laser (spectral sweep) and a CCD camera (fixed spatial range). However, the lack of tunable lasers around 2µm and of high resolution camera or the expansiveness of such devices forced to consider the use of a rare-earth-based ASE source (fixed spectral range) and a 2D spatial mapping. The strength of $S^2$ relies in the possibility to use both ways (fixed spectral range and spatial sweep or the other way around) without the need of a reference (as opposed to $C^2$) to perform the measurement.

$S^2$ has been demonstrated by Nicholson and coworkers [33] and rely on the assessment that a multimode fiber guiding N modes behaves as an N unbalanced arms interferometer. Therefore, if one arm has a dominating intensity, the resulting interferences will be from this arm with others. Less excited arms interfering with others are neglected in this approach. In this scenario, the produced interferograms will provide sufficient data to enable the evaluation of the modal content at the output of any kind of fibers. In its


BY-NC-ND

demonstration, spectral interferences were spatially resolved. Fringes in the optical spectrum could be identified as peaks in the temporal domain through the use of Fourier transform. For a detailed theortical explanation the reader is invited to look into ref [33], [50].

### A.1. Modeling

In its basic form, S² measurement requires a preponderant mode over the others. It is commonly used with a preponderant fundamental $LP_{01}$ mode which eventually will not be our case. Modeling is then required to foresee the possible different interference patterns since every reconstruction and MPI evaluation will be realized with a preponderant $LP_{02}$. The following simulations model the S² measurements of the designed optimal fiber (Chapter II.4) excited by a flat ASE source. The interference patterns are generated between 1.83 and 1.87 µm with a spectral resolution of 40 pm. Two excitation conditions are modeled with either $LP_{01}$ or $LP_{02}$ being the main mode. The weight of each mode and the averaged calculated differential group delays normalized by the fiber length (fDGDs) between the main mode and the other modes are summed up table A-1.

Table A-IV-12: S² modeling with two distinct excitations and corresponding differential group delays.

| Mode | Main mode | | | |
|---|---|---|---|---|
| | LP01 | | LP02 | |
| | Power fraction (%) | fDGD (ps/m) | Power fraction (%) | fDGD (ps/m) |
| LP01 | 97 | | 1 | 5.51 |
| LP11 | 1 | 6.16 | 1 | 0.69 |
| LP21 | 1 | 11.58 | 1 | 6.07 |
| LP02 | 1 | 5.51 | 97 | |

The expected MPI is equal to -19.87 dB for each mode as their weight is equal. Using the mode solver described in Chapter II, the radial field distributions and effective indices of each mode at every wavelength are computed. From those radial distributions are created 2D distributions normalized in intensity. A pixel by pixel interference spectrum is generated using the computed effective indices while introducing controlled weight on each guided mode as described by the following equations:

$$E_{nm}(x,y,\lambda) = Amp_{nm} Dist_{nm}(x,y) e^{(-jk_0 n_{eff-nm}(\lambda) L_{fiber})} \quad \text{(A.1)}$$

$$\text{Interf}(x,y,\lambda) = \left( \sum_{\text{modes}} E_{nm}(x,y,\lambda) \right) \times \text{c.c.} \quad \text{(A.2)}$$

where $E_{nm}$ is the electrical field of the $LP_{nm}$ mode with the 2D distribution $Dist_{nm}$, $Amp_{nm}$ is the square root of the fraction of power contained in the mode (given in Tab III-1), $n_{eff-nm}$ is the wavelength dependent effective index of the considered mode and $L_{fiber}$ the simulated fiber


BY-NC-ND

length. *Interf* is the generated interference spectrum which stands for the measured spectrum in the experiment.

Inverse Fourier transform is performed at each point of the matrix which contains an optical spectrum. Taking the modulus of the inverse Fourier transform will lead to amplitude interference patterns while taking the phase will enable phase interference patterns.

### A.1.1. Preponderant $LP_{01}$ mode

The obtained temporal traces are summed so as to extract the interferences peaks from noise. The fDGDs and interference patterns can be identified and observed at that point (Figure A-1).

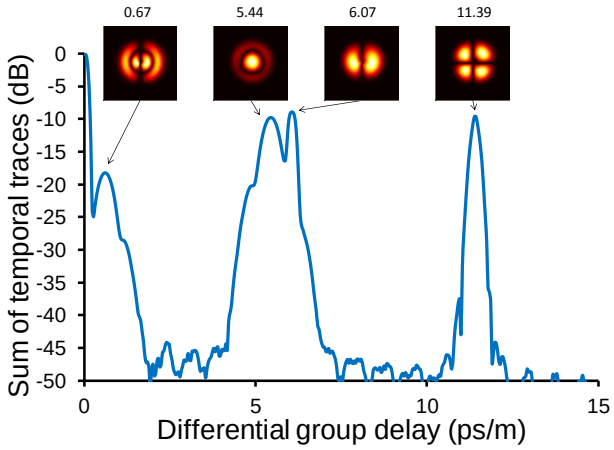


Figure A-IV-35: $S^2$ modeling - preponderant $LP_{01}$: differential group delay, normalized by the fiber length, identification with correlated 2D interference patterns in insets.

The peak at null DGD represents the superposition of all 2D interference patterns (2D-IP) and is equivalent of what a camera could record at the fiber output.

While using the fundamental $LP_{01}$ mode as the main mode, 2D-IP and reconstructed modes produce rather similar pictures. The main difference being that the 2D-IP seems to be compressed towards the center. The retrieved fDGDs agree well with the expected values. Moreover, as can be seen on Figure A-1, a spurious peak can be noticed at fDGD = 0.67 ps/m. It gives a 2D-IP of the form of the $LP_{12}$ mode which is not a guided mode of the simulated fiber. This peak is consistent with the one between the $LP_{02}$ and the $LP_{11}$ as noted in Tab III-1. This gives an insight of what can be expected in terms of 2D-IP in the case of a preponderant $LP_{02}$ mode.

Using the calculation of the 'f' and $\alpha$ parameters the mode intensities and phases can be reconstructed and their respective weights identified.


BY-NC-ND

Table A-IV-13: S² modeling - preponderant $LP_{01}$: Reconstructed mode intensity and phase with respective differential group delays and multi-path interference

| | Intensity | Phase | fDGD (ps/m) | MPI (dB) |
|---|---|---|---|---|
| $LP_{02}$ | 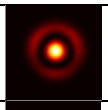 |  | 5.44 | -21.06 |
| $LP_{11}$ |  |  | 6.07 | -19.27 |
| $LP_{21}$ | 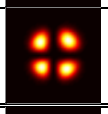 | 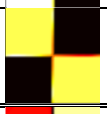 | 11.39 | -19.76 |
| Mix $LP_{02}$ and $LP_{11}$ | 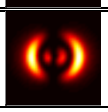 |  | 0.67 | |

Table A-2 summarizes the different retrieved mode intensity and phase profiles as well as their respective MPIs. Gray and coworkers [51] demonstrated that a 7 points window integration centered on the peak allow retrieving accurate weight, when being sure that the summed points do describe the same peak. With this integration window, the respective MPIs of the $LP_{11}$ and $LP_{21}$ agree well with the expected value of -19.87 dB. The lower retrieved MPI for the $LP_{02}$ is explained by the fact that the width of its peak is wider than the others since it is highly dispersive. Therefore, it requires a wider integration window, in this case 15 points, to retrieve a MPI of -19.31 dB. Experimentally, being sure that the summed points belong to only one peak might not be possible, especially with such a wide integration window. This results in under evaluating the MPI by a maximum of 3 dB (when only one point is taken). It is noticeable that when the $LP_{02}$ and $LP_{11}$ interfere, the resulting phase pattern is the sum of both phases.

### A.1.2. Preponderant $LP_{02}$ mode

On the contrary, if the $LP_{02}$ mode has the highest weight, interference patterns are quite different and may show unexpected results. In intensity, those patterns lead to a biased reconstruction since the $LP_{02}$ mode presents a zero and is used as the denominator in ‘f’. This produces singularities on all reconstructed modes. Therefore, MPI values while using $LP_{02}$ mode as the main mode will be underestimated. The results of the modeling are summarized in Tab III-3. The fDGDs still agree well with the expected values. As previously noticed, the reconstructed phases are the superposition of the $LP_{02}$ mode with the interfering mode. The $LP_{01}$ 2D-IP strongly resembles the $LP_{02}$ mode but the reconstruction helps clearing up the doubt. However, all MPI values are underestimated by roughly 6 dB. This value is only linked to the suppression of the modal distribution of the modes and is thus


BY-NC-ND

independent of the excitation conditions. Therefore, in any further MPI measurements involving the $LP_{02}$ mode as the preponderant one, MPI values will be corrected by +6 dB.

Table A-IV-14: S² modeling - preponderant $LP_{02}$: 2D interference patterns, reconstructed mode intensity and phase with respective differential group delays and multi-path interference

| | 2D-IP | Intensity | Phase | fDGD (ps/m) | MPI (dB) |
|---|---|---|---|---|---|
| $LP_{11}$ | 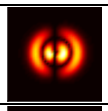 | 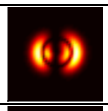 |  | 0.63 | -25.55 |
| $LP_{01}$ | 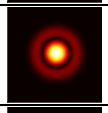 | 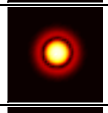 | 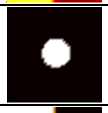 | 5.44 | -25.01 |
| $LP_{21}$ | 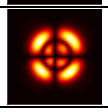 | 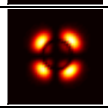 |  | 5.95 | -25.24 |

### A.1.3. Water absorption influence

In the S² measurement, the biggest temporal window requires the smallest spectral step. This will allow the resolution of thin absorption peaks of any airborne components present in the spectrum analyzer or in free space. Working in the thulium emission bandwidth has proven to be difficult in free space due to water absorption peaks. Gaida and coworkers [21] have put their CPA in a controlled climate chamber ensuring a very low humidity to achieve proper compression. If not regulated, the air humidity is roughly of 25%. The free space optical path in an optical spectrum analyzer is around 1 m. When considering those two parameters, the water contribution to spectrum is as follows (Figure A-2).

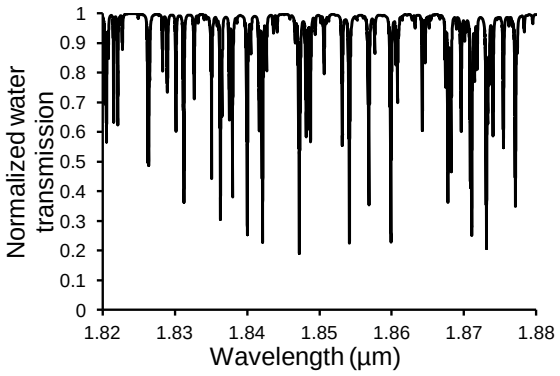


Figure A-IV-36: Water transmission from 1.82 µm to 1.88 µm in a 1 m gaz cell with 25% humidity (http://spectralcalc.com/).

The water contribution to spectrum was implemented at the spectrum generation step hence modifying the Equation A.2:

$$Interf(x,y,\lambda) = Water(\lambda) * \left[ \left( \sum_{modes} E_{nm}(x,y,\lambda) \right) \times c.c. \right] \qquad (A.3)$$


BY-NC-ND

where *Water*(λ) is the transmission spectrum of Figure A-3-(a). For example, in the case of the $LP_{02}$ mode being preponderant, the shape of the sum of temporal traces and of reconstructed modes are strongly changed by water contribution as shown in Figure A-3-(b).

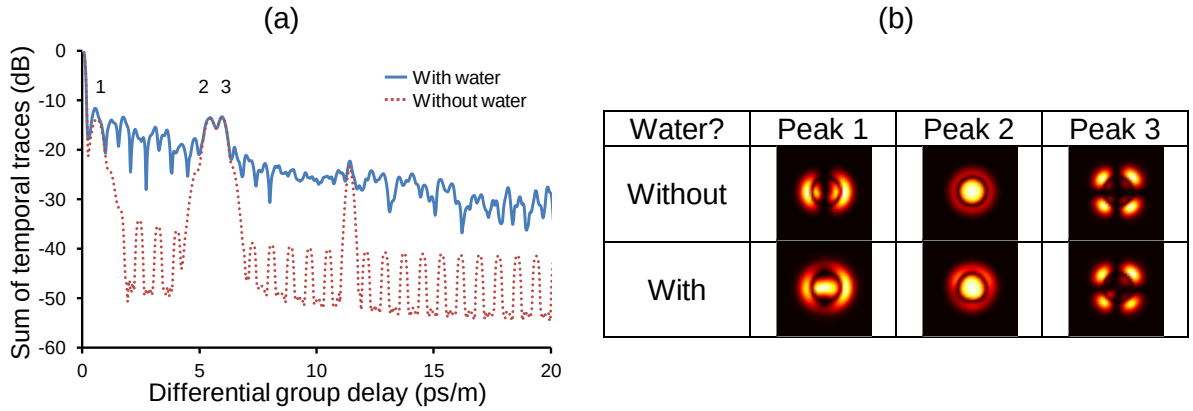


Figure A-IV-37: (a) Sum of temporal traces in the case where the $LP_{02}$ mode is preponderant with and without water contribution. Labeled peaks refer to interferences with the $LP_{02}$ mode (b) Comparison of the reconstructed modal intensities.

The MPIs are close to the modeled ones in the 'without water' case with a difference between ±1dB. Water contribution to the $S^2$ results can be numerically compensated by dividing the measured spectra by the properly scaled water transmission spectra. Unfortunately, during the acquisition time the hygrometry is subject to change and without an accurate measurement the compensation cannot be done. Recently, several complementary algorithms were proposed to allow mode reconstruction without the need of a preponderant mode [52] or to be able to separate the 2D-IP according to the involved modes [53]. These algorithms are yet to be implemented. Nevertheless, in the following experiments, the 'basic' $S^2$ algorithm was enough since we stayed in a preponderant mode excitation scheme.

### A.2. $S^2$ experiments

As mention before, $S^2$ can be realized in two ways. In the first way, spatial interferences are spectrally-resolved hence the required devices are: a tunable laser with the lowest spectral linewidth to enable the largest temporal frame window, a CCD camera. This way is faster but extra care has to be taken in the data post-processing since the camera sampling rate may cause distortion in the retrieved signal [51]. However, high resolution CCD cameras working around 2µm are not that easy to find and tunable lasers on the same bandwidth are quite expensive. In the second way, spectral interferences are spatially-resolved: a broadband white light source and an optical spectrum analyzer are required. In the following, I will present the spatially-resolved spectral interferences bench that I have created and fully automated through the use of LabView. Afterwards, modal content measurements on the passive few-mode fiber will be presented. It will be followed by the $S^2$ measurement of the active few-mode fiber completed by a GNLSE solving in the case of the


BY-NC-ND

$LP_{02}$ carrying a pulse in this fiber. Another measurement of a Tm-doped LMA will be presented to show the flexibility of the developed bench.

### A.2.1. S² setup

The bench is composed by three distinct parts depicted in Figure A-4:

- The all-fiber polarized output ASE source, Erbium and Thulium based ASE sources are currently available in the lab.
- The fiber under test (FUT), spliced to the ASE source, and its collimated output
- The automated scanning platform and optical spectrum analyzer.

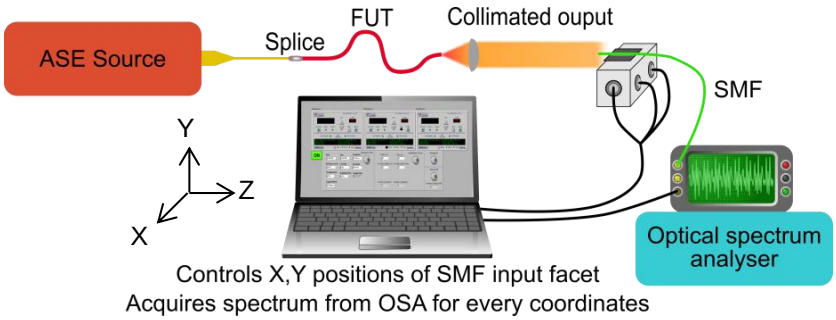


Figure A-IV-38: Spectrally- and spatially-resolved imaging bench scheme.

The ASE sources emit tens of mW of power with broadband spectrum to ensure good temporal resolution. The collimation is ensured by an achromatic set of lenses. The free space part is kept as short as possible to lower the water contribution to the measured spectra. The scanning platform has a 10 µm step resolution with a displacement width of 4 mm in 3D. The spatial resolution is set by the probe single mode fiber core diameter (in green in Figure A-4). By experience, the displacement step should not exceed 1.5 times the core diameter of the probe fiber to ensure resolution of the modal intensities close to zero. The spectral step is taken to be the shortest available on the OSA (0.05 nm ≈ 120 ps window) to achieve the widest temporal window. If the total DGD should be above 120 ps, aliasing will happen and can superimpose different DGD peaks. The spectral window is commonly taken around 30 nm (≈280 fs step), but if small DGDs (or close to zero) are to be measured, a wider window as to be taken. The limiting parameter on a pixel measurement in terms of time is the acquisition of the spectrum. As an example, a 51x51 pixels measurement with a 50 nm spectral window and 0.05 nm spectral resolution has 2 hours of acquisition time.


BY-NC-ND

### A.2.2. Passive FMF Modal content

The measurement was realized with successively 10 and 20 of fiber to allow retrieving every guided mode. The two pieces of FMF were badly spliced at the output of the in-house Tm-ASE source to ensure multimode excitation. The measurements were carried between 1860 and 1880 nm. Figure A-5 shows the reconstructed excited modes and their respective fDGD for both fiber lengths. In both measurements, the $LP_{11}$ fDGD is around 6.4 ps/m. The thinner peaks in Figure A-5-(b) are due the normalization by the fiber length creating a twice smaller temporal step. With 10 m of the passive FMF, the $LP_{02}$ could not be retrieved. There are two possible explanations. First, the excitation value is lower than the noise brought by water. Second, the $LP_{02}$ was not excited in this experiment. The $LP_{21}$ is retrieved at an fDGD around 11 ps/m. With 20 m of fiber, the $LP_{02}$ mode is reconstructed contrary to the $LP_{21}$. The dispersive $LP_{02}$ mode has a measured fDGD of roughly 5.2 ps/m. In Figure A-5-(b), two degenerate $LP_{11}$ modes were retrieved contrary to Figure A-5-(a). The difference in peak height is due to the polarized characteristic of the ASE source. This is consistent with the plateau formation of not temporally resolved degenerated modes reported by Nicholson and coworkers [50]. Those two modes could be observed thanks to the long piece of fiber used allowing enough accumulated group delay difference between the degenerated modes.

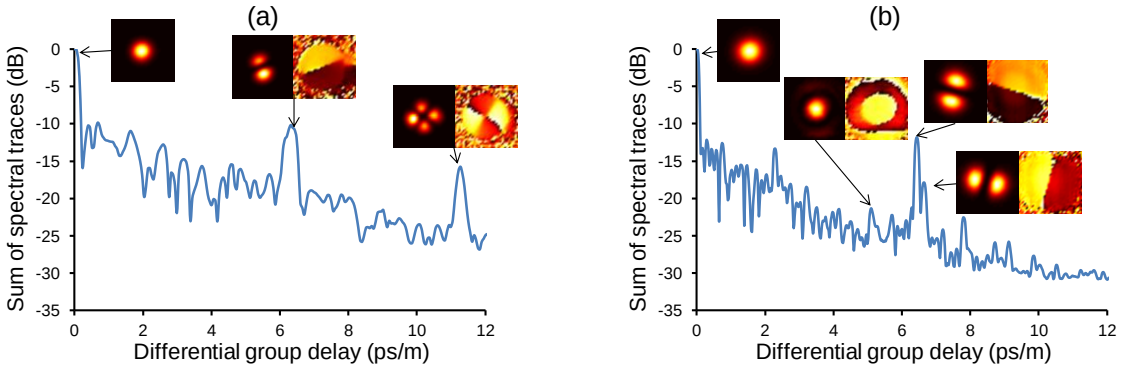


Figure A-IV-39: S² measurement of the passive few-mode fiber for (a) 10 m and (b) 20 m of length.

I was able to calculate the fDGDs of the guided modes in the passive few mode fiber by feeding the in-house mode solver with its measured refractive index profile. Table A-4 summarizes both measured and calculated fDGDs.

Table A-IV-15: Comparison of the measured by S² and calculated differential group delays in ps/m for the passive few mode fiber.

| | Measured fDGDs (ps/m) | Calculated fDGDs (ps/m) |
|---|---|---|
| $LP_{01\text{-}11}$ | 6.4 | 6.16 |
| $LP_{01\text{-}21}$ | 11 | 11.58 |
| $LP_{01\text{-}02}$ | 5.2 | 5.51 |


BY-NC-ND

The measured fDGDs agree well with the computed values. Even though the differential group delays are wavelength dependent, the S² measurement can still be applied and produces results with good agreement with fDGDs.

### A.2.3. Active FMF

To measure the modal content of the active few mode fiber, the test bench was modified to include a pumping stage to the thulium doped fiber under test as shown in Figure A-6-(a). 5 meters of the active FMF were used in this experiment; it required a 750 mW pumping to ensure a gain close to 1 dB at the output. As demonstrated in the linear modeling (IV.2), the modal weights along amplification vary. Therefore, the measured weights are only the output weights. It is not possible to know the exact excitation condition by just applying the loss coefficient. The output spectrum was centered at a longer wavelength due to short wavelengths absorption by thulium ions. However, the S² measurement was realized over a bandwidth that overlaps between input and output spectra (Figure A-6-(b)) to ensure measuring excited modes and not distributed excitation of modes.

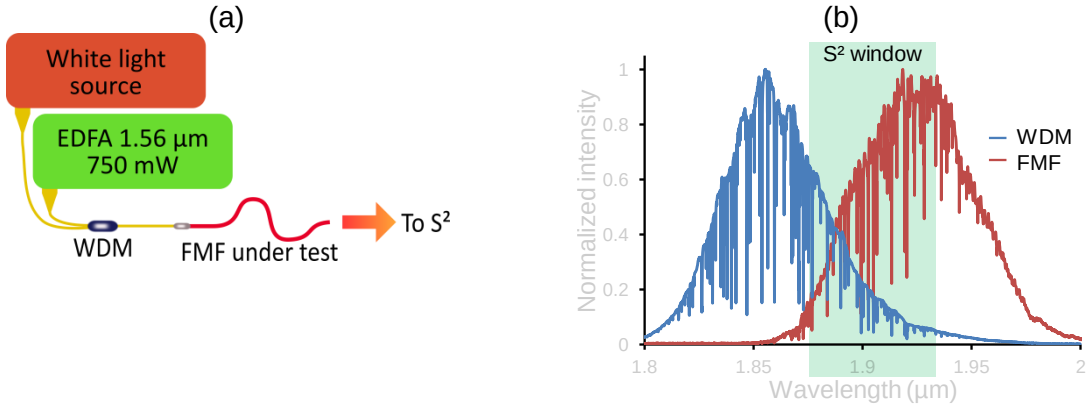


Figure A-IV-40: (a) S² setup for an active fiber. WDM: Wavelength division multiplexer. (b) Spectrum at the output of the WDM (blue) and of the active FMF (red). The S² measurement window is marked by the green surface.

In Figure A-6-(b), both spectrum present features due to water absorption in this wavelength range.

Only two degenerated $LP_{11}$ modes could be retrieved in these experiments. Higher order modes were not well enough excited and/or amplified to be recovered as it is shown in Figure III-8. The measured fDGD of the first $LP_{11}$ mode is 1.3 ps/m which is consistent with the calculated value of 1.23 ps/m. This shows that the $LP_{11}$ was excited at the splice between the WDM and the active FMF and not during a possible coupling along the fiber.


BY-NC-ND

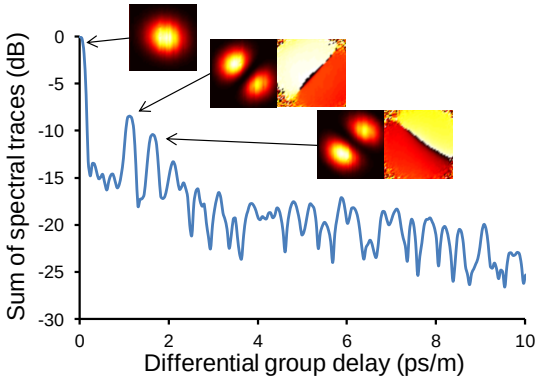


Figure A-IV-41: S² measurement on 5 m of the active few-mode fiber.

Since the measured fDGD of the $LP_{11}$ is in good agreement with calculated value, we can expect that this fiber also guides the $LP_{21}$ and the $LP_{02}$. The explanation behind not retrieving both $LP_{21}$ and $LP_{02}$ is twofold. First, the excitation of those modes is not guaranteed with the splice. A worse splice may produce an enhanced excitation of asymmetric modes but will unfortunately produce a modal content without a predominant mode. Second, due to the preponderant amplification of the fundamental mode, the $LP_{02}$ might not be retrieved at the output of the amplifier if not strongly excited. Indeed, the overlap integral between the $LP_{02}$ mode and the active media is far lower than that of the $LP_{01}$ due to its dispersive behavior.

### A.2.4. PM-LMA active fiber in a CPA scheme

The S² bench was brought to Novae facilities to perform a measurement on a commercial PM-LMA thulium-doped fiber presenting 40 µm core diameter with a numerical aperture of 0.2. The refractive index profile measurement of this fiber is still ongoing. It was however approximated by a step. This fiber is intrinsically multimode guiding at least the sixteen first LP modes around 2 µm. This fiber is used in a CPA scheme and the seed source was replaced by a pre-amplified white light source (Figure A-8). The output of the PM-LMA was angle cleaved for the CPA operation and kept that way of the S² measurements. The goal was to evaluate the singlemodedness at the output of the last stage of amplification. The calculated fDGDs for the first nine high order modes are presented in table A-5 using the rough estimation of a step index profile.

Table A-IV-16: Calculated fDGDs of the PM-LMA Thulium doped fiber 40 um core diameter and 0.2 numerical aperture when considering a step index profile.

| Interferences $LP_{01}$ with | $LP_{11}$ | $LP_{21}$ | $LP_{02}$ | $LP_{31}$ | $LP_{12}$ | $LP_{41}$ | $LP_{22}$ | $LP_{03}$ | $LP_{51}$ |
|---|---|---|---|---|---|---|---|---|---|
| fDGDs (ps/m) | 1.83 | 4.22 | 5.03 | 7.12 | 8.74 | 10.50 | 12.91 | 13.60 | 14.33 |


BY-NC-ND

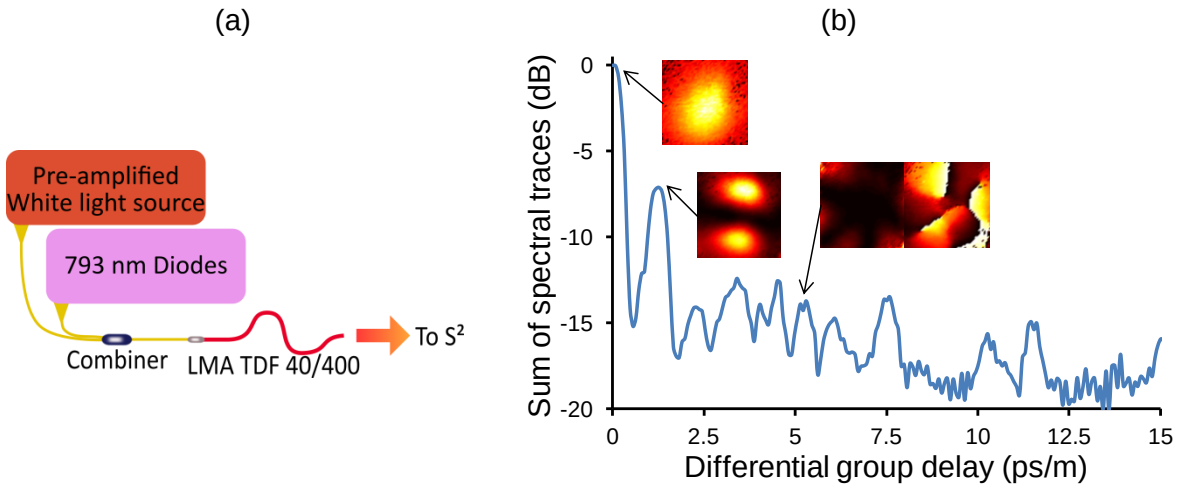


Figure A-IV-42: (a) S² setup for the PM-LMA fiber used in a CPA scheme by Novae. (b) S² measurement results with two identified higher order modes: $LP_{11}$ and $LP_{31}$.

Two major observations can be made when looking at the reconstructed modes in Figure A-8-(b). First, the angle cleave does not jeopardize the reconstruction. Second, the retrieved fDGDs are close to the calculated ones even though a basic step index profile was considered. The $LP_{11}$ presents a MPI value of -13 dB while the $LP_{31}$ one is of -25 dB. The $LP_{31}$ is not well defined in terms of intensity due to high reconstructed intensity in the corners of the figure. However the phase information allows clearing the doubt. Other peaks present intensity patterns with the same reconstruction issue as the $LP_{31}$, however their phases are not as well defined. Therefore, we can say that this linear excitation produces at least 6% of power in the higher order modes. Experiments are still ongoing to assess the impact of the presence of the higher order mode in the CPA regime.


BY-NC-ND

## References


[1] K. S. Kim, W. A. Reed, K. W. Quoi, and R. H. Stolen, 'Measurement of the nonlinear index of silica-core and dispersion-shifted fibers', *Opt. Lett.*, vol. 19, no. 4, pp. 257–259, Feb. 1994.

[2] A. B. Grudinin, E. M. Dianov, D. V. Korbkin, A. M. Prokhorov, and D. V. Khaidarov, 'Nonlinear mode coupling in multimode optical fibers; excitation of femtosecond-range stimulated-Raman-scattering solitons', *JETP Lett.*, vol. 47, no. 6, p. 356, Mar. 1988.

[3] Y. Tang, L. G. Wright, K. Charan, T. Wang, C. Xu, and F. W. Wise, 'Generation of intense 100 fs solitons tunable from 2 to 4.3 μm in fluoride fiber', *Optica*, vol. 3, no. 9, p. 948, Sep. 2016.

[4] I. H. Malitson, 'Interspecimen Comparison of the Refractive Index of Fused Silica*,†', *JOSA*, vol. 55, no. 10, pp. 1205–1209, Oct. 1965.

[5] H. Liu, 'Development Of Fiber Lasers That Generate Few-Cycle Optical Pulses', May 2014.

[6] N. G. Horton *et al.*, 'In vivo three-photon microscopy of subcortical structures within an intact mouse brain', *Nat. Photonics*, vol. 7, no. 3, pp. 205–209, Mar. 2013.

[7] A. B. Grudinin and S. Gray, 'Passive harmonic mode locking in soliton fiber lasers', *JOSA B*, vol. 14, no. 1, pp. 144–154, Jan. 1997.

[8] A. Chong, J. Buckley, W. Renninger, and F. Wise, 'All-normal-dispersion femtosecond fiber laser', *Opt. Express*, vol. 14, no. 21, p. 10095, 2006.

[9] H. Wang *et al.*, 'Dissipative Soliton Generation and Amplification in Erbium-Doped Fibers Operating at 1.55 μm', *IEEE J. Sel. Top. Quantum Electron.*, vol. 20, no. 5, pp. 283–289, Sep. 2014.

[10] Y. Tang, A. Chong, and F. W. Wise, 'Generation of 8 nJ pulses from a normal-dispersion thulium fiber laser', *Opt. Lett.*, vol. 40, no. 10, p. 2361, May 2015.

[11] W. H. Renninger, A. Chong, and F. W. Wise, 'Self-similar pulse evolution in an all-normal-dispersion laser', *Phys. Rev. A*, vol. 82, no. 2, p. 021805, Aug. 2010.

[12] M. E. Fermann, V. I. Kruglov, B. C. Thomsen, J. M. Dudley, and J. D. Harvey, 'Self-Similar Propagation and Amplification of Parabolic Pulses in Optical Fibers', *Phys. Rev. Lett.*, vol. 84, no. 26, pp. 6010–6013, Jun. 2000.

[13] Y. Zaouter *et al.*, 'Stretcher-free high energy nonlinear amplification of femtosecond pulses in rod-type fibers', *Opt. Lett.*, vol. 33, no. 2, p. 107, Jan. 2008.

[14] A. Ruehl, H. Hundertmark, D. Wandt, C. Fallnich, and D. Kracht, '0.7 W all-fiber Erbium oscillator generating 64 fs wave breaking-free pulses', *Opt. Express*, vol. 13, no. 16, pp. 6305–6309, Aug. 2005.

[15] J. Peng *et al.*, 'All-fiber ultrashort similariton generation, amplification, and compression at telecommunication band', *JOSA B*, vol. 29, no. 9, pp. 2270–2274, Sep. 2012.

[16] D. S. Chernykh *et al.*, 'Hybrid mode-locked erbium-doped all-fiber soliton laser with a distributed polarizer', *Appl. Opt.*, vol. 53, no. 29, pp. 6654–6662, Oct. 2014.

[17] K.-C. Chu, H.-Y. Jiang, and S.-D. Yang, 'High-energy femtosecond amplifier-similariton Er-doped fiber oscillator', *Opt. Lett.*, vol. 40, no. 22, pp. 5319–5322, Nov. 2015.

[18] D. Strickland and G. Mourou, 'Compression of amplified chirped optical pulses', *Opt. Commun.*, vol. 55, no. 6, pp. 447–449, Oct. 1985.




BY-NC-ND

[19] T. Eidam *et al.*, ‘Fiber chirped-pulse amplification system emitting 3.8 GW peak power’, *Opt. Express*, vol. 19, no. 1, pp. 255–260, Jan. 2011.

[20] F. Röser *et al.*, ‘Millijoule pulse energy high repetition rate femtosecond fiber chirped-pulse amplification system’, *Opt. Lett.*, vol. 32, no. 24, pp. 3495–3497, Dec. 2007.

[21] C. Gaida, M. Gebhardt, F. Stutzki, C. Jauregui, J. Limpert, and A. Tünnermann, ‘Thulium-doped fiber chirped-pulse amplification system with 2 GW of peak power’, *Opt. Lett.*, vol. 41, no. 17, pp. 4130–4133, Sep. 2016.

[22] F. Röser *et al.*, ‘90 W average power 100 µJ energy femtosecond fiber chirped-pulse amplification system’, *Opt. Lett.*, vol. 32, no. 15, pp. 2230–2232, Aug. 2007.

[23] D. Gaponov, L. Lavoute, S. Février, A. Hideur, and N. Ducros, ‘2µm all-fiber dissipative soliton master oscillator power amplifier’, 2016, p. 972834.

[24] F. Tan, H. Shi, R. Sun, P. Wang, and P. Wang, ‘1 µJ, sub-300 fs pulse generation from a compact thulium-doped chirped pulse amplifier seeded by Raman shifted erbium-doped fiber laser’, *Opt. Express*, vol. 24, no. 20, pp. 22461–22468, Oct. 2016.

[25] B. Oktem, C. Ülgüdür, and F. Ö. Ilday, ‘Soliton–similariton fibre laser’, *Nat. Photonics*, vol. 4, no. 5, pp. 307–311, May 2010.

[26] C. D. Poole, J. M. Wiesenfeld, A. R. McCormick, and K. T. Nelson, ‘Broadband dispersion compensation by using the higher-order spatial mode in a two-mode fiber’, *Opt. Lett.*, vol. 17, no. 14, p. 985, Jul. 1992.

[27] S. Ramachandran, J. m. Fini, M. Mermelstein, J. w. Nicholson, S. Ghalmi, and M. f. Yan, ‘Ultra-large effective-area, higher-order mode fibers: a new strategy for high-power lasers’, *Laser Photonics Rev.*, vol. 2, no. 6, pp. 429–448, Dec. 2008.

[28] X. Peng *et al.*, ‘Higher-order mode fiber enables high energy chirped-pulse amplification’, *Opt. Express*, vol. 21, no. 26, pp. 32411–32416, Dec. 2013.

[29] S. Ramachandran, ‘Dispersion-Tailored Few-Mode Fibers: A Versatile Platform for In-Fiber Photonic Devices’, *J. Light. Technol.*, vol. 23, no. 11, p. 3426, Nov. 2005.

[30] A. E. Miller, R. L. Opila, and M. F. Yan, ‘Ultranegative delta cladding for modified chemical vapor deposition’, 1996, pp. 56–58.

[31] G. Humbert and A. Malki, ‘Electric-arc-induced gratings in non-hydrogenated fibres: fabrication and high-temperature characterizations’, *J. Opt. Pure Appl. Opt.*, vol. 4, no. 2, p. 194, 2002.

[32] K. Lai, S. G. Leon-Saval, A. Witkowska, W. J. Wadsworth, and T. A. Birks, ‘Wavelength-independent all-fiber mode converters’, *Opt. Lett.*, vol. 32, no. 4, pp. 328–330, Feb. 2007.

[33] J. W. Nicholson, A. D. Yablon, S. Ramachandran, and S. Ghalmi, ‘Spatially and spectrally resolved imaging of modal content in large-mode-area fibers’, *Opt. Express*, vol. 16, no. 10, pp. 7233–7243, May 2008.

[34] F. Morin, *Conception d’une source à impulsions courtes à 1600 nm à fibres dopées erbium□: application à la greffe de cornée*. Paris 11, 2010.

[35] S. G. Leon-Saval, N. K. Fontaine, J. R. Salazar-Gil, B. Ercan, R. Ryf, and J. Bland-Hawthorn, ‘Mode-selective photonic lanterns for space-division multiplexing’, *Opt. Express*, vol. 22, no. 1, pp. 1036–1044, Jan. 2014.

[36] T. A. Birks, I. Gris-Sánchez, S. Yerolatsitis, S. G. Leon-Saval, and R. R. Thomson, ‘The photonic lantern’, *Adv. Opt. Photonics*, vol. 7, no. 2, p. 107, Jun. 2015.

[37] A. M. Velazquez-Benitez *et al.*, ‘Six mode selective fiber optic spatial multiplexer’, *Opt. Lett.*, vol. 40, no. 8, pp. 1663–1666, Apr. 2015.



BY-NC-ND

[38] G. Lopez-Galmiche *et al.*, ‘Few-mode erbium-doped fiber amplifier with photonic lantern for pump spatial mode control’, *Opt. Lett.*, vol. 41, no. 11, pp. 2588–2591, Jun. 2016.

[39] M. A. Khamis and K. Ennser, ‘Theoretical Model of a Thulium-Doped Fiber Amplifier Pumped at 1570 nm and 793 nm in the Presence of Cross Relaxation’, *J. Light. Technol.*, vol. 34, no. 24, pp. 5675–5681, Dec. 2016.

[40] P. Peterka, I. Kasik, A. Dhar, B. Dussardier, and W. Blanc, ‘Theoretical modeling of fiber laser at 810 nm based on thulium-doped silica fibers with enhanced ^3H_4 level lifetime’, *Opt. Express*, vol. 19, no. 3, p. 2773, Jan. 2011.

[41] S. D. Agger and J. H. Povlsen, ‘Emission and absorption cross section of thulium doped silica fibers’, *Opt. Express*, vol. 14, no. 1, p. 50, 2006.

[42] S. D. Jackson and T. A. King, ‘Theoretical modeling of Tm-doped silica fiber lasers’, *J. Light. Technol.*, vol. 17, no. 5, pp. 948–956, May 1999.

[43] M. DEVAUTOUR, ‘Étude de fibres actives combinant large cœur et fort niveau de dopage pour l’émission unimodale□’:, thesis, Université de Limoges.

[44] S. Wielandy, ‘Implications of higher-order mode content in large mode area fibers with good beam quality’, *Opt. Express*, vol. 15, no. 23, pp. 15402–15409, Nov. 2007.

[45] D. B. S. Soh, J. Nilsson, S. Baek, C. Codemard, Y. Jeong, and V. Philippov, ‘Modal power decomposition of beam intensity profiles into linearly polarized modes of multimode optical fibers’, *JOSA A*, vol. 21, no. 7, pp. 1241–1250, Jul. 2004.

[46] M. Paurisse, L. Lévèque, M. Hanna, F. Druon, and P. Georges, ‘Complete measurement of fiber modal content by wavefront analysis’, *Opt. Express*, vol. 20, no. 4, pp. 4074–4084, Feb. 2012.

[47] Y. Ma, ‘Characterization of Higher Order Modes in Optical Fibers, Charakterisierung von Moden höherer Ordnung in optischen Fasern’.

[48] Y. Z. Ma *et al.*, ‘Fiber-modes and fiber-anisotropy characterization using low-coherence interferometry’, *Appl. Phys. B*, vol. 96, no. 2–3, pp. 345–353, Aug. 2009.

[49] D. N. Schimpf, R. A. Barankov, and S. Ramachandran, ‘Cross-correlated ($C^2$) imaging of fiber and waveguide modes’, *Opt. Express*, vol. 19, no. 14, pp. 13008–13019, Jul. 2011.

[50] J. W. Nicholson, A. D. Yablon, J. M. Fini, and M. D. Mermelstein, ‘Measuring the Modal Content of Large-Mode-Area Fibers’, *IEEE J. Sel. Top. Quantum Electron.*, vol. 15, no. 1, pp. 61–70, Jan. 2009.

[51] D. R. Gray *et al.*, ‘Accurate calibration of S^2 and interferometry based multimode fiber characterization techniques’, *Opt. Express*, vol. 23, no. 8, p. 10540, Apr. 2015.

[52] H. Otto, F. Jansen, F. Stutzki, C. Jauregui, J. Limpert, and A. Tunnermann, ‘Improved Modal Reconstruction for Spatially and Spectrally Resolved Imaging’, *J. Light. Technol.*, vol. 31, no. 8, pp. 1295–1299, Apr. 2013.

[53] B. Sévigny *et al.*, ‘Advanced S Imaging: Application of Multivariate Statistical Analysis to Spatially and Spectrally Resolved Datasets’, *J. Light. Technol.*, vol. 32, no. 23, pp. 4606–4612, Dec. 2014.



BY-NC-ND

## Table of figures





BY-NC-ND

BY-NC-ND

BY-NC-ND

BY-NC-ND

BY-NC-ND

BY-NC-ND

BY-NC-ND

## Table of tables





BY-NC-ND

BY-NC-ND

## Table of contents




BY-NC-ND

BY-NC-ND

BY-NC-ND

**Développement de fibres optiques à dispersion contrôlée pour l'élaboration de lasers ultrarapides à 2 µm**

L'objectif de cette thèse est d'ouvrir la voie à la démonstration de l'amplification parabolique à 2 µm en format tout fibré. La théorie sur l'amplification d'impulsions auto-similaires est d'abord présentée. Il en découle que le meilleur amplificateur tout fibré à 2 µm devra s'appuyer sur une fibre dopée aux ions Tm3+ présentant à la fois une forte dispersion normale et une grand aire effective. L'amplification parabolique ne peut pas être réalisée dans des fibres monomodes à base de silice à 2 µm du fait de la forte dispersion anormale présentée par le matériau. Afin de surmonter cette limitation, une fibre dont le mode $LP_{02}$ présente à la fois une forte dispersion normale et une grande aire effective à 2 µm a été conçue et réalisée. Un convertisseur spatial de lumière dédié à la génération du mode $LP_{02}$ a également été conçu et réalisé. La pureté d'excitation par ce convertisseur du mode $LP_{02}$ de la fibre passive a été évaluée à 99,9% par la technique interférométrique d'imagerie spatialement et spectralement résolue. Une source d'impulsions ultrabrèves (100 fs) et accordable en longueur d'onde de 1,6 µm à 2 µm a été créée pour générer le signal de l'amplificateur. Cette source a en outre permis de mesurer la dispersion du mode $LP_{02}$ de la fibre passive à la longueur d'onde de 1,95 µm, celle-ci vaut -106 ps/(nm.km) en excellent accord quantitatif avec les résultats numériques. Des modélisations numériques de l'amplificateur nonlinéaire basé sur la version active de cette fibre indiquent que des impulsions présentant une puissance crête de l'ordre du MW à 1,9 µm sont envisageables en sortie de l'amplificateur parabolique.

Mots-clés : Fibres optiques à dispersion contrôlée, mode d'ordre élevé, excitation sélective, amplification parabolique

**Development of dispersion tailored optical fibers for ultrafast 2 µm lasers**

The goal of this PhD thesis is to pave the way towards the demonstration of parabolic amplification at 2 µm in an all-fiber format. The physical theory on self-similar pulse amplification is first presented. The best all-fiber amplifier at 2 µm would need a special Tm-doped fiber with both high normal dispersion and large effective area. Parabolic amplification is however prohibited in silica based singlemode fiber working at 2 µm due to the large anomalous dispersion of silica. To overcome this limitation, a four-mode fiber in which the $LP_{02}$ mode exhibits high normal dispersion combined with large effective area at 2 µm was designed and manufactured. A dedicated mode converter has also been designed and manufactured. Using the spatially- and spectrally-resolved imaging technique the purity of excitation of the $LP_{02}$ mode in the passive fiber was evaluated to 99.9%. An ultrashort pulse (100 fs) source tunable from 1.6 µm to 2 µm was implemented to seed the amplifier. This source allowed to measure the $LP_{02}$ mode dispersion of the passive fiber at the wavelength of 1.95 µm: D = -106 ps/(nm.km) in excellent quantitative agreement with the simulations. Numerical modeling of a nonlinear amplifier based on the realized active fiber shows that MW peak power class pulses centered at 1.9 µm can be obtained at the output of the parabolic amplifier.

Keywords: Dispersion tailored fibers, high order modes, selective excitation, parabolic amplification